

# Search for Spatially Extended *Fermi*-LAT Sources Using Two Years of Data

J. Lande<sup>1,2</sup>, M. Ackermann<sup>3,4</sup>, A. Allafort<sup>1</sup>, J. Ballet<sup>5</sup>, K. Bechtol<sup>1</sup>, T. H. Burnett<sup>6</sup>, J. Cohen-Tanugi<sup>7</sup>, A. Drlica-Wagner<sup>1</sup>, S. Funk<sup>1,8</sup>, F. Giordano<sup>9,10</sup>, M.-H. Grondin<sup>11,12</sup>, M. Kerr<sup>1</sup>, M. Lemoine-Goumard<sup>13,14</sup>

## ABSTRACT

Spatial extension is an important characteristic for correctly associating  $\gamma$ -ray-emitting sources with their counterparts at other wavelengths and for obtaining an unbiased model of their spectra. We present a new method for quantifying the spatial extension of sources detected by the Large Area Telescope (LAT), the primary science instrument on the *Fermi Gamma-ray Space Telescope (Fermi)*. We perform a series of Monte Carlo simulations to validate this tool and calculate

---

<sup>1</sup>W. W. Hansen Experimental Physics Laboratory, Kavli Institute for Particle Astrophysics and Cosmology, Department of Physics and SLAC National Accelerator Laboratory, Stanford University, Stanford, CA 94305, USA

<sup>2</sup>email: joshualande@gmail.com

<sup>3</sup>Deutsches Elektronen Synchrotron DESY, D-15738 Zeuthen, Germany

<sup>4</sup>email: markus.ackermann@desy.de

<sup>5</sup>Laboratoire AIM, CEA-IRFU/CNRS/Université Paris Diderot, Service d'Astrophysique, CEA Saclay, 91191 Gif sur Yvette, France

<sup>6</sup>Department of Physics, University of Washington, Seattle, WA 98195-1560, USA

<sup>7</sup>Laboratoire Univers et Particules de Montpellier, Université Montpellier 2, CNRS/IN2P3, Montpellier, France

<sup>8</sup>email: funk@slac.stanford.edu

<sup>9</sup>Dipartimento di Fisica "M. Merlin" dell'Università e del Politecnico di Bari, I-70126 Bari, Italy

<sup>10</sup>Istituto Nazionale di Fisica Nucleare, Sezione di Bari, 70126 Bari, Italy

<sup>11</sup>Max-Planck-Institut für Kernphysik, D-69029 Heidelberg, Germany

<sup>12</sup>Landessternwarte, Universität Heidelberg, Königstuhl, D 69117 Heidelberg, Germany

<sup>13</sup>Université Bordeaux 1, CNRS/IN2p3, Centre d'Études Nucléaires de Bordeaux Gradignan, 33175 Gradignan, France

<sup>14</sup>Funded by contract ERC-StG-259391 from the European Community

the LAT threshold for detecting the spatial extension of sources. We then test all sources in the second *Fermi*-LAT catalog (2FGL) for extension. We report the detection of seven new spatially extended sources.

8 *Subject headings:* Catalogs; Fermi Gamma-ray Space Telescope; Gamma rays:  
9 observations; ISM: supernova remnants; Methods: statistical; pulsar wind nebula

## 10 1. Introduction

11 A number of astrophysical source classes including supernova remnants (SNRs), pulsar  
12 wind nebulae (PWNe), molecular clouds, normal galaxies, and galaxy clusters are expected  
13 to be spatially resolvable by the Large Area Telescope (LAT), the primary instrument on  
14 the *Fermi Gamma-ray Space Telescope* (*Fermi*). Additionally, dark matter satellites are also  
15 hypothesized to be spatially extended. See Atwood et al. (2009a) for pre-launch predictions.  
16 The LAT has detected seven SNRs which are significantly extended at GeV energies: W51C,  
17 W30, IC 443, W28, W44, RX J1713.7–3946, and the Cygnus Loop (Abdo et al. 2009a, 2012b,  
18 2010h,e,g, 2011; Katagiri et al. 2011). In addition, three extended PWN have been detected  
19 by the LAT: MSH 15–52, Vela X, and HESS J1825–137 (Abdo et al. 2010a,f; Grondin et al.  
20 2011). Two nearby galaxies, the Large and Small Magellanic Clouds, and the lobes of one  
21 radio galaxy, Centaurus A, were spatially resolved at GeV energies (Abdo et al. 2010i,b,c).  
22 A number of additional sources detected at GeV energies are positionally coincident with  
23 sources that exhibit large enough extension at other wavelengths to be spatially resolvable  
24 by the LAT at GeV energies. In particular, there are 59 GeV sources in the second Fermi  
25 Source Catalog (2FGL) that might be associated with extended SNRs (2FGL, Nolan et al.  
26 2012). Previous analyses of extended LAT sources were performed as dedicated studies of  
27 individual sources so we expect that a systematic scan of all LAT-detected sources could  
28 uncover additional spatially extended sources.

29 The current generation of air Cherenkov detectors have made it apparent that many  
30 sources can be spatially resolved at even higher energies. Most prominent was a survey of  
31 the Galactic plane using the High Energy Stereoscopic System (H.E.S.S) which reported 14  
32 spatially extended sources with extensions varying from  $\sim 0^\circ.1$  to  $\sim 0^\circ.25$  (Aharonian et al.  
33 2006). Within our Galaxy very few sources detected at TeV energies, most notably the  $\gamma$ -ray  
34 binaries LS 5039 (Aharonian et al. 2006a), LS I+61–303 (Albert et al. 2006; Acciari et al.  
35 2011), HESS J0632+057 (Aharonian et al. 2007c), and the Crab nebula (Weekes et al. 1989),  
36 have no detectable extension. High-energy  $\gamma$ -rays from TeV sources are produced by the de-  
37 cay of  $\pi^0$ s produced by hadronic interactions with interstellar matter and by relativistic  
38 electrons due to Inverse Compton (IC) scattering and bremsstrahlung radiation. It is plausi-

39 ble that the GeV and TeV emission from these sources originates from the same population  
40 of high-energy particles and so at least some of these sources should be detectable at GeV  
41 energies. Studying these TeV sources at GeV energies would help to determine the emission  
42 mechanisms producing these high energy photons.

43 The LAT is a pair conversion telescope that has been surveying the  $\gamma$ -ray sky since 2008  
44 August. The LAT has broad energy coverage (20 MeV to  $> 300$  GeV), wide field of view  
45 ( $\sim 2.4$  sr), and large effective area ( $\sim 8000$  cm<sup>2</sup> at  $> 1$  GeV) Additional information about  
46 the performance of the LAT can be found in Atwood et al. (2009b).

47 Using 2 years of all-sky survey data, the LAT Collaboration published 2FGL (2FGL,  
48 Nolan et al. 2012). The possible counterparts of many of these sources can be spatially  
49 resolved when observed at other frequencies. But detecting the spatial extension of these  
50 sources at GeV energies is difficult because the size of the point-spread function (PSF) of  
51 the LAT is comparable to the typical size of many of these sources.

52 The capability to spatially resolve GeV  $\gamma$ -ray sources is important for several reasons.  
53 Finding a coherent source extension across different energy bands can help to associate a LAT  
54 source to an otherwise confused counterpart. Furthermore,  $\gamma$ -ray emission from dark matter  
55 annihilation has been predicted to be detectable by the LAT. Some of the dark matter  
56 substructure in our Galaxy could be spatially resolvable by the LAT (Baltz et al. 2008).  
57 Characterization of spatial extension could help to identify this substructure. Also, due to  
58 the strong energy dependence of the LAT PSF, the spatial and spectral characterization of a  
59 source cannot be decoupled. An inaccurate spatial model will bias the spectral model of the  
60 source and vice versa. Specifically, modeling a spatially extended source as point-like will  
61 systematically soften measured spectra. Furthermore, correctly modeling source extension  
62 is important for understanding an entire region of the sky. For example, an imperfect  
63 model of the spatially extended LMC introduced significant residuals in the surrounding  
64 region (Abdo et al. 2010d; Nolan et al. 2012). Such residuals can bias the significance and  
65 measured spectra of neighboring sources in the densely populated Galactic plane.

66 For these reasons, in Section 2 we present a new systematic method for analyzing spa-  
67 tially extended LAT sources. In Section 3, we demonstrate that this method can be used to  
68 test the statistical significance of the extension of a LAT source and we assess the expected  
69 level of bias introduced by assuming an incorrect spatial model. In Section 4, we calculate  
70 the LAT detection threshold to resolve the extension of a source. In Section 5, we study the  
71 ability of the LAT to distinguish between a single extended source and unresolved closely-  
72 spaced point-like sources In Section 6, we further demonstrate that our detection method  
73 does not misidentify point-like sources as being extended by testing the extension of active  
74 Galactic nuclei (AGN) believed to be unresolvable. In Section 7, we systematically reanalyze

75 the twelve extended sources included in the 2FGL catalog and in Section 8 we describe a  
76 way to estimate systematic errors on the measured extension of a source. In Section 9, we  
77 describe a search for new spatially extended LAT sources. Finally, in Section 10 we present  
78 the detection of the extension of nine spatially extended sources that were reported in the  
79 2FGL catalog but treated as point-like in the analysis. Two of these sources have been  
80 previously analyzed in dedicated publications.

## 81 **2. Analysis Methods**

82 Morphological studies of sources using the LAT are challenging because of the strongly  
83 energy-dependent PSF that is comparable in size to the extension of many sources expected  
84 to be detected at GeV energies. Additional complications arise for sources along the Galactic  
85 plane due to systematic uncertainties in the model for Galactic diffuse emission.

86 For energies below  $\sim 300$  MeV, the angular resolution is limited by multiple scattering in  
87 the silicon strip tracking section of the detector and is several degrees at 100 MeV. The PSF  
88 improves with energy approaching a 68% containment radius of  $\sim 0.2^\circ$  at the highest energies  
89 (when averaged over the acceptance of the LAT) and is limited by the ratio of the strip pitch  
90 to the height of the tracker (Atwood et al. 2009b; Abdo et al. 2009d, 2012a).<sup>1</sup> However, since  
91 most high energy astrophysical sources have spectra that decrease rapidly with increasing  
92 energy, there are typically fewer higher energy photons with improved angular resolution.  
93 Therefore sophisticated analysis techniques are required to maximize the sensitivity of the  
94 LAT to extended sources.

### 95 **2.1. Modeling Extended Sources in the `pointlike` Package**

96 A new maximum-likelihood analysis tool has been developed to address the unique  
97 requirements for studying spatially extended sources with the LAT. It works by maximizing  
98 the Poisson likelihood to detect the observed distributions of  $\gamma$ -rays (referred to as counts)  
99 given a parametrized spatial and spectral model of the sky. The data are binned spatially,  
100 using a HEALPix pixellization, and spectrally (Górski et al. 2005) and the likelihood is  
101 maximized over all bins in a region. The extension of a source can be modeled by a geometric  
102 shape (e.g. a disk or a two-dimensional Gaussian) and the position, extension, and spectrum

---

<sup>1</sup>More information about the performance of the LAT can be found at the *Fermi* Science Support Center (FSSC, <http://fermi.gsfc.nasa.gov>).

103 of the source can be simultaneously fit.

104 This type of analysis is unwieldy using the standard LAT likelihood analysis tool `gtlike`<sup>2</sup>  
 105 because it can only fit the spectral parameters of the model unless a more sophisticated  
 106 iterative procedure is used. We note that `gtlike` has been used in the past in several studies  
 107 of source extension in the LAT Collaboration (Abdo et al. 2010i,b,e, 2009a). In these studies,  
 108 a set of `gtlike` maximum likelihood fits at fixed extensions was used to build a profile of the  
 109 likelihood as a function of extension. The `gtlike` likelihood profile approach has been shown  
 110 to correctly reproduce the extension of simulated extended sources assuming that the true  
 111 position is known (Giordano 2011). But it is not optimal because the position, extension,  
 112 and spectrum of the source must be simultaneously fit to find the best fit parameters and  
 113 to maximize the statistical significance of the detection. Furthermore, because the `gtlike`  
 114 approach is computationally intensive, no large-scale Monte Carlo simulations have been run  
 115 to calculate its false detection rate.

116 The approach presented here is based on a second maximum likelihood fitting package  
 117 developed in the LAT Collaboration called `pointlike` (Abdo et al. 2010d; Kerr 2011). The  
 118 choice to base the spatial extension fitting on `pointlike` rather than `gtlike` was made due  
 119 to considerations of computing time. The `pointlike` algorithm was optimized for speed  
 120 to handle larger numbers of sources efficiently, which is important for our catalog scan  
 121 and for being able to perform large-scale Monte Carlo simulations to validate the analysis.  
 122 Details on the `pointlike` package can be found in Kerr (2011). We extended the code to  
 123 allow a simultaneous fit of the source extension together with the position and the spectral  
 124 parameters.

## 125 2.2. Extension Fitting

126 In `pointlike`, one can fit the position and extension of a source under the assumption  
 127 that the source model can be factorized:  $M(x, y, E) = S(x, y) \times X(E)$ , where  $S(x, y)$  is  
 128 the spatial distribution and  $X(E)$  is the spectral distribution. To fit an extended source,  
 129 `pointlike` convolves the extended source shape with the PSF (as a function of energy)  
 130 and uses the `minuit` library (James & Roos 1975) to maximize the likelihood by simulta-  
 131 neously varying the position, extension, and spectrum of the source. As will be described  
 132 in Section 3.1, simultaneously fitting the position, extension, and spectrum is important to  
 133 maximize the statistical significance of the detection of the extension of a source. To avoid  
 134 projection effects, the longitude and latitude of the source are not directly fit but instead

---

<sup>2</sup>`gtlike` is distributed publicly by the FSSC.

135 the displacement of the source in a reference frame centered on the source.

The significance of the extension of a source can be calculated from the likelihood-ratio test. The likelihood ratio defines the test statistic (TS) by comparing the likelihood of a simpler hypothesis to a more complicated one:

$$\text{TS} = 2 \log(\mathcal{L}(H_1)/\mathcal{L}(H_0)), \quad (1)$$

where  $H_1$  is the more complicated hypothesis and  $H_0$  the simpler one. For the case of the extension test, we compare the likelihood when assuming the source has either a point-like or spatially extended spatial model:

$$\text{TS}_{\text{ext}} = 2 \log(\mathcal{L}_{\text{ext}}/\mathcal{L}_{\text{ps}}). \quad (2)$$

136 `pointlike` calculates  $\text{TS}_{\text{ext}}$  by fitting a source first with a spatially extended model and  
 137 then as a point-like source. The interpretation of  $\text{TS}_{\text{ext}}$  in terms of a statistical significance  
 138 is discussed in Section 3.1.

For extended sources with an assumed radially-symmetric shape, we optimized the calculation by performing one of the integrals analytically. The expected photon distribution can be written as

$$\text{PDF}(\vec{r}) = \int \text{PSF}(|\vec{r} - \vec{r}'|) I_{\text{src}}(\vec{r}') r' dr' d\phi' \quad (3)$$

where  $\vec{r}$  represents the position in the sky and  $I_{\text{src}}(\vec{r})$  is the spatial distribution of the source. The PSF of the LAT is currently parameterized in the Pass 7\_V6 (P7\_V6) Source Instrument Response Function (IRFs, Abdo et al. 2012a) by a King function (King 1962):

$$\text{PSF}(r) = \frac{1}{2\pi\sigma^2} \left(1 - \frac{1}{\gamma}\right) \left(1 + \frac{u}{\gamma}\right)^{-\gamma}, \quad (4)$$

where  $u = (r/\sigma)^2/2$  and  $\sigma$  and  $\gamma$  are free parameters (Kerr 2011). For radially-symmetric extended sources, the angular part of the integral can be evaluated analytically

$$\text{PDF}(u) = \int_0^\infty r' dr' I_{\text{src}}(v) \int_0^{2\pi} d\phi' \text{PSF}(\sqrt{2\sigma^2(u + v - 2\sqrt{uv} \cos(\phi - \phi'))}) \quad (5)$$

$$= \int_0^\infty dv I_{\text{src}}(v) \left(\frac{\gamma - 1}{\gamma}\right) \left(\frac{\gamma}{\gamma + u + v}\right)^\gamma \times {}_2F_1\left(\gamma/2, \frac{1 + \gamma}{2}, 1, \frac{4uv}{(\gamma + u + v)^2}\right), \quad (6)$$

139 where  $v = (r'/\sigma)^2/2$  and  ${}_2F_1$  is the Gaussian hypergeometric function. This convolution  
 140 formula reduces the expected photon distribution to a single numerical integral.

141 There will always be a small numerical discrepancy between the expected photon dis-  
 142 tribution derived from a true point-like source and a very small extended source due to

143 numerical error in the convolution. In most situations, this error is insignificant. But in  
 144 particular for very bright sources, this numerical error has the potential to bias the TS for  
 145 the extension test. Therefore, when calculating  $TS_{\text{ext}}$ , we compare the likelihood fitting the  
 146 source with an extended spatial model to the likelihood when the extension is fixed to a very  
 147 small value ( $10^{-10}$  degrees in radius for a uniform disk model).

148 We estimate the error on the extension of a source by fixing the position of the source  
 149 and varying the extension until the log of the likelihood has decreased by  $1/2$ , corresponding  
 150 to a  $1\sigma$  error (Eadie et al. 1971). Figure 1 demonstrates this method by showing the change  
 151 in the log of the likelihood when varying the modeled extension of the SNR IC 443. The  
 152 localization error is calculated by fixing the extension and spectrum of the source to their  
 153 best fit values and then fitting the log of the likelihood to a 2D Gaussian as a function of  
 154 position. This localization error algorithm is further described in Nolan et al. (2012).

### 155 2.3. `gtlike` Analysis Validation

156 `pointlike` is important for analyses of LAT data that require many iterations such as  
 157 source localization and extension fitting. On the other hand, because `gtlike` makes fewer  
 158 approximations in calculating the likelihood we expect the spectral parameters found with  
 159 `gtlike` to be slightly more accurate. Furthermore, because `gtlike` is the standard likelihood  
 160 analysis package for LAT data, it has been more extensively validated for spectral analysis.  
 161 For those reasons, in the following analysis we used `pointlike` to determine the position and  
 162 extension of a source and subsequently derived the spectrum using `gtlike`. Both `gtlike` and  
 163 `pointlike` can be used to estimate the statistical significance of the extension of a source  
 164 and we required that both methods agree for a source to be considered extended. There was  
 165 good agreement between the two methods. Unless explicitly mentioned, all TS,  $TS_{\text{ext}}$ , and  
 166 spectral parameters were calculated using `gtlike` with the best-fit positions and extension  
 167 found by `pointlike`.

### 168 2.4. Comparing Source Sizes

We considered two models for the surface brightness profile for extended sources: a 2D Gaussian model

$$I_{\text{Gaussian}}(x, y) = \frac{1}{2\pi\sigma^2} \exp\left(-\frac{x^2 + y^2}{2\sigma^2}\right) \quad (7)$$

or a uniform disk model

$$I_{\text{disk}}(x, y) = \begin{cases} \frac{1}{\pi\sigma^2} & x^2 + y^2 \leq \sigma^2 \\ 0 & x^2 + y^2 > \sigma^2. \end{cases} \quad (8)$$

Although these shapes are significantly different, Figure 2 shows that, after convolution with the LAT PSF, their PDFs are similar for a source that has a  $0.5^\circ$  radius typical of LAT-detected extended sources. To allow a valid comparison between the Gaussian and the uniform disk models, we define the source size as the radius containing 68% of the intensity ( $r_{68}$ ). By direct integration, we find

$$r_{68, \text{Gaussian}} = 1.51\sigma, \quad (9)$$

$$r_{68, \text{disk}} = 0.82\sigma, \quad (10)$$

169 where  $\sigma$  is defined in Equation 7 and Equation 8 respectively. For the example above,  
 170  $r_{68} = 0.5^\circ$  so  $\sigma_{\text{disk}} = 0.61^\circ$  and  $\sigma_{\text{Gaussian}} = 0.33^\circ$ .

171 For sources that are comparable in size to the PSF, the differences in the PDF for  
 172 different spatial models are lost in the noise and the LAT is not sensitive to the detailed  
 173 spatial structure of these sources. In section 3.3, we perform a dedicated Monte Carlo  
 174 simulation that shows there is little bias due to incorrectly modeling the spatial structure  
 175 of an extended source. Therefore, in our search for extended sources we use only a radially-  
 176 symmetric uniform disk spatial model. Unless otherwise noted, we quote the radius to the  
 177 edge ( $\sigma$ ) as the size of the source.

### 178 3. Validation of the TS Distribution

#### 179 3.1. Point-like Source Simulations Over a Uniform Background

We tested the theoretical distribution for  $\text{TS}_{\text{ext}}$  to evaluate the false detection probability for measuring source extension. To do so, we tested simulated point-like sources for extension. Mattox et al. (1996) discuss that the TS distribution for a likelihood-ratio test on the existence of a source at a given position is

$$P(\text{TS}) = \frac{1}{2}(\chi_1^2(\text{TS}) + \delta(\text{TS})), \quad (11)$$

180 where  $P(\text{TS})$  is the probability density to get a particular value of TS,  $\chi_1^2$  is the chi-squared  
 181 distribution with one degree of freedom, and  $\delta$  is the Dirac delta function. The particular  
 182 form of Equation 11 is due to the null hypothesis (source flux  $\Phi = 0$ ) residing on the edge  
 183 of parameter space and the model hypothesis adding a single degree of freedom (the source  
 184 flux). It leads to the often quoted result  $\sqrt{TS} = \sigma$ , where  $\sigma$  here refers to the significance of



185 the detection. It is plausible to expect a similar distribution for the TS in the test for source  
 186 extension since the same conditions apply (with the source flux  $\Phi$  replaced by the source  
 187 radius  $r$  and  $r < 0$  being unphysical). To verify Equation 11, we evaluated the empirical  
 188 distribution function of  $\text{TS}_{\text{ext}}$  computed from simulated sources.

189 We simulated point-like sources with various spectral forms using the LAT on-orbit  
 190 simulation tool `gtobssim`<sup>3</sup> and fit the sources with `pointlike` using both point-like and ex-  
 191 tended source hypotheses. These point-like sources were simulated with a power-law spectral  
 192 model with integrated fluxes above 100 MeV ranging from  $3 \times 10^{-9}$  to  $1 \times 10^{-5}$   $\text{ph cm}^{-2} \text{s}^{-1}$   
 193 and spectral indices ranging from 1.5 to 3. These values were picked to represent typical  
 194 parameters of LAT-detected sources. The point-like sources were simulated on top of an  
 195 isotropic background with a power-law spectral model with integrated flux above 100 MeV  
 196 of  $1.5 \times 10^{-5}$   $\text{ph cm}^{-2} \text{s}^{-1} \text{sr}^{-1}$  and spectral index 2.1. This was taken to be the same as the  
 197 isotropic spectrum measured by EGRET (Sreekumar et al. 1998). This spectrum is compa-  
 198 rable to the high-latitude background intensity seen by the LAT. The Monte Carlo simulation  
 199 was performed over a one-year observation period using a representative spacecraft orbit and  
 200 livetime. The reconstruction was performed using the P7\_V6 Source class event selection and  
 201 IRFs (Abdo et al. 2012a). For each significantly detected point-like source ( $\text{TS} \geq 25$ ), we  
 202 used `pointlike` to fit the source as an extended source and calculate  $\text{TS}_{\text{ext}}$ . This entire  
 203 procedure was performed twice, once fitting in the 1 GeV to 100 GeV energy range and once  
 204 fitting in the 10 GeV to 100 GeV energy range.

205 For each set of spectral parameters,  $\sim 20,000$  statistically independent simulations  
 206 were performed. For lower-flux spectral models, many of the simulations left the source  
 207 insignificant ( $\text{TS} < 25$ ) and were discarded. Table 1 shows the different spectral models  
 208 used in our study as well as the number of simulations and the average point-like source  
 209 significance. The cumulative density of  $\text{TS}_{\text{ext}}$  is plotted in Figures 3 and 4 and compared to  
 210 the  $\chi_1^2/2$  distribution of Equation 11.

211 Our study shows broad agreement between simulations and Equation 11. To the extent  
 212 that there is a discrepancy, the simulations tended to produce smaller than expected values  
 213 of  $\text{TS}_{\text{ext}}$  which would make the formal significance conservative. Considering the distribution  
 214 in Figures 3 and 4, the choice of a threshold  $\text{TS}_{\text{ext}}$  set to 16 (corresponding to a formal  $4\sigma$   
 215 significance) is reasonable.

---

<sup>3</sup>`gtobssim` is distributed publicly by the FSSC.

### 3.2. Point-like Source Simulations Over a Structured Background

We performed a second set of simulations to show that the theoretical distribution for  $\text{TS}_{\text{ext}}$  is still preserved when the point-like sources are present over a highly-structured diffuse background. Our simulation setup was the same as above except that the sources were simulated on top of and analyzed assuming the presence of the standard Galactic diffuse and isotropic background models used in 2FGL. In our simulations, we selected our sources to have random positions on the sky such that they were within  $5^\circ$  of the Galactic plane. This probes the brightest and most strongly contrasting areas of the Galactic background.

To limit the number of tests, we selected only one flux level for each of the four spectral indices and we performed this test only in the 1 GeV to 100 GeV energy range. As described below, the fluxes were selected so that  $\text{TS} \sim 50$ . We do not expect to be able to spatially resolve sources at lower fluxes than these, and the results for much brighter sources are less likely to be affected by the structured background.

Because the Galactic diffuse emission is highly structured with strong gradients, the point-source sensitivity can vary significantly across the Galactic plane. To account for this, we scaled the flux (for a given spectral index) so that the source always has approximately the same signal-to-noise ratio:

$$F(\vec{x}) = F(\text{GC}) \times \left( \frac{B(\vec{x})}{B(\text{GC})} \right)^{1/2}. \quad (12)$$

Here,  $\vec{x}$  is the position of the simulated source,  $F$  is the integral flux of the source from 100 MeV to 100 GeV,  $F(\text{GC})$  is the same quantity if the source was at the Galactic center,  $B$  is the integral of the Galactic diffuse and isotropic emission from 1 GeV to 100 GeV at the position of the source, and  $B(\text{GC})$  is the same quantity if the source was at the Galactic center. For the four spectral models, Table 1 lists  $F(\text{GC})$  and the average value of  $\text{TS}$ .

For each spectrum, we performed  $\sim 90,000$  simulations. Figure 5 shows the cumulative density of  $\text{TS}_{\text{ext}}$  for each spectrum. For small values of  $\text{TS}_{\text{ext}}$ , there is good agreement between the simulations and theory. For the highest values of  $\text{TS}_{\text{ext}}$ , there is possibly a small discrepancy, but the discrepancy is not statistically significant. Therefore, we are confident we can use  $\text{TS}_{\text{ext}}$  as a robust measure of statistical significance when testing LAT-detected sources for extension.

### 3.3. Extended Source Simulations Over a Structured Background

We also performed a Monte Carlo study to show that incorrectly modeling the spatial extension of an extended source does not substantially bias the spectral fit of the source, although it does alter the value of the TS. To assess this, we simulated the spatially extended ring-type SNR W44. We selected W44 because it is the most significant extended source detected by the LAT that has a non-radially symmetric photon distribution (Abdo et al. 2010g).

W44 was simulated with a power-law spectral model with an integral flux of  $7.12 \times 10^{-8}$   $\text{ph cm}^{-2} \text{s}^{-1}$  in the energy range from 1 GeV to 100 GeV and a spectral index of 2.66 (see Section 7).

W44 was simulated with the elliptical ring spatial model described in Abdo et al. (2010g). For reference, the ellipse has a semi-major axis of  $0^\circ.3$ , a semi-minor axis of  $0^\circ.19$ , a position angle of  $147^\circ$  measured East of celestial North, and the ring’s inner radius is 75% of the outer radius.

We used a simulation setup similar to that described in Section 3.2, but the simulations were over the 2-year interval of the 2FGL catalog. In the simulations, we did not include the finite energy resolution of the LAT to isolate any effects due to changing the assumed spatial model. The fitting code we use also ignores this energy dispersion and the potential bias introduced by this will be discussed in an upcoming paper by the LAT collaboration (Abdo et al. 2012a). In total, we performed 985 independent simulations.

The simulated sources were fit using a point-like spatial model, a radially-symmetric Gaussian spatial model, a uniform disk spatial model, an elliptical disk spatial model, and finally with an elliptical ring spatial model. We obtained the best fit spatial parameters using `pointlike` and, with these parameters, obtained the best fit spectral parameters using `gtlike`.

Figure 6a shows that the significance of W44 in the simulations is very large ( $\text{TS} \sim 3500$ ) for a model with a point-like source hypothesis. Figure 6b shows that the significance of the spatial extension is also large ( $\text{TS}_{\text{ext}} \sim 250$ ). On average  $\text{TS}_{\text{ext}}$  is somewhat larger when fitting the sources with more accurate spatial models. This shows that assuming an incorrect spatial model will cause the source’s significance to be underestimated. Figure 6c shows that the sources were fit better when assuming an elliptical disk spatial model compared to a uniform disk spatial model ( $\text{TS}_{\text{elliptical disk}} - \text{TS}_{\text{disk}} \sim 30$ ). Finally, Figure 6d shows that the sources were fit somewhat better assuming an elliptical ring spatial model compared to an elliptical disk spatial model ( $\text{TS}_{\text{elliptical ring}} - \text{TS}_{\text{elliptical disk}} \sim 9$ ). This shows that the LAT has some additional power to resolve substructure in bright extended sources.

275 Figure 7a and Figure 7b clearly show that no significant bias is introduced by modeling  
 276 the source as extended but with an inaccurate spatial model, while a point-like source model-  
 277 ing results in a  $\sim 10\%$  and  $\sim 0.125$  bias in the fit flux and index, respectively. Furthermore,  
 278 Figure 7c shows that the  $r_{68}$  estimate of the extension size is very mildly biased ( $\sim 10\%$ )  
 279 toward higher values when inaccurate spatial models are used, and thus represents a rea-  
 280 sonable measurement of the true 68% containment radius for the source. For the elliptical  
 281 spatial models,  $r_{68}$  is computed by numeric integration.

#### 282 4. Extended Source Detection Threshold

283 We calculated the LAT flux threshold to detect spatial extent. We define the detection  
 284 threshold as the flux at which the value of  $\text{TS}_{\text{ext}}$  averaged over many statistical realizations  
 285 is  $\langle \text{TS}_{\text{ext}} \rangle = 16$  (corresponding to a formal  $4\sigma$  significance) for a source of a given extension.

286 We used a simulation setup similar to that described in Section 3.1, but instead of point-  
 287 like sources we simulated extended sources with radially-symmetric uniform disk spatial  
 288 models. Additionally, we simulated our sources over the two-year time range included in  
 289 the 2FGL catalog. For each extension and spectral index, we selected a flux range which  
 290 bracketed  $\text{TS}_{\text{ext}} = 16$  and performed an extension test for  $> 100$  independent realizations of  
 291 ten fluxes in the range. We calculated  $\langle \text{TS}_{\text{ext}} \rangle = 16$  by fitting a line to the flux and  $\text{TS}_{\text{ext}}$   
 292 values in the narrow range.

293 Figure 8 shows the threshold for sources of four spectral indices from 1.5 to 3 and  
 294 extensions varying from  $\sigma = 0^\circ.1$  to  $2^\circ.0$ . The threshold is high for small extensions when  
 295 the source is small compared to the size of the PSF. It drops quickly with increasing source  
 296 size and reaches a minimum around  $0^\circ.5$ . The threshold increases for large extended sources  
 297 because the source becomes increasingly diluted by the background. Figure 8 shows the  
 298 threshold using photons with energies between 100 MeV and 100 GeV and also using only  
 299 photons with energies between 1 GeV and 100 GeV. Except for very large or very soft sources,  
 300 the threshold is not substantially improved by including photons with energies between 100  
 301 MeV and 1 GeV. This is also demonstrated in Figure 1 which shows  $\text{TS}_{\text{ext}}$  for the SNR  
 302 IC 443 computed independently in twelve energy bins between 100 MeV and 100 GeV. For  
 303 IC 443, which has a spectral index  $\sim 2.4$  and an extension  $\sim 0^\circ.35$ , almost the entire increase  
 304 in likelihood from optimizing the source extent in the model comes from energies above 1  
 305 GeV. Furthermore, other systematic errors become increasingly large at low energy. For our  
 306 extension search (Section 9), we therefore used only photons with energies above 1 GeV.

307 Figure 9 shows the flux threshold as a function of source extension for different back-

308 ground levels ( $1\times$ ,  $10\times$ , and  $100\times$  the nominal background), different spectral indices, and  
 309 two different energy ranges (1 GeV to 100 GeV and 10 GeV to 100 GeV). The detection  
 310 threshold is higher for sources in regions of higher background. When studying sources only  
 311 at energies above 1 GeV, the LAT detection threshold (defined as the 1 GeV to 100 GeV flux  
 312 at which  $\langle \text{TS}_{\text{ext}} \rangle = 16$ ) depends less strongly on the spectral index of the source. The index  
 313 dependence of the detection threshold is even weaker when considering only photons with  
 314 energies above 10 GeV because the PSF changes little from 10 GeV to 100 GeV. Overlaid  
 315 on Figure 9 are the LAT-detected extended sources that will be discussed in Sections 7 and  
 316 10. The extension thresholds are tabulated in Table 2.

317 Finally, Figure 10 shows the projected detection threshold of the LAT to extension  
 318 with a 10 year exposure against 10 times the isotropic background measured by EGRET.  
 319 This background is representative of the background near the Galactic plane. For small  
 320 extended sources, the threshold improves by a factor larger than the square root of the  
 321 relative exposures because the LAT is signal-limited at high energies where the present  
 322 analysis is most sensitive. For large extended sources, the relevant background is over a  
 323 larger spatial range and so the improvement is closer to a factor corresponding to the square  
 324 root of the relative exposures that is caused by Poisson fluctuations in the background.

## 325 5. Testing Against Source Confusion

326 It is impossible to discriminate using only LAT data between a spatially extended source  
 327 and multiple point-like sources separated by angular distances comparable to or smaller than  
 328 the size of the LAT PSF. To assess the plausibility of source confusion for sources with  
 329  $\text{TS}_{\text{ext}} \geq 16$ , we developed an algorithm to test if a region contains two point-like sources.  
 330 The algorithm works by simultaneously fitting in `pointlike` the positions and spectra of the  
 331 two point-like sources. To help with convergence, it begins by dividing the source into two  
 332 spatially coincident point-like sources and then fitting the sum and difference of the positions  
 333 of the two sources without any limitations on the fit parameters.

After simultaneously fitting the two positions and two spectra, we define  $\text{TS}_{2\text{pts}}$  as twice  
 the increase in the log of the likelihood fitting the region with two point-like sources compared  
 to fitting the region with one point-like source:

$$\text{TS}_{2\text{pts}} = 2 \log(\mathcal{L}_{2\text{pts}}/\mathcal{L}_{\text{ps}}). \quad (13)$$

334 For the following analysis of LAT data,  $\text{TS}_{2\text{pts}}$  was computed by fitting the spectra of the two  
 335 point-like sources in `gtlike` using the best fit positions of the sources found by `pointlike`.

336  $\text{TS}_{2\text{pts}}$  cannot be quantitatively compared to  $\text{TS}_{\text{ext}}$  using a simple likelihood-ratio test to

337 evaluate which model is significantly better because the models are not nested (Protassov et al.  
 338 2002). Even though the comparison of  $\text{TS}_{\text{ext}}$  with  $\text{TS}_{2\text{pts}}$  is not a calibrated test,  $\text{TS}_{\text{ext}} >$   
 339  $\text{TS}_{2\text{pts}}$  indicates that the likelihood for the extended source hypothesis is higher than for two  
 340 point-like sources and we only consider a source to be extended if  $\text{TS}_{\text{ext}} > \text{TS}_{2\text{pts}}$ .

341 We considered using the Bayesian information criterion (BIC, Schwarz 1978) as an  
 342 alternative Bayesian formulation for this test, but it is difficult to apply to LAT data because  
 343 it contains a term including the number of data points. For studying  $\gamma$ -ray sources in LAT  
 344 data, we analyze relatively large regions of the sky to better define the contributions from  
 345 diffuse backgrounds and nearby point sources. This is important for accurately evaluating  
 346 source locations and fluxes but the fraction of data directly relevant to the evaluation of the  
 347 parameters for the source of interest is relatively small.

348 As an alternative, we considered the Akaike information criterion test (AIC, Akaike  
 349 1974). The AIC is defined as  $\text{AIC} = 2k - 2 \log \mathcal{L}$ , where  $k$  is the number of parameters in the  
 350 model. In this formulation, the best hypothesis is considered to be the one that minimizes  
 351 the AIC. The first term penalizes models with additional parameters.

352 The two point-like sources hypothesis has three more parameters than the single ex-  
 353 tended source hypothesis (two more spatial parameters and two more spectral parameters  
 354 compared to one extension parameter), so the comparison  $\text{AIC}_{\text{ext}} < \text{AIC}_{2\text{pts}}$  is formally  
 355 equivalent to  $\text{TS}_{\text{ext}} + 6 > \text{TS}_{2\text{pts}}$ . Our criterion for accepting extension ( $\text{TS}_{\text{ext}} > \text{TS}_{2\text{pts}}$ )  
 356 is thus equivalent to requesting that the AIC-based empirical support for the two point-  
 357 like sources model be “considerably less” than for the extended source model, following the  
 358 classification by Burnham & Anderson (2002).

359 We assessed the power of the  $\text{TS}_{\text{ext}} > \text{TS}_{2\text{pts}}$  test with a Monte Carlo study. We  
 360 simulated one spatially extended source and fit it as both an extended source and as two  
 361 point-like sources using `pointlike`. We then simulated two point-like sources and fit them  
 362 with the same two hypotheses. By comparing the distribution of  $\text{TS}_{2\text{pts}}$  and  $\text{TS}_{\text{ext}}$  computed  
 363 by `pointlike` for the two cases, we evaluated how effective the  $\text{TS}_{\text{ext}} > \text{TS}_{2\text{pts}}$  test is at  
 364 rejecting cases of source confusion as well as how likely it is to incorrectly reject that an  
 365 extended source is spatially extended. All sources were simulated using the same time range  
 366 as in Section 4 against a background 10 times the isotropic background measured by EGRET,  
 367 representative of the background near the Galactic plane.

368 We did this study first in the energy range from 1 GeV to 100 GeV by simulating  
 369 extended sources of flux  $4 \times 10^{-9}$  ph cm $^{-2}$  s $^{-1}$  integrated from 1 GeV to 100 GeV and a power-  
 370 law spectral model with spectral index 2. This spectrum was picked to be representative of  
 371 the new extended sources that were discovered in the following analysis when looking in the

372 1 GeV to 100 GeV energy range (see Section 10). We simulated these sources using uniform  
 373 disk spatial models with extensions varying up to  $1^\circ$ . Figure 11a shows the distribution of  
 374  $TS_{\text{ext}}$  and  $TS_{2\text{pts}}$  and Figure 11c shows the distribution of  $TS_{\text{ext}} - TS_{2\text{pts}}$  as a function of the  
 375 simulated extension of the source for 200 statistically independent simulations.

376 Figure 12a shows the same plot but when fitting two simulated point-like sources each  
 377 with half of the flux of the spatially extended source and with the same spectral index as the  
 378 extended source. Finally, Figure 12c shows the same plot with each point-like source having  
 379 the same flux but different spectral indices. One point-like source had a spectral index of  
 380 1.5 and the other an index of 2.5. These indices are representative of the range of indices of  
 381 LAT-detected sources.

382 The same four plots are shown in Figure 11b, 11d, 12b, and 12d but this time when  
 383 analyzing a source of flux  $10^{-9}$  ph cm $^{-2}$  s $^{-1}$  (integrated from 10 GeV to 100 GeV) only in the  
 384 10 GeV to 100 GeV energy range. This flux is typical of the new extended sources discovered  
 385 using only photons with energies between 10 GeV and 100 GeV (see Section 10).

386 Several interesting conclusions can be made from this study. As one would expect,  
 387  $TS_{\text{ext}} - TS_{2\text{pts}}$  is mostly positive when fitting the simulated extended sources. In the 1 GeV  
 388 to 100 GeV analysis, only 11 of the 200 simulated extended sources had  $TS_{\text{ext}} > 16$  but  
 389 were incorrectly rejected due to  $TS_{2\text{pts}}$  being greater than  $TS_{\text{ext}}$ . In the 10 GeV to 100 GeV  
 390 analysis, only 7 of the 200 sources were incorrectly rejected. From this, we conclude that  
 391 this test is unlikely to incorrectly reject truly spatially extended sources.

392 On the other hand, it is often the case that  $TS_{\text{ext}} > 16$  when testing the two simulated  
 393 point-like sources for extension. This is especially the case when the two sources had the  
 394 same spectral index. Forty out of 200 sources in the 1 GeV to 100 GeV energy range and  
 395 43 out of 200 sources in the 10 GeV to 100 GeV energy range had  $TS_{\text{ext}} > 16$ . But in these  
 396 cases, we always found the single extended source fit to be worse than the two point-like  
 397 source fit. From this, we conclude that the  $TS_{\text{ext}} > TS_{2\text{pts}}$  test is powerful at discarding  
 398 cases in which the true emission comes from two point-like sources.

399 The other interesting feature in Figure 11a and 11b is that for simulated extended  
 400 sources with typical sizes ( $\sigma \sim 0.5^\circ$ ), one can often obtain almost as large an increase in  
 401 likelihood fitting the source as two point-like sources ( $TS_{2\text{pts}} \sim TS_{\text{ext}}$ ). This is because  
 402 although the two point-like sources represent an incorrect spatial model, the second source  
 403 has four additional degrees of freedom (two spatial and two spectral parameters) and can  
 404 therefore easily model much of the extended source and statistical fluctuations in the data.  
 405 This effect is most pronounced when using photons with energies between 1 GeV and 100  
 406 GeV where the PSF is broader.

407 From this Monte Carlo study, we can see the limits of an analysis with LAT data of  
 408 spatially extended sources. Section 3.1 showed that we have a statistical test that finds when  
 409 a LAT source is not well described by the PSF. But this test does not uniquely prove that  
 410 the emission originates from spatially extended emission instead of from multiple unresolved  
 411 sources. Demanding that  $TS_{\text{ext}} > TS_{2\text{pts}}$  is a powerful second test to avoid cases of simple  
 412 confusion of two point-like sources. But it could always be the case that an extended source  
 413 is actually the superposition of multiple point-like or extended sources that could be resolved  
 414 with deeper observations of the region. There is nothing about this conclusion unique to  
 415 analyzing LAT data, but the broad PSF of the LAT and the density of sources expected to  
 416 be GeV emitters in the Galactic plane makes this issue more significant for analyses of LAT  
 417 data. When possible, multiwavelength information should be used to help select the best  
 418 model of the sky.

## 419 6. Test of 2LAC Sources

420 For all following analyses of LAT data, we used the same two-year dataset that was  
 421 used in the 2FGL catalog spanning from 2008 August 4 to 2010 August 1. We applied the  
 422 same acceptance cuts and we used the same P7\_V6 Source class event selection and IRFs  
 423 (Abdo et al. 2012a). When analyzing sources in `pointlike`, we used a circular  $10^\circ$  region  
 424 of interest (ROI) centered on our source and eight energy bins per logarithmic decade in  
 425 energy. When refitting the region in `gtlike` using the best fit spatial and spectral models  
 426 from `pointlike`, we used the ‘binned likelihood’ mode of `gtlike` on a  $14^\circ \times 14^\circ$  ROI with  
 427 a pixel size of  $0^\circ.03$ .

428 Unless explicitly mentioned, we used the same background model as 2FGL to represent  
 429 the Galactic diffuse, isotropic, and Earth limb emission. To compensate for possible residuals  
 430 in the diffuse emission model, the Galactic emission was scaled by a power-law and the  
 431 normalization of the isotropic component was left free. Unless explicitly mentioned, we used  
 432 all 2FGL sources within  $15^\circ$  of our source as our list of background sources and we refit the  
 433 spectral parameters of all sources within  $2^\circ$  of the source.

434 To validate our method, we tested LAT sources associated with AGN for extension.  
 435 GeV emission from AGN is believed to originate from collimated jets. Therefore AGN are  
 436 not expected to be spatially resolvable by the LAT and provide a good calibration source  
 437 to demonstrate that our extension detection method does not misidentify point-like sources  
 438 as being extended. We note that megaparsec-scale  $\gamma$ -ray halos around AGNs have been  
 439 hypothesized to be resolvable by the LAT (Aharonian et al. 1994). However, no such halo  
 440 has been discovered in the LAT data so far (Neronov et al. 2011).



441 Following 2FGL, the LAT Collaboration published the Second LAT AGN Catalog  
 442 (2LAC), a list of high latitude ( $|b| > 10^\circ$ ) sources that had a high probability associa-  
 443 tion with AGN (Ackermann et al. 2011). 2LAC associated 1016 2FGL sources with AGN.  
 444 To avoid systematic problems with AGN classification, we selected only the 885 AGN which  
 445 made it into the clean AGN sub-sample defined in the 2LAC paper. An AGN association  
 446 is considered clean only if it has a high probability of association  $P \geq 80\%$ , if it is the only  
 447 AGN associated with the 2FGL source, and if no analysis flags have been set for the source  
 448 in the 2FGL catalog. These last two conditions are important for our analysis. Source con-  
 449 fusion may look like a spatially extended source and flagged 2FGL sources may correlate  
 450 with unmodeled structure in the diffuse emission.

451 Of the 885 clean AGN, we selected the 733 of these 2FGL sources which were significantly  
 452 detected above 1 GeV and fit each of them for extension. The cumulative density of  $\text{TS}_{\text{ext}}$   
 453 for these AGN is compared to the  $\chi_1^2/2$  distribution of Equation 11 in Figure 13. The  $\text{TS}_{\text{ext}}$   
 454 distribution for the AGN shows reasonable agreement with the theoretical distribution and  
 455 no AGN was found to be significantly extended ( $\text{TS}_{\text{ext}} > 16$ ). The observed discrepancy  
 456 from the theoretical distribution is likely due to small systematics in our model of the LAT  
 457 PSF and the Galactic diffuse emission (see Section 8). The discrepancy could also in a few  
 458 cases be due to confusion with a nearby undetected source. We note that the Monte Carlo  
 459 study of section 3.1 effectively used perfect IRFs and a perfect model of the sky. The overall  
 460 agreement with the expected distribution demonstrates that we can use  $\text{TS}_{\text{ext}}$  as a measure  
 461 of the statistical significance of the detection of the extension of a source.

462 We note that the LAT PSF used in this study was determined empirically by fitting the  
 463 distributions of gamma rays around bright AGN (see Section 8). Finding that the AGN we  
 464 test are not extended is not surprising. This validation analysis is not suitable to reject any  
 465 hypotheses about the existence of megaparsec-scale halos around AGN.

## 466 7. Analysis of Extended Sources Identified in the 2FGL Catalog

467 As further validation of our method for studying spatially extended sources, we re-  
 468 analyzed the twelve spatially extended sources which were included in the 2FGL catalog  
 469 (Nolan et al. 2012). Even though these sources had all been the subjects of dedicated analy-  
 470 ses and separate publications, and had been fit with a variety of spatial models, it is valuable  
 471 to show that these sources are significantly extended using our systematic method assuming  
 472 radially-symmetric uniform disk spatial models. On the other hand, for some of these sources  
 473 a uniform disk spatial model does not well describe the observed extended emission and so  
 474 the dedicated publications by the LAT collaboration provide better models of these sources.

475 Six extended SNRs were included in the 2FGL catalog: W51C, IC 443, W28, W44,  
 476 the Cygnus Loop, and W30 (Abdo et al. 2009a, 2010h,e,g; Katagiri et al. 2011; Abdo et al.  
 477 2012b). Using photons with energies between 1 GeV and 100 GeV, our analysis significantly  
 478 detected that these six SNRs are spatially extended.

479 Two nearby satellite galaxies of the Milky Way the Large Magellanic Cloud (LMC)  
 480 and the Small Magellanic Cloud (SMC) were included in the 2FGL catalog as spatially  
 481 extended sources (Abdo et al. 2010i,b). Their extensions were significantly detected using  
 482 photons with energies between 1 GeV and 100 GeV. Our fit extensions are comparable to  
 483 the published result, but we note that the previous LAT Collaboration publication on the  
 484 LMC used a more complicated two 2D Gaussian surface brightness profile when fitting it  
 485 (Abdo et al. 2010i).

486 Three PWNe, MSH 15–52, Vela X, and HESS J1825–137, were fit as extended sources  
 487 in the 2FGL analysis (Abdo et al. 2010a,f; Grondin et al. 2011). In the present analysis,  
 488 HESS J1825–137 was significantly detected using photons with energies between 10 GeV and  
 489 100 GeV. To avoid confusion with the nearby bright pulsar PSR J1509–5850, MSH 15–52  
 490 had to be analyzed at high energies. Using photons with energies above 10 GeV, we fit the  
 491 extension of MSH 15–52 to be consistent with the published size but with  $TS_{\text{ext}}=6.6$ .

492 Our analysis was unable to resolve Vela X which would have required first removing the  
 493 pulsed photons from the Vela pulsar which was beyond the scope of this paper. Our analysis  
 494 also failed to detect a significant extension for the Centaurus A Lobes because the shape  
 495 of the source is significantly different from a uniform radially-symmetric disk (Abdo et al.  
 496 2010c).

497 Our analysis of these sources is summarized in Table 3. This table includes the best  
 498 fit positions and extensions of these sources when fitting them with a radially-symmetric  
 499 uniform disk model. It also includes the best fit spectral parameters for each source. The  
 500 positions and extensions of Vela X and the Centaurus A Lobes were taken from Abdo et al.  
 501 (2010f,c) and are included in this table for completeness.

## 502 8. Systematic Errors on Extension

503 We developed two criteria for estimating systematic errors on the extensions of the  
 504 sources. First, we estimated a systematic error due to uncertainty in our knowledge of the  
 505 LAT PSF. Before launch, the LAT PSF was determined by detector simulations which were  
 506 verified in accelerator beam tests (Atwood et al. 2009b). However, in-flight data revealed  
 507 a discrepancy above 3 GeV in the PSF compared to the angular distribution of photons

508 from bright AGN (Abdo et al. 2012a). Subsequently, the PSF was fit empirically to bright  
 509 AGN and this empirical parameterization is used in the P7\_V6 IRFs. To account for the  
 510 uncertainty in our knowledge of the PSF, we refit our extended source candidates using the  
 511 pre-flight Monte Carlo representation of the PSF and consider the difference in extension  
 512 found using the two PSFs as a systematic error on the extension of a source. The same  
 513 approach was used in Abdo et al. (2010h). We believe that our parameterization of the PSF  
 514 from bright AGN is substantially better than the Monte Carlo representation of the PSF so  
 515 this systematic error is conservative.

516 We estimated a second systematic error on the extension of a source due to uncertainty  
 517 in our model of the Galactic diffuse emission by using an alternative approach to modeling  
 518 the diffuse emission which takes as input templates calculated by GALPROP<sup>4</sup> but then fits  
 519 each template locally in the surrounding region. The particular GALPROP model that was  
 520 used as input is described in the analysis of the isotropic diffuse emission with LAT data  
 521 (Abdo et al. 2010j). The intensities of various components of the Galactic diffuse emission  
 522 were fitted individually using a spatial distribution predicted by the model. We considered  
 523 separate contributions from cosmic-ray interactions with the molecular hydrogen, the atomic  
 524 and ionized hydrogen, residual gas traced by dust (Grenier et al. 2005), and the interstellar  
 525 radiation field. We further split the contributions from interactions with molecular and  
 526 atomic hydrogen to the Galactic diffuse emission according to the distance from the Galactic  
 527 center in which they are produced. Hence, we replaced the standard diffuse emission model  
 528 by 18 individually fitted templates to describe individual components of the diffuse emission.  
 529 A similar crosscheck was used in an analysis of RX J1713.7–3946 by the LAT Collaboration  
 530 (Abdo et al. 2011).

531 It is not expected that this diffuse model is superior to the standard LAT model obtained  
 532 through an all-sky fit. However, adding degrees of freedom to the background model can  
 533 remove likely spurious sources that correlate with features in the Galactic diffuse emission.  
 534 Therefore, this tests systematics that may be due to imperfect modeling of the diffuse emis-  
 535 sion in the region. Nevertheless, this alternative approach to modeling the diffuse emission  
 536 does not test all systematics related to the diffuse emission model. In particular, because  
 537 the alternative approach uses the same underlying gas maps, it is unable to be used to assess  
 538 systematics due to insufficient resolution of the underlying maps. Structure in the diffuse  
 539 emission that is not correlated with these maps will also not be assessed by this test.

---

<sup>4</sup>GALPROP is a software package for calculating the Galactic  $\gamma$ -ray emission based on a model of cosmic-ray propagation in the Galaxy and maps of the distributions of the components of the interstellar medium (Strong & Moskalenko 1998; Vladimirov et al. 2011). See also <http://galprop.stanford.edu/> for details.

540 We do not expect the systematic error due to uncertainties in the PSF to be correlated  
541 with the systematic error due to uncertainty in the Galactic diffuse emission. Therefore, the  
542 total systematic error on the extension of a source was obtained by adding the two errors in  
543 quadrature.

544 There is another systematic error on the size of a source due to issues modeling nearby  
545 sources in crowded regions of the sky. It is beyond the scope of this paper to address this  
546 systematic error. Therefore, for sources in crowded regions the systematic errors quoted in  
547 this paper may not represent the full set of systematic errors associated with this analysis.

## 548 9. Extended Source Search Method

549 Having demonstrated that we understand the statistical issues associated with analyzing  
550 spatially extended sources (Section 3.1 and 6) and that our method can correctly analyze  
551 the extended sources included in 2FGL (Section 7), we applied this method to search for  
552 new spatially extended GeV sources. The data and general analysis setting is as described  
553 in Section 6.

554 Ideally, we would apply a completely blind and uniform search that tests the extension  
555 of each 2FGL source in the presence of all other 2FGL sources to find a complete list of  
556 all spatially extended sources. As our test of AGN in Section 6 showed, at high Galactic  
557 latitude where the source density is not as large and the diffuse emission is less structured,  
558 this method works well.

559 But this is infeasible in the Galactic plane where we are most likely to discover new  
560 spatially extended sources. In the Galactic plane, this analysis is challenged by our imperfect  
561 model of the diffuse emission and by an imperfect model of nearby sources. The Monte  
562 Carlo study in Section 5 showed that the overall likelihood would greatly increase by fitting  
563 a spatially extended source as two point-like sources so we expect that spatially extended  
564 sources would be modeled in the 2FGL catalog as multiple point-like sources. Furthermore,  
565 the positions of other nearby sources in the region close to an extended source could be  
566 biased by not correctly modeling the extension of the source. The 2FGL catalog contains a  
567 list of sources significant at energies above 100 MeV whereas we are most sensitive to spatial  
568 extension at higher energies. We therefore expect that at higher energies our analysis would  
569 be complicated by 2FGL sources no longer significant and by 2FGL sources whose positions  
570 were biased by diffuse emission at lower energies.

571 To account for these issues, we first produced a large list of possibly extended sources  
572 employing very liberal search criteria and then refined the analysis of the promising can-

573 didates on a case by case basis. Our strategy was to test all point-like 2FGL sources for  
574 extension assuming they had a uniform radially-symmetric disk spatial model and a power-  
575 law spectral model. Although not all extended sources are expected to have a shape very  
576 similar to a uniform disk, Section 2.4 showed that for many spatially extended sources the  
577 wide PSF of the LAT and limited statistics makes this a reasonable approximation. On the  
578 other hand, choosing this spatial model biases us against finding extended sources that are  
579 not well described by a uniform disk model such as shell-type SNRs.

580 Before testing for extension, we automatically removed from the background model all  
581 other 2FGL sources within  $0.5^\circ$  of the source. This distance is somewhat arbitrary, but was  
582 picked in hopes of finding extended sources with sizes on the order of  $\sim 1^\circ$  or smaller. On the  
583 other hand, by removing these nearby background sources we expect to also incorrectly add  
584 to our list of extended source candidates point-like sources that are confused with nearby  
585 sources. To screen out obvious cases of source confusion, we performed the dual localization  
586 procedure described in Section 5 to compare the extended source hypothesis to the hypothesis  
587 of two independent point-like sources.

588 As was shown in Section 4, little sensitivity is gained by using photons with energies  
589 below 1 GeV. In addition, the broad PSF at low energy makes the analysis more susceptible  
590 to systematic errors arising from source confusion due to nearby soft point-like sources and  
591 by uncertainties in our modeling of the Galactic diffuse emission. For these reasons, we  
592 performed our search using only photons with energies between 1 GeV and 100 GeV.

593 We also performed a second search for extended sources using only photons with en-  
594 ergies between 10 GeV and 100 GeV. Although this approach tests the same sources, it is  
595 complementary because the Galactic diffuse emission is even less dominant above 10 GeV  
596 and because source confusion is less of an issue. A similar procedure was used to detect the  
597 spatial extensions of MSH 15–52 and HESS J1825–137 with the LAT (Abdo et al. 2010a;  
598 Grondin et al. 2011).

599 When we applied this test to the 1861 point-like sources in the 2FGL catalog, our  
600 search found 117 extended source candidates in the 1 GeV to 100 GeV energy range and 11  
601 extended source candidates in the 10 GeV to 100 GeV energy range. Most of the extended  
602 sources found above 10 GeV were also found above 1 GeV and in many cases multiple nearby  
603 point-like sources were found to be extended even though they fit the same emission region.  
604 For example, the sources 2FGL J1630.2–4752, 2FGL J1632.4–4753c 2FGL J1634.4–4743c,  
605 and 2FGL J1636.3–4740c were all found to be spatially extended in the 10 GeV to 100 GeV  
606 energy range even though they all fit to similar positions and sizes. For these situations, we  
607 manually discarded all but one of the 2FGL sources.

608 Similarly, many of these sources were confused with nearby point-like sources or influ-  
 609 enced by large-scale residuals in the diffuse emission. To help determine which of these fits  
 610 found truly extended sources and when the extension was influenced by source confusion and  
 611 diffuse emission, we generated a series of diagnostic plots. For each candidate, we generated  
 612 a map of the residual TS by adding a new point-like source of spectral index 2 into the  
 613 region at each position and finding the increase in likelihood when fitting its flux. Figure 14  
 614 shows this map around the most significantly extended source IC 443 when it is modeled  
 615 both as a point-like source and as an extended source. The residual TS map indicates that  
 616 the spatially extended model for IC 443 is a significantly better description of the observed  
 617 photons and that there is no  $TS > 25$  residual in the region after modeling the source as  
 618 being spatially extended. We also generated plots of the sum of all counts within a given  
 619 distance of the source and compared them to the model predictions assuming the emission  
 620 originated from a point-like source. An example radial integral plot is shown for the ex-  
 621 tended source IC 443 in Figure 1. For each source, we also made diffuse-emission-subtracted  
 622 smoothed counts maps (shown for IC 443 in Figure 1).

623 We found by visual inspection that in many cases our results were strongly influenced by  
 624 large-scale residuals in the diffuse emission and hence the extension measure was unreliable.  
 625 This was especially true in our analysis of sources in the 1 GeV to 100 GeV energy range.  
 626 An example of such a case is 2FGL J1856.2+0450c analyzed in the 1 GeV to 100 GeV energy  
 627 range. Figure 15 shows a diffuse-emission-subtracted smoothed counts map for this source  
 628 with the best fit extension of the source overlaid. There appear to be large-scale residuals in  
 629 the diffuse emission in this region along the Galactic plane. As a result, 2FGL J1856.2+0450c  
 630 is fit to an extension of  $\sim 2^\circ$  and the result is statistically significant with  $TS_{\text{ext}} = 45.4$ .  
 631 However, by looking at the residuals it is clear that this complicated region is not well  
 632 modeled. We manually discard sources like this.

633 We only selected extended source candidates in regions that did not appear dominated  
 634 by these issues and where there was a multiwavelength counterpart. Because of these sys-  
 635 tematic issues, this search can not be expected to be complete and it is likely that there are  
 636 other spatially extended sources that this method missed.

637 For each candidate that was not biased by neighboring point-like sources or by large-scale  
 638 residuals in the diffuse emission model, we improved the model of the region by deciding on a  
 639 case by case basis which background point-like sources should be kept. We kept in our model  
 640 the sources that we believed represented physically distinct sources and we removed sources  
 641 that we believed were included in the 2FGL catalog to compensate for residuals induced by  
 642 not modeling the extension of the source. Soft nearby point-like 2FGL sources that were  
 643 not significant at higher energies were frozen to the spectras predicted by 2FGL. When

644 deciding which background sources to keep and which to remove, we used multiwavelength  
 645 information about possibly extended source counterparts to help guide our choice. For each  
 646 extended source presented in Section 10, we describe any modifications from 2FGL of the  
 647 background model that were performed. In Table 6, we summarize the sources in the 2FGL  
 648 catalog that we have concluded here correspond to residuals induced by not modeling the  
 649 extensions of nearby extended sources.

650 The best fit positions of nearby point-like sources can be influenced by the extended  
 651 source and vice versa. Similarly, the best fit positions of nearby point-like sources in the 2FGL  
 652 catalog can be biased by systematic issues at lower energies. Therefore, after selecting the list  
 653 of background sources, we iteratively refit the positions and spectra of nearby background  
 654 sources as well as the positions and extensions of the analyzed spatially extended sources until  
 655 the overall fit converged globally. For each extended source, we will describe the positions  
 656 of any relocalized background sources.

657 After obtaining the overall best fit positions and extensions of all of the sources in  
 658 the region using `pointlike`, we refit the spectral parameters of the region using `gtlike`.  
 659 With `gtlike`, we obtained a second measure of  $TS_{\text{ext}}$ . We only consider a source to be  
 660 extended when both `pointlike` and `gtlike` agree that  $TS_{\text{ext}} \geq 16$ . We further required  
 661 that  $TS_{\text{ext}} \geq 16$  using the alternative approach to modeling the diffuse emission presented  
 662 in Section 8. We then replaced the spatially extended source with two point-like sources  
 663 and refit the positions and spectra of the two point-like sources to calculate  $TS_{2\text{pts}}$ . We only  
 664 consider a source to be spatially extended, instead of being the result of confusion of two  
 665 point-like sources, if  $TS_{\text{ext}} > TS_{2\text{pts}}$ . As was shown in Section 5, this test is fairly powerful  
 666 at removing situations in which the emission actually originates from two distinct point-  
 667 like sources instead of one spatially extended source. On the other hand, it is still possible  
 668 that longer observations could resolve additional structure or new sources that the analysis  
 669 cannot currently detect. Considering the very complicated morphologies of extended sources  
 670 observed at other wavelengths and the high density of possible sources that are expected  
 671 to emit at GeV energies, it is likely that in some of these regions further observations will  
 672 reveal that the emission is significantly more complicated than the simple radially-symmetric  
 673 uniform disk model that we assume.

## 674 10. New Extended Sources

675 Nine extended sources not included in the 2FGL catalog were found by our extended  
 676 source search. Two of these have been previously studied in dedicated publications: RX J1713.7–3946  
 677 and Vela Jr. (Abdo et al. 2011; Tanaka et al. 2011). Two of these sources were found when

678 using photons with energies between 1 GeV and 100 GeV and seven were found when using  
 679 photons with energies between 10 GeV and 100 GeV. For the sources found at energies above  
 680 10 GeV, we restrict our analysis to higher energies because of the issues of source confusion  
 681 and diffuse emission modeling described in Section 9. The spectral and spatial properties  
 682 of these nine sources are summarized in Table 4 and the results of our investigation of sys-  
 683 tematic errors are presented in Table 5. Table 5 also compares the likelihood assuming the  
 684 source is spatially extended to the likelihood assuming that the emission originates from  
 685 two independent point-like sources. For these new extended sources,  $TS_{\text{ext}} > TS_{2\text{pts}}$  so we  
 686 conclude that the GeV emission does not originate from two physically distinct point-like  
 687 sources (see Section 5). Table 5 also includes the results of the extension fits using variations  
 688 of the PSF and the Galactic diffuse model described in Section 8. There is good agreement  
 689 between  $TS_{\text{ext}}$  and the fit size using the standard analysis, the alternative approach to mod-  
 690 eling the diffuse emission, and the alternative PSF. This suggests that the sources are robust  
 691 against mis-modeled features in the diffuse emission model and uncertainties in the PSF.

### 692 10.1. 2FGL J0823.0–4246

693 2FGL J0823.0–4246 was found by our search to be an extended source candidate in the  
 694 1 GeV to 100 GeV energy range and is spatially coincident with the SNR Puppis A. Figure 16  
 695 shows a counts map of this source. There are two nearby 2FGL sources 2FGL J0823.4–4305  
 696 and 2FGL J0821.0–4254 that are also coincident with the SNR but that do not appear  
 697 to represent physically distinct sources. We conclude that these nearby point-like sources  
 698 were included in the 2FGL catalog to compensate for residuals induced by not modeling the  
 699 extension of this source and removed them from our model of the sky. After removing these  
 700 sources, 2FGL J0823.0–4246 was found to have an extension  $\sigma = 0^\circ.37 \pm 0^\circ.03_{\text{stat}} \pm 0^\circ.02_{\text{sys}}$   
 701 with  $TS_{\text{ext}} = 48.0$ . Figure 17 shows the spectrum of this source.

702 Puppis A has been studied in detail in radio (Castelletti et al. 2006), and X-ray (Petre et al.  
 703 1996; Hwang et al. 2008). The fit extension of 2FGL J0823.0–4246 matches well the size of  
 704 Puppis A in X-ray. The distance of Puppis A was estimated at 2.2 kpc (Reynoso et al. 1995,  
 705 2003) and leads to a 1 GeV to 100 GeV luminosity of  $\sim 3 \times 10^{34}$  ergs s<sup>-1</sup>. No molecular  
 706 clouds have been observed directly adjacent to Puppis A (Paron et al. 2008), similar to the  
 707 LAT-detected Cygnus Loop SNR (Katagiri et al. 2011). The luminosity of Puppis A is also  
 708 smaller than that of other SNRs believed to interact with molecular clouds (Abdo et al.  
 709 2009a, 2010h,g,e; Abdo et al. 2010).



## 10.2. 2FGL J0851.7–4635

710

711 2FGL J0851.7–4635 was found by our search to be an extended source candidate in the  
 712 10 GeV to 100 GeV energy range and is spatially coincident with the SNR Vela Jr. This  
 713 source was recently studied by the LAT Collaboration in Tanaka et al. (2011). Figure 18  
 714 shows a counts map of the source. Overlaid on Figure 18 are TeV contours of Vela Jr.  
 715 (Aharonian et al. 2007a). There are three point-like 2FGL sources 2FGL J0848.5–4535,  
 716 2FGL J0853.5–4711, and 2FGL J0855.4–4625 which correlate with the multiwavelength  
 717 emission of this SNR but do not appear to be physically distinct sources. They were most  
 718 likely included in the 2FGL catalog to compensate for residuals induced by not modeling  
 719 the extension of Vela Jr. and were removed from our model of the sky.

720 With this model of the background, 2FGL J0851.7–4635 was found to have an extension  
 721 of  $\sigma = 1^{\circ}15 \pm 0^{\circ}08_{\text{stat}} \pm 0^{\circ}02_{\text{sys}}$  with  $\text{TS}_{\text{ext}} = 86.8$ . The LAT size matches well the TeV  
 722 morphology of Vela Jr. While fitting the extension of 2FGL J0851.7–4635, we iteratively  
 723 relocalized the position of the nearby point-like 2FGL source 2FGL J0854.7–4501 to  $(l, b) =$   
 724  $(266^{\circ}24, 0^{\circ}49)$  to better fit its position at high energies.

## 10.3. 2FGL J1615.0–5051

725

726 2FGL J1615.0–5051 and 2FGL J1615.2–5138 were both found to be extended source  
 727 candidates in the 10 GeV to 100 GeV energy range. Because they are less than  $1^{\circ}$  away  
 728 from each other, they needed to be analyzed simultaneously. 2FGL J1615.0–5051 is spa-  
 729 tially coincident with the extended TeV source HESS J1616–508 and 2FGL J1615.2–5138 is  
 730 coincident with the extended TeV source HESS J1614–518. Figure 19 shows a counts map  
 731 of these sources and overlays the TeV contours of HESS J1616–508 and HESS J1614–518  
 732 (Aharonian et al. 2006). The figure shows that the 2FGL source 2FGL J1614.9–5212 is  
 733 very close to 2FGL J1615.2–5138 and correlates with the same extended TeV source as  
 734 2FGL J1615.2–5138. We concluded that this source was included in the 2FGL catalog to  
 735 compensate for residuals induced by not modeling the extension of 2FGL J1615.2–5138 and  
 736 removed it from our model of the sky.

737 With this model of the sky, we iteratively fit the extensions of 2FGL J1615.0–5051  
 738 and 2FGL J1615.2–5138. 2FGL J1615.0–5051 was found to have an extension  $\sigma = 0^{\circ}32 \pm$   
 739  $0^{\circ}04_{\text{stat}} \pm 0^{\circ}01_{\text{sys}}$  and  $\text{TS}_{\text{ext}} = 16.7$ .

740 The TeV counterpart of 2FGL J1615.0–5051 was fit with a radially-symmetric Gaussian  
 741 surface brightness profile with  $\sigma = 0^{\circ}136 \pm 0^{\circ}008$  (Aharonian et al. 2006). This TeV size  
 742 corresponds to a 68% containment radius of  $r_{68} = 0^{\circ}21 \pm 0^{\circ}01$ , comparable to the LAT size

743  $r_{68} = 0^{\circ}26 \pm 0^{\circ}03$ . Figure 20 shows that the spectrum of 2FGL J1615.0–5051 at GeV energies  
 744 connects to the spectrum of HESS J1616–508 at TeV energies.

745 HESS J1616–508 is located in the region of two SNRs RCW103 (G332.4-04) and Kes 32  
 746 (G332.4+0.1) but is not spatially coincident with either of them (Aharonian et al. 2006).  
 747 HESS J1616–508 is near three pulsars PSR J1614–5048, PSR J1616–5109, and PSR J1617–5055.  
 748 (Torii et al. 1998; Landi et al. 2007a). Only PSR J1617–5055 is energetically capable of  
 749 powering the TeV emission and Aharonian et al. (2006) speculated that HESS J1616–508  
 750 could be a PWN powered by this young pulsar. Because HESS J1616–508 is  $9'$  away from  
 751 PSR J1617–5055, this would require an asymmetric X-ray PWNe to power the TeV emis-  
 752 sion. *Chandra* ACIS observations revealed an underluminous PWN of size  $\sim 1'$  around the  
 753 pulsar that was not oriented towards the TeV emission, rendering this association uncertain  
 754 (Kargaltsev et al. 2009). No other promising counterparts were observed at X-ray and soft  $\gamma$ -  
 755 ray energies by *Suzaku* (Matsumoto et al. 2007), *Swift*/XRT, IBIS/ISGRBI, BeppoSAX and  
 756 *XMM-Newton* (Landi et al. 2007a). Kargaltsev et al. (2009) discovered additional diffuse  
 757 emission towards the center of HESS J1616–508 using archival radio and infrared observa-  
 758 tions. Deeper observations will likely be necessary to understand this  $\gamma$ -ray source.

#### 759 10.4. 2FGL J1615.2–5138

760 2FGL J1615.2–5138 was found to have an extension  $\sigma = 0^{\circ}42 \pm 0^{\circ}04_{\text{stat}} \pm 0.02_{\text{sys}}$  with  
 761  $\text{TS}_{\text{ext}} = 46.5$ . To test for the possibility that 2FGL J1615.2–5138 is not spatially extended  
 762 but instead composed of two point-like sources (one of them represented in the 2FGL catalog  
 763 by 2FGL J1614.9–5212), we refit 2FGL J1615.2–5138 as two point-like sources. Because  
 764  $\text{TS}_{2\text{pts}} = 35.1$  is less than  $\text{TS}_{\text{ext}} = 46.5$ , we conclude that this emission does not originate  
 765 from two closely-spaced point-like sources.

766 2FGL J1615.2–5138 is spatially coincident with the extended TeV source HESS J1614–518.  
 767 H.E.S.S. measured a 2D Gaussian extension of  $\sigma = 0^{\circ}23 \pm 0^{\circ}02$  and  $\sigma = 0^{\circ}15 \pm 0^{\circ}02$   
 768 in the semi-major and semi-minor axis. This corresponds to a 68% containment size of  
 769  $r_{68} = 0^{\circ}35 \pm 0^{\circ}03$  and  $0^{\circ}23 \pm 0^{\circ}03$ , consistent with the LAT size  $r_{68} = 0^{\circ}34 \pm 0^{\circ}03$ . Figure 20  
 770 shows that the spectrum of 2FGL J1615.2–5138 at GeV energies connects to the spectrum  
 771 of HESS J1614–518 at TeV energies. Further data collected by H.E.S.S. in 2007 resolve a  
 772 double peaked structure at TeV energies but no spectral variation across this source, suggest-  
 773 ing that the emission is not the confusion of physically separate sources (Rowell et al. 2008).  
 774 This double peaked structure is also hinted at in the LAT counts map in Figure 19 but is not  
 775 very significant. The TeV source was also detected by CANGAROO-III (Mizukami et al.  
 776 2011).

777 There are five nearby pulsars, but none are luminous enough to provide the energy  
 778 output required to power the  $\gamma$ -ray emission (Rowell et al. 2008). HESS J1614–518 is spa-  
 779 tially coincident with a young open cluster Pismis 22 (Landi et al. 2007b; Rowell et al. 2008).  
 780 *Suzaku* detected two promising X-ray candidates. Source A is an extended source consistent  
 781 with the peak of HESS J1614–518 and source B coincident with Pismis 22 and towards the  
 782 center but in a relatively dim region of HESS J1614–518 (Matsumoto et al. 2008). Three  
 783 hypotheses have been presented to explain this emission: either source A is an SNR powering  
 784 the  $\gamma$ -ray emission; source A is a PWN powered by an undiscovered pulsar in either source A  
 785 or B; and finally that the emission may arise from hadronic acceleration in the stellar winds  
 786 of Pismis 22 (Mizukami et al. 2011).

### 787 10.5. 2FGL J1627.0–2425c

788 2FGL J1627.0–2425c was found by our search to have an extension  $\sigma = 0^\circ.42 \pm 0^\circ.05_{\text{stat}} \pm$   
 789  $0^\circ.16_{\text{sys}}$  with  $\text{TS}_{\text{ext}} = 32.4$  using photons with energies between 1 GeV and 100 GeV. Figure  
 790 21 shows a counts map of this source.

791 This source is in a region of remarkably complicated diffuse emission. Even though it is  
 792  $16^\circ$  from the Galactic plane, this source is on top of the core of the Ophiuchus molecular cloud  
 793 which contains massive star-forming regions that are bright in infrared. The region also has  
 794 abundant molecular and atomic gas traced by CO and H I and significant dark gas found  
 795 only by its association with dust emission (Grenier et al. 2005). Embedded star-forming  
 796 regions make it even more challenging to measure the column density of dust. Infrared and  
 797 CO ( $J = 1 \rightarrow 0$ ) contours are overlaid on Figure 21 and show good spatial correlation with  
 798 the GeV emission (Young et al. 1986; de Geus et al. 1990). This source might represent  $\gamma$ -  
 799 ray emission from the interactions of cosmic rays with interstellar gas which has not been  
 800 accounted for in the LAT diffuse emission model.

### 801 10.6. 2FGL J1632.4–4753c

802 2FGL J1632.4–4753c was found by our search to be an extended source candidate in  
 803 the 10 GeV to 100 GeV energy range but is in a crowded region of the sky. It is spa-  
 804 tially coincident with the TeV source HESS J1632–478. Figure 22a shows a counts map of  
 805 this source and overlays TeV contours of HESS J1632–478 (Aharonian et al. 2006). There  
 806 are six nearby point-like 2FGL sources that appear to represent physically distinct sources  
 807 and were included in our background model: 2FGL J1630.2–4752, 2FGL J1631.7–4720c,

808 2FGL J1632.4–4820c, 2FGL J1635.4–4717c, 2FGL J1636.3–4740c, and 2FGL J1638.0–4703c.  
 809 On the other hand, one point-like 2FGL source 2FGL J1634.4–4743c correlates with the ex-  
 810 tended TeV source and at GeV energies does not appear physically separate. It is very close  
 811 to the position of 2FGL J1632.4–4753c and does not show spatially separated emission in the  
 812 observed photon distribution. We therefore removed this source from our model of the back-  
 813 ground. Figure 22b shows the same region with the background sources subtracted. With  
 814 this model, 2FGL J1632.4–4753c was found to have an extension  $\sigma = 0^{\circ}35 \pm 0^{\circ}04_{\text{stat}} \pm 0^{\circ}02_{\text{sys}}$   
 815 with  $\text{TS}_{\text{ext}} = 26.9$ . While fitting the extension of 2FGL J1632.4–4753c, we iteratively relo-  
 816 calized 2FGL J1635.4–4717c to  $(l, b) = (337^{\circ}23, 0^{\circ}35)$  and 2FGL J1636.3–4740c to  $(l, b) =$   
 817  $(336^{\circ}97, -0^{\circ}07)$ .

818 H.E.S.S. measured an extension of  $\sigma = 0^{\circ}21 \pm 0^{\circ}05$  and  $0^{\circ}06 \pm 0^{\circ}04$  along the semi-  
 819 major and semi-minor axes when fitting HESS J1632–478 with an elliptical 2D Gaussian  
 820 surface brightness profile. This corresponds to a 68% containment size  $r_{68} = 0^{\circ}31 \pm 0^{\circ}08$   
 821 and  $0^{\circ}09 \pm 0^{\circ}06$  along the semi-major and semi-minor axis, consistent with the LAT size  
 822  $r_{68} = 0^{\circ}29 \pm 0^{\circ}04$ . Figure 20 shows that the spectrum of 2FGL J1632.4–4753c at GeV  
 823 energies connects to the spectrum of HESS J1632–478 at TeV energies.

824 Aharonian et al. (2006) argued that HESS J1632–478 is positionally coincident with the  
 825 hard X-ray source IGR J1632–4751 observed by *ASCA*, *INTEGRAL*, and *XMM-Newton*  
 826 (Sugizaki et al. 2001; Tomsick et al. 2003; Rodriguez et al. 2003), but this source is sus-  
 827 pected to be a Galactic X-Ray Binary so the  $\gamma$ -ray extension disfavors the association. Fur-  
 828 ther observations by *XMM-Newton* discovered point-like emission coincident with the peak  
 829 of the H.E.S.S. source surrounded by extended emission of size  $\sim 32'' \times 15''$  (Balbo et al.  
 830 2010). They found in archival MGPS-2 data a spatially coincident extended radio source  
 831 (Murphy et al. 2007) and argued for a single synchrotron and inverse Compton process pro-  
 832 ducing the radio, X-ray, and TeV emission, likely due to a PWN. The increased size at TeV  
 833 energies compared to X-ray energies has previously been observed in several aging PWNe  
 834 including HESS J1825–137 (Gaensler et al. 2003; Aharonian et al. 2006b), HESS J1640–465  
 835 (Aharonian et al. 2006; Funk et al. 2007), and Vela X (Markwardt & Ogelman 1995; Aharonian et al.  
 836 2006c) and can be explained by different synchrotron cooling times for the electrons that  
 837 produce X-rays and  $\gamma$ -rays.

## 838 10.7. 2FGL J1712.4–3941

839 2FGL J1712.4–3941 was found by our search to be spatially extended using photons  
 840 with energies between 1 GeV and 100 GeV. This source is spatially coincident with the  
 841 SNR RX J1713.7–3946 and was recently studied by the LAT Collaboration in Abdo et al.

842 (2011). To avoid issues related to uncertainties in the nearby Galactic diffuse emission at  
 843 lower energy, we restricted our analysis only to energies above 10 GeV. Figure 23 shows a  
 844 smoothed counts map of the source. Above 10 GeV, the GeV emission nicely correlates with  
 845 the TeV contours of RX J1713.7–3946 (Aharonian et al. 2007b) and 2FGL J1712.4–3941 fit  
 846 to an extension  $\sigma = 0^\circ.56 \pm 0^\circ.04_{\text{stat}} \pm 0^\circ.02_{\text{sys}}$  with  $\text{TS}_{\text{ext}} = 38.5$ .

### 847 10.8. 2FGL J1837.3–0700c

848 2FGL J1837.3–0700c was found by our search to be an extended source candidate in  
 849 the 10 GeV to 100 GeV energy range and is spatially coincident with the TeV source  
 850 HESS J1837–069. This source is in a complicated region. Figure 24a shows a smoothed  
 851 counts map of the region and overlays the TeV contours of HESS J1837–069 (Aharonian et al.  
 852 2006). There are two very nearby point-like 2FGL sources, 2FGL J1836.8–0623c and 2FGL J1839.3–0558c,  
 853 that clearly represent distinct sources. On the other hand, there is another source 2FGL J1835.5–0649  
 854 located between the three sources that appears to correlate with the TeV morphology of  
 855 HESS J1837–069 but at GeV energies does not appear to represent a physically distinct  
 856 source. We concluded that this source was included in the 2FGL catalog to compensate  
 857 for residuals induced by not modeling the extension of this source and removed it from our  
 858 model of the sky. Figure 24b shows a counts map of this region after subtracting these  
 859 background sources. After removing 2FGL J1835.5–0649, we tested for source confusion  
 860 by fitting 2FGL J1837.3–0700c instead as two point-like sources. Because  $\text{TS}_{2\text{pts}} = 10.8$  is  
 861 less than  $\text{TS}_{\text{ext}} = 18.5$ , we conclude that this emission does not originate from two nearby  
 862 point-like sources.

863 With this model, 2FGL J1837.3–0700c was found to have an extension  $\sigma = 0^\circ.33 \pm$   
 864  $0^\circ.07_{\text{stat}} \pm 0^\circ.05_{\text{sys}}$ . While fitting the extension of 2FGL J1837.3–0700c, we iteratively re-  
 865 localized the two closest background sources along with the extension of 2FGL J1837.3–0700c  
 866 but their positions did not significantly change. 2FGL J1834.7–0705c moved to  $(l, b) =$   
 867  $(24^\circ.77, 0^\circ.50)$ , 2FGL J1836.8–0623c moved to  $(l, b) = (25^\circ.57, 0^\circ.32)$ .

868 H.E.S.S. measured an extension of  $\sigma = 0^\circ.12 \pm 0^\circ.02$  and  $0^\circ.05 \pm 0^\circ.02$  of the coincident  
 869 TeV source HESS J1837–069 along the semi-major and semi-minor axis when fitting this  
 870 source with an elliptical 2D Gaussian surface brightness profile. This corresponds to a 68%  
 871 containment radius of  $r_{68} = 0^\circ.18 \pm 0^\circ.03$  and  $0^\circ.08 \pm 0^\circ.03$  along the semi-major and semi-  
 872 minor axis. The size is not significantly different from the LAT 68% containment radius of  
 873  $r_{68} = 0^\circ.27 \pm 0^\circ.07$  (less than  $2\sigma$ ). Figure 20 shows that the spectrum of 2FGL J1837.3–0700c  
 874 at GeV energies connects to the spectrum of HESS J1837–069 at TeV energies.

875 HESS J1837–069 is coincident with the hard and steady X-ray source AX J1838.0–0655  
 876 (Bamba et al. 2003). This source was discovered by RXTE to be a pulsar (PSR J1838-  
 877 0655) sufficiently luminous to power the TeV emission and was resolved by *Chandra* to be a  
 878 bright point-like source surrounded by a  $\sim 2'$  nebula (Gotthelf & Halpern 2008). The  $\gamma$ -ray  
 879 emission may be powered by this pulsar. The hard spectral index and spatial extension of  
 880 2FGL J1837.3–0700c disfavor a pulsar origin of the LAT emission and suggest instead that  
 881 the GeV and TeV emission both originate from the pulsar’s wind. There is another X-ray  
 882 point-like source AX J1837.3–0652 near HESS J1837–069 (Bamba et al. 2003) that was also  
 883 resolved into a point-like and diffuse component (Gotthelf & Halpern 2008). Although no  
 884 pulsations have been detected from it, it could also be a pulsar powering some of the  $\gamma$ -ray  
 885 emission.

### 886 10.9. 2FGL J2021.5+4026

887 The source 2FGL J2021.5+4026 is associated with the  $\gamma$ -Cygni SNR and has been specu-  
 888 lated to originate from the interaction of accelerated particles in the SNR with dense molecu-  
 889 lar clouds (Pollock 1985; Gaisser et al. 1998). This association was disfavored when the GeV  
 890 emission from this source was detected to be pulsed (PSR J2021+4026, Abdo et al. 2010k).  
 891 This pulsar was also observed by AGILE (Chen et al. 2011).

892 Looking at the same region at energies above 10 GeV, the pulsar is no longer significant  
 893 but we instead found in our search an extended source candidate. Figure 25 shows a counts  
 894 map of this source and overlays radio contours of  $\gamma$ -Cygni from the Canadian Galactic Plane  
 895 Survey (Taylor et al. 2003). There is good spatial overlap between the SNR and the GeV  
 896 emission.

897 There is a nearby source 2FGL J2019.1+4040 that correlates with the radio emission  
 898 of  $\gamma$ -Cygni and at GeV energies does not appear to represent a physically distinct source.  
 899 We concluded that it was included in the 2FGL catalog to compensate for residuals induced  
 900 by not modeling the extension of  $\gamma$ -Cygni and removed it from our model of the sky. With  
 901 this model, 2FGL J2021.5+4026 was found to have an extension  $\sigma = 0^\circ.63 \pm 0^\circ.05_{\text{stat}} \pm 0^\circ.04_{\text{sys}}$   
 902 with  $\text{TS}_{\text{ext}} = 128.9$ . Figure 17 shows its spectrum. The inferred size of this source at GeV  
 903 energies well matches the radio size of  $\gamma$ -Cygni. Milagro detected a  $4.2\sigma$  excess at energies  
 904  $\sim 30$  TeV from this location (Abdo et al. 2009b,c). VERITAS also detected an extended  
 905 source VER J2019+407 coincident with the SNR above 200 GeV and suggested that the TeV  
 906 emission could be a shock-cloud interaction in  $\gamma$ -Cygni (Weinstein 2009).

## 11. Discussion

907

908 Twelve extended sources were included in the 2FGL catalog and two additional extended  
 909 sources were studied in dedicated publications. Using 2 years of LAT data and a new analysis  
 910 method, we presented the detection of seven additional extended sources. We also reanalyzed  
 911 the spatial extents of the twelve extended sources in the 2FGL catalog and the two additional  
 912 sources. The 21 extended LAT sources are located primarily along the Galactic plane and  
 913 their locations are shown in Figure 26. Most of the LAT-detected extended sources are  
 914 expected to be of Galactic origin as the distances of extragalactic sources (with the exception  
 915 of the local group Galaxies) are typically too large to be able to resolve them at  $\gamma$ -ray energies.

916

917 For the LAT extended sources also seen at TeV energies, Figure 27 shows that there is  
 918 a good correlation between the sizes of the sources at GeV and TeV energies. Even so, the  
 919 sizes of PWNe are expected to vary across the GeV and TeV energy range and the size of  
 920 HESS J1825–137 is significantly larger at GeV than TeV energies (Grondin et al. 2011). It  
 921 is interesting to compare the sizes of other PWN candidates at GeV and TeV energies, but  
 922 definitively measuring a difference in size would require a more in-depth analysis of the LAT  
 data using the same elliptical Gaussian spatial model.

923

924 Figure 28 compares the sizes of the 21 extended LAT sources to the 42 extended H.E.S.S.  
 925 sources.<sup>5</sup> Because of the large field of view and all-sky coverage, the LAT can more easily  
 926 measure larger sources. On the other hand, the better angular resolution of air Cherenkov  
 927 detectors allows them to measure a population of extended sources below the resolution limit  
 928 of the LAT (currently about  $\sim 0.2^\circ$ ). *Fermi* has a 5 year nominal mission lifetime with a  
 929 goal of 10 years of operation. As Figure 10 shows, the low background of the LAT at high  
 930 energies allows its sensitivity to these smaller sources to improve by a factor greater than the  
 931 square root of the relative exposures. With increasing exposure, the LAT will likely begin  
 to detect and resolve some of these smaller TeV sources.

932

933 Figure 29 compares the spectral indices of LAT detected extended sources and of all  
 934 sources in the 2FGL catalog. This, and Tables 3 and 4, show that the LAT observes a popula-  
 935 tion of hard extended sources at energies above 10 GeV. Figure 20 shows that the spectra of  
 936 four of these sources (2FGL J1615.0–5051, 2FGL J1615.2–5138, 2FGL J1632.4–4753c, and  
 937 2FGL J1837.3–0700c) at GeV energies connects to the spectra of their H.E.S.S. counterparts  
 938 at TeV energies. This is also true of Vela Jr., HESS J1825–137 (Grondin et al. 2011), and  
 RX J1713.7–3946 (Abdo et al. 2011). It is likely that the GeV and TeV emission from these

---

<sup>5</sup>The TeV extension of the 42 extended H.E.S.S. sources comes from the H.E.S.S. Source Catalog  
<http://www.mpi-hd.mpg.de/hfm/HESS/pages/home/sources/>.

939 sources originates from the same population of high-energy particles.

940 Many of the TeV-detected extended sources now seen at GeV energies are currently  
941 unidentified and further multiwavelength follow-up observations will be necessary to un-  
942 derstand these particle accelerators. Extending the spectra of these TeV sources towards  
943 lower energies with LAT observations may help to determine the origin and nature of the  
944 high-energy emission.

945 The *Fermi* LAT Collaboration acknowledges generous ongoing support from a number  
946 of agencies and institutes that have supported both the development and the operation of the  
947 LAT as well as scientific data analysis. These include the National Aeronautics and Space  
948 Administration and the Department of Energy in the United States, the Commissariat à  
949 l’Energie Atomique and the Centre National de la Recherche Scientifique / Institut National  
950 de Physique Nucléaire et de Physique des Particules in France, the Agenzia Spaziale Italiana  
951 and the Istituto Nazionale di Fisica Nucleare in Italy, the Ministry of Education, Culture,  
952 Sports, Science and Technology (MEXT), High Energy Accelerator Research Organization  
953 (KEK) and Japan Aerospace Exploration Agency (JAXA) in Japan, and the K. A. Wallen-  
954 berg Foundation, the Swedish Research Council and the Swedish National Space Board in  
955 Sweden.

956 Additional support for science analysis during the operations phase is gratefully acknowl-  
957 edged from the Istituto Nazionale di Astrofisica in Italy and the Centre National d’Études  
958 Spatiales in France.

959 This research has made use of `pywcsgrid2`, an open-source plotting package for Python<sup>6</sup>.  
960 The authors acknowledge the use of `HEALPix`<sup>7</sup> (Górski et al. 2005).

## 961 REFERENCES

- 962 Abdo, A., Ackermann, M., Ajello, M., Baldini, L., Ballet, J., et al. 2010, *ApJ*, 722, 1303  
963 Abdo, A. A., et al. 2009a, *ApJ*, 706, L1  
964 —. 2009b, *ApJS*, 183, 46  
965 —. 2009c, *ApJ*, 700, L127

---

<sup>6</sup><http://leejjoon.github.com/pywcsgrid2/>

<sup>7</sup><http://healpix.jpl.nasa.gov/>



- 966 —. 2009d, *Astroparticle Physics*, 32, 193
- 967 —. 2010a, *ApJ*, 714, 927
- 968 —. 2010b, *A&A*, 523, A46+
- 969 —. 2010c, *Science*, 328, 725
- 970 —. 2010d, *ApJS*, 188, 405
- 971 —. 2010e, *ApJ*, 718, 348
- 972 —. 2010f, *ApJ*, 713, 146
- 973 —. 2010g, *Science*, 327, 1103
- 974 —. 2010h, *ApJ*, 712, 459
- 975 —. 2010i, *A&A*
- 976 —. 2010j, *Physical Review Letters*, 104, 101101
- 977 —. 2010k, *ApJS*, 187, 460
- 978 —. 2011, *ApJ*, 734, 28
- 979 —. 2012a, *ApJS*, in preparation
- 980 —. 2012b, *ApJ*, 744, 80
- 981 Acciari, V. A., et al. 2009, *ApJ*, 698, L133
- 982 —. 2011, *ApJ*, 738, 3
- 983 Ackermann, M., et al. 2011, *ApJ*, 743, 171
- 984 Aharonian, F., et al. 2005, *A&A*, 435, L17
- 985 —. 2006a, *A&A*, 460, 743
- 986 —. 2006b, *A&A*, 460, 365
- 987 —. 2006c, *A&A*, 448, L43
- 988 Aharonian, F., et al. 2006, *ApJ*, 636, 777
- 989 Aharonian, F., et al. 2007a, *ApJ*, 661, 236

- 990 —. 2007b, *A&A*, 464, 235
- 991 —. 2008, *A&A*, 481, 401
- 992 Aharonian, F. A., Coppi, P. S., & Voelk, H. J. 1994, *ApJ*, 423, L5
- 993 Aharonian, F. A., et al. 2007c, *A&A*, 469, L1
- 994 Akaike, H. 1974, *IEEE Transactions on Automatic Control*, 19, 716
- 995 Albert, J., et al. 2006, *Science*, 312, 1771
- 996 Atwood, W. B., et al. 2009a, *ApJ*, 697, 1071
- 997 —. 2009b, *ApJ*, 697, 1071
- 998 Balbo, M., Saouter, P., Walter, R., Pavan, L., Tramacere, A., Pohl, M., & Zurita-Heras,  
999 J.-A. 2010, *A&A*, 520, A111+
- 1000 Baltz, E. A., et al. 2008, *J. Cosmology Astropart. Phys.*, 7, 13
- 1001 Bamba, A., Ueno, M., Koyama, K., & Yamauchi, S. 2003, *ApJ*, 589, 253
- 1002 Burnham, K. P., & Anderson, D. R. 2002, *Model selection and multimodel inference: a*  
1003 *practical information-theoretic approach*, 2nd edn. (Springer), 1–488
- 1004 Castelletti, G., Dubner, G., Golap, K., & Goss, W. M. 2006, *A&A*, 459, 535
- 1005 Chen, A. W., et al. 2011, *A&A*, 525, A33+
- 1006 Dame, T. M. 2011, *ArXiv:1101.1499*
- 1007 de Geus, E. J., Bronfman, L., & Thaddeus, P. 1990, *A&A*, 231, 137
- 1008 Eadie, W. T., Drijard, D., & James, F. E. 1971, *Statistical methods in experimental physics*,  
1009 ed. Eadie, W. T., Drijard, D., & James, F. E.
- 1010 Funk, S., Hinton, J. A., Pühlhofer, G., Aharonian, F. A., Hofmann, W., Reimer, O., &  
1011 Wagner, S. 2007, *ApJ*, 662, 517
- 1012 Gaensler, B. M., Schulz, N. S., Kaspi, V. M., Pivovarov, M. J., & Becker, W. E. 2003, *ApJ*,  
1013 588, 441
- 1014 Gaisser, T. K., Protheroe, R. J., & Stanev, T. 1998, *ApJ*, 492, 219

- 1015 Giordano, F. 2011, in *High-Energy Emission from Pulsars and their Systems*, ed. N. Rea &  
1016 D. F. Torres (Springer), 69–73
- 1017 Górski, K. M., Hivon, E., Banday, A. J., Wandelt, B. D., Hansen, F. K., Reinecke, M., &  
1018 Bartelmann, M. 2005, *ApJ*, 622, 759
- 1019 Gotthelf, E. V., & Halpern, J. P. 2008, *ApJ*, 681, 515
- 1020 Grenier, I. A., Casandjian, J.-M., & Terrier, R. 2005, *Science*, 307, 1292
- 1021 Grondin, M.-H., et al. 2011, *ApJ*, 738, 42
- 1022 Hwang, U., Petre, R., & Flanagan, K. A. 2008, *ApJ*, 676, 378
- 1023 James, F., & Roos, M. 1975, *Comput. Phys. Commun.*, 10, 343
- 1024 Kargaltsev, O., Pavlov, G. G., & Wong, J. A. 2009, *The Astrophysical Journal*, 690, 891
- 1025 Katagiri, H., et al. 2011, *ApJ*, 741, 44
- 1026 Kerr, M. 2011, PhD in physics, University of Washington
- 1027 King, I. 1962, *AJ*, 67, 471
- 1028 Krause, J., Carmona, E., & Reichardt, I. 2011, in (Presented at the 2011 Fermi Symposium,  
1029 Rome Italy)
- 1030 Landi, R., de Rosa, A., Dean, A. J., Bassani, L., Ubertini, P., & Bird, A. J. 2007a, *MNRAS*,  
1031 380, 926
- 1032 Landi, R., Masetti, N., Bassani, L., Cellone, S. A., Romero, G. E., Ubertini, P., & Dean,  
1033 A. J. 2007b, *The Astronomer’s Telegram*, 1047, 1
- 1034 Markwardt, C. B., & Ogelman, H. 1995, *Nature*, 375, 40
- 1035 Matsumoto, H., et al. 2007, *PASJ*, 59, 199
- 1036 —. 2008, *PASJ*, 60, 163
- 1037 Mattox, J. R., et al. 1996, *ApJ*, 461, 396
- 1038 Mizukami, T., et al. 2011, *ApJ*, 740, 78
- 1039 Murphy, T., Mauch, T., Green, A., Hunstead, R. W., Piestrzynska, B., Kels, A. P., &  
1040 Sztajer, P. 2007, *MNRAS*, 382, 382

- 1041 Neronov, A., Semikoz, D. V., Tinyakov, P. G., & Tkachev, I. I. 2011, *A&A*, 526, A90
- 1042 Nolan, P. L., et al. 2012, *ApJS*, 199, 31
- 1043 Paron, S., Dubner, G., Reynoso, E., & Rubio, M. 2008, *A&A*, 480, 439
- 1044 Petre, R., Becker, C. M., & Winkler, P. F. 1996, *ApJ*, 465, L43+
- 1045 Pollock, A. M. T. 1985, *A&A*, 150, 339
- 1046 Protassov, R., van Dyk, D. A., Connors, A., Kashyap, V. L., & Siemiginowska, A. 2002,  
1047 *ApJ*, 571, 545
- 1048 Reynoso, E. M., Dubner, G. M., Goss, W. M., & Arnal, E. M. 1995, *AJ*, 110, 318
- 1049 Reynoso, E. M., Green, A. J., Johnston, S., Dubner, G. M., Giacani, E. B., & Goss, W. M.  
1050 2003, *MNRAS*, 345, 671
- 1051 Rodriguez, J., Tomsick, J. A., Foschini, L., Walter, R., Goldwurm, A., Corbel, S., & Kaaret,  
1052 P. 2003, *A&A*, 407, L41
- 1053 Rowell, G., Horns, D., Fukui, Y., & Moriguchi, Y. 2008, in *American Institute of Physics*  
1054 *Conference Series*, Vol. 1085, American Institute of Physics Conference Series, ed.  
1055 F. A. Aharonian, W. Hofmann, & F. Rieger, 241–244
- 1056 Schwarz, G. 1978, *The Annals of Statistics*, 6, pp. 461
- 1057 Sreekumar, P., et al. 1998, *The Astrophysical Journal*, 494, 523
- 1058 Strong, A. W., & Moskalenko, I. V. 1998, *ApJ*, 509, 212
- 1059 Sugizaki, M., Mitsuda, K., Kaneda, H., Matsuzaki, K., Yamauchi, S., & Koyama, K. 2001,  
1060 *ApJS*, 134, 77
- 1061 Tanaka, T., et al. 2011, *ApJ*, 740, L51
- 1062 Taylor, A. R., et al. 2003, *AJ*, 125, 3145
- 1063 Tomsick, J. A., Lingenfelter, R., Walter, R., Rodriguez, J., Goldwurm, A., Corbel, S., &  
1064 Kaaret, P. 2003, *IAU Circ.*, 8076, 1
- 1065 Torii, K., et al. 1998, *ApJ*, 494, L207+
- 1066 Vladimirov, A. E., et al. 2011, *Computer Physics Communications*, 182, 1156

<sup>1067</sup> Weekes, T. C., et al. 1989, ApJ, 342, 379

<sup>1068</sup> Weinstein, A. 2009, ArXiv:0912.4492

<sup>1069</sup> Young, E. T., Lada, C. J., & Wilking, B. A. 1986, ApJ, 304, L45

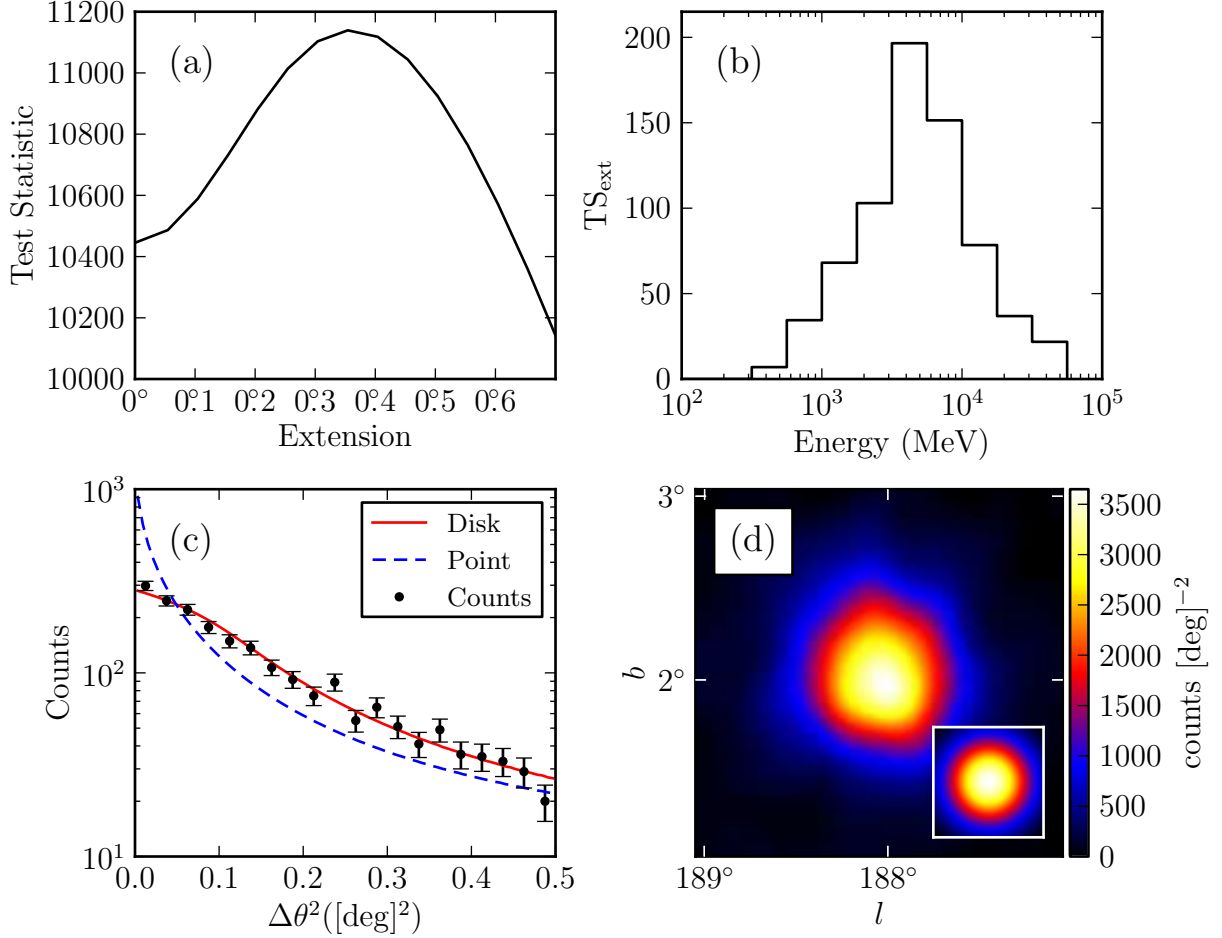


Fig. 1.— Counts maps and TS profiles for the SNR IC 443. (a) TS vs. extension of the source. (b)  $TS_{\text{ext}}$  for individual energy bands. (c) observed radial profile of counts in comparison to the expected profiles for a spatially extended source (solid and colored red in the online version) and for a point-like source (dashed and colored blue in the online version). (d) smoothed counts map after subtraction of the diffuse emission compared to the smoothed LAT PSF (inset). Both were smoothed by a  $0.1^\circ$  2D Gaussian kernel. Plots (a), (c), and (d) use only photons with energies between 1 GeV and 100 GeV. Plots (c) and (d) include only photons which converted in the front part of the tracker and have an improved angular resolution (Atwood et al. 2009a).

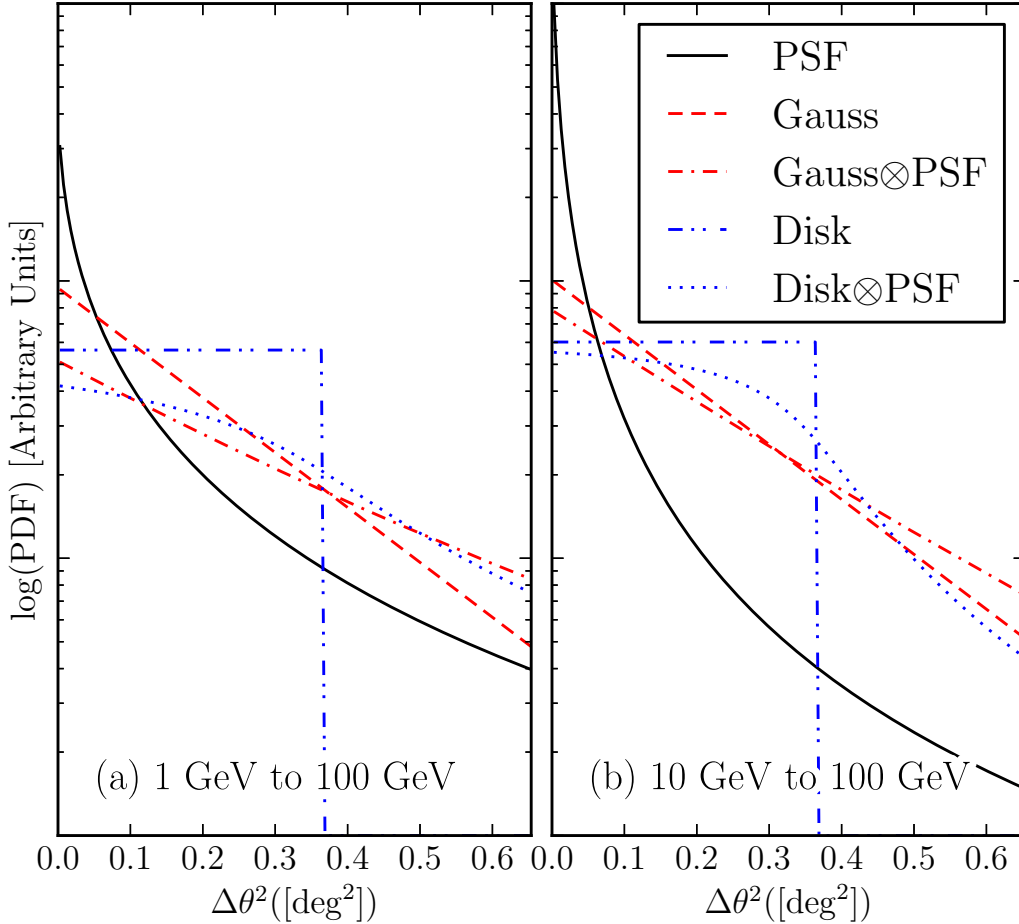


Fig. 2.— A comparison of a 2D Gaussian and uniform disk spatial model of extended sources before and after convolving with the PSF for two energy ranges. The solid black line is the PSF that would be observed for a power-law source of spectral index 2. The dashed line and the dash-dotted lines are the brightness profile of a Gaussian with  $r_{68} = 0.5$  and the convolution of this profile with the LAT PSF respectively (colored red in the online version). The dash-dot-dotted and the dot-dotted lines are the brightness profile of a uniform disk with  $r_{68} = 0.5$  and the convolution of this profile with the LAT PSF respectively (colored blue in the online version).

Table 1. Monte Carlo Spectral Parameters

Spectral Index	Flux <sup>(a)</sup> ( $\text{ph cm}^{-2} \text{s}^{-1}$ )	$N_{1-100\text{GeV}}$	$\langle \text{TS} \rangle_{1-100\text{GeV}}$	$N_{10-100\text{GeV}}$	$\langle \text{TS} \rangle_{10-100\text{GeV}}$
Isotropic Background					
1.5	$3 \times 10^{-7}$	18938	22233	18938	8084
	$10^{-7}$	19079	5827	19079	2258
	$3 \times 10^{-8}$	19303	1276	19303	541
	$10^{-8}$	19385	303	19381	142
	$3 \times 10^{-9}$	18694	62	12442	43
2	$10^{-6}$	18760	22101	18760	3033
	$3 \times 10^{-7}$	18775	4913	18775	730
	$10^{-7}$	18804	1170	18803	192
	$3 \times 10^{-8}$	18836	224	15256	50
	$10^{-8}$	17060	50	...	...
2.5	$3 \times 10^{-6}$	18597	19036	18597	786
	$10^{-6}$	18609	4738	18608	208
	$3 \times 10^{-7}$	18613	954	15958	53
	$10^{-7}$	18658	203	...	...
	$3 \times 10^{-8}$	14072	41	...	...
3	$10^{-5}$	18354	19466	18354	215
	$3 \times 10^{-6}$	18381	4205	15973	54
	$10^{-6}$	18449	966	...	...
	$3 \times 10^{-7}$	18517	174	...	...
	$10^{-7}$	13714	41	...	...
Galactic Diffuse and Isotropic Background <sup>(b)</sup>					
1.5	$2.3 \times 10^{-8}$	90741	63	...	...
2	$1.2 \times 10^{-7}$	92161	60	...	...
2.5	$4.5 \times 10^{-7}$	86226	47	...	...
3	$2.0 \times 10^{-6}$	94412	61	...	...

<sup>(a)</sup>Integral 100 MeV to 100 GeV flux.

<sup>(b)</sup>For the Galactic simulations, the quoted fluxes are the fluxes for sources placed in the Galactic center. The actual fluxes are scaled by Equation 12.

Note. — A list of the spectral models of the simulated point-like sources which were tested for extension. For each model, the number of statistically independent simulations and the average value of TS is also tabulated. The top rows are the simulations on top of an isotropic background and the bottom rows are the simulations on top of the Galactic diffuse and isotropic background.



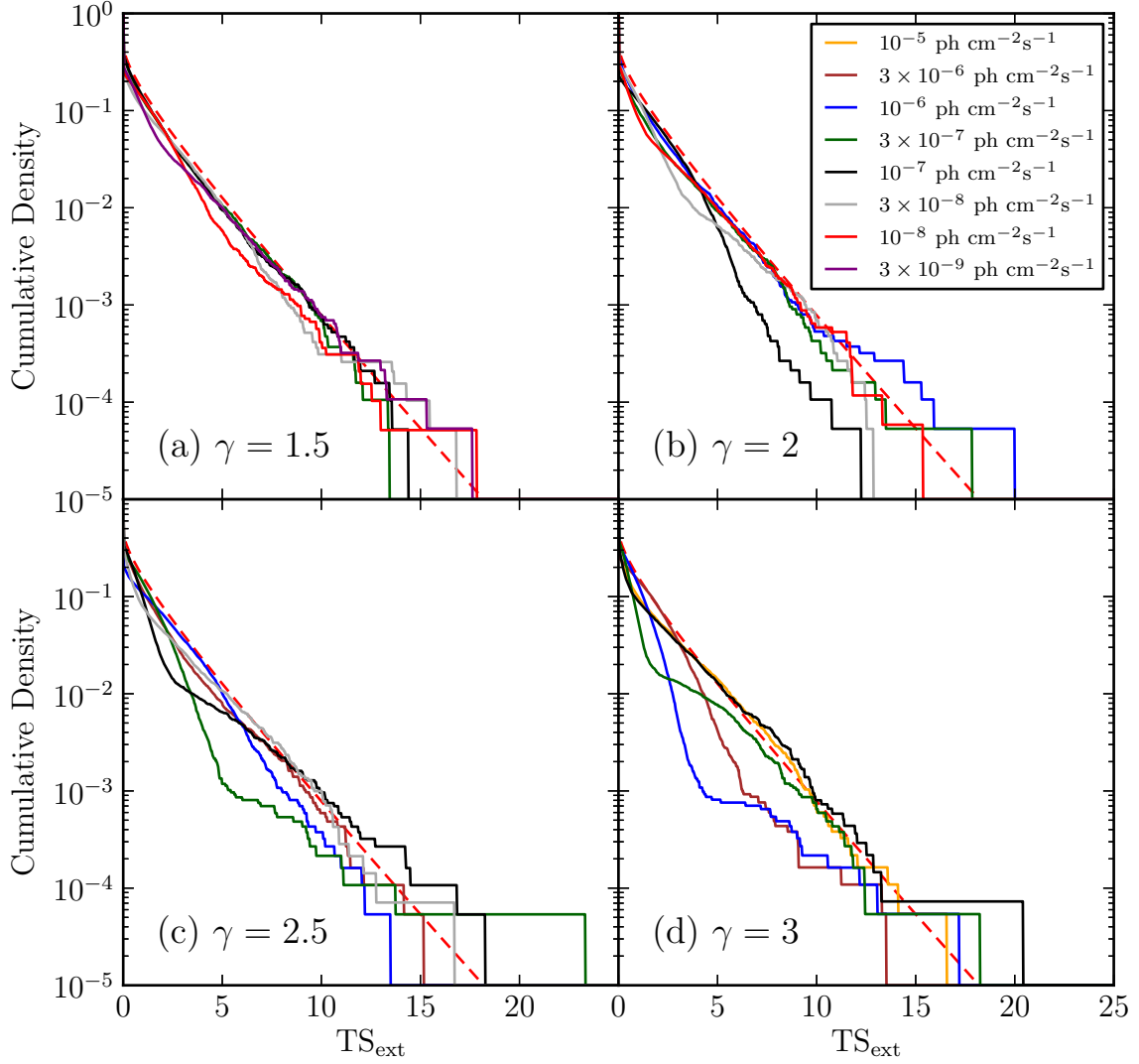


Fig. 3.— Cumulative distribution of the TS for the extension test when fitting simulated point-like sources in the 1 GeV to 100 GeV energy range. The four plots represent simulated sources of different spectral indices and the different lines (colored in the online version) represent point-like sources with different 100 MeV to 100 GeV integral fluxes. The dashed line (colored red) is the cumulative density function of Equation 11.

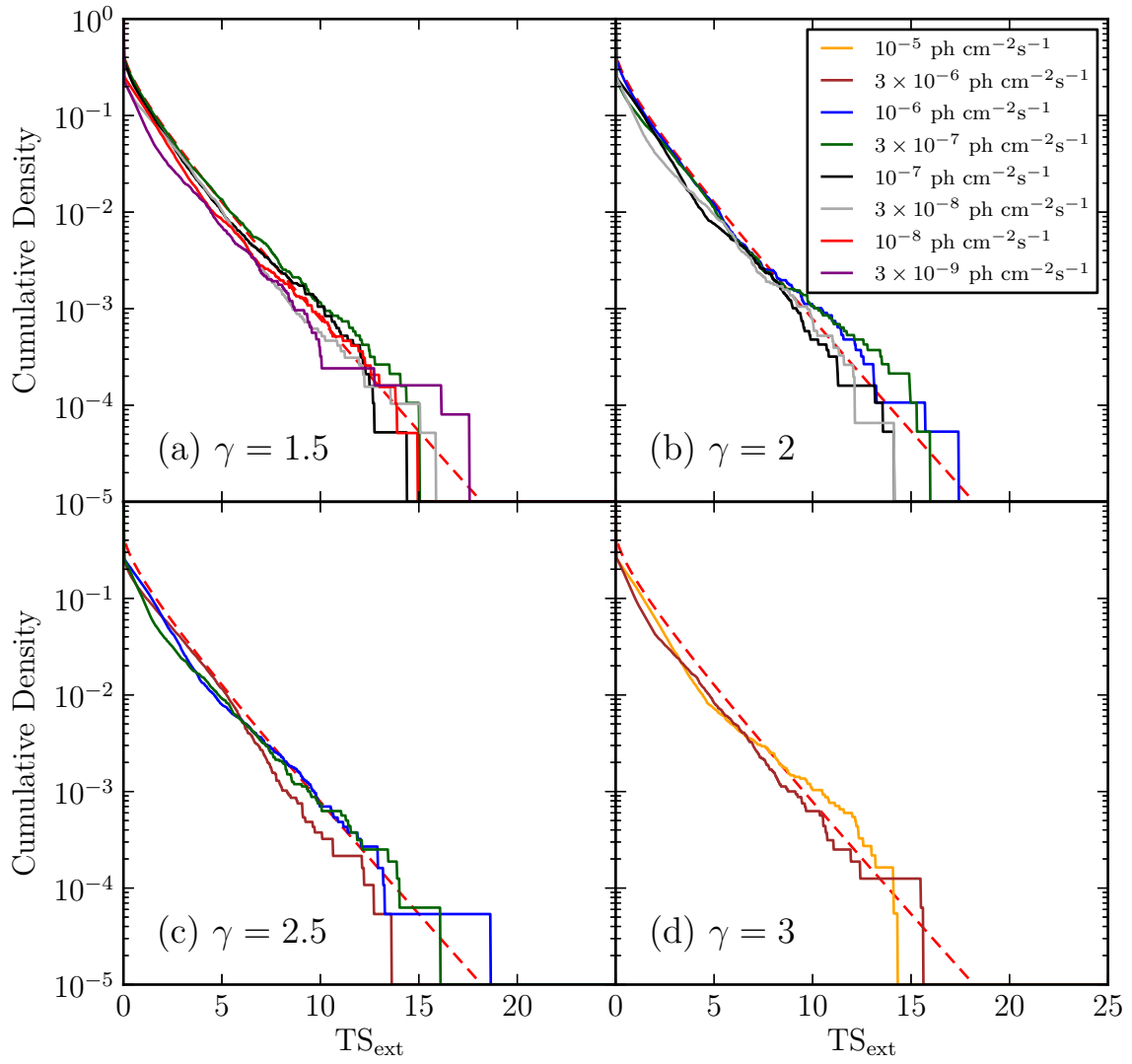


Fig. 4.— The same plot as Figure 3 but fitting in the 10 GeV to 100 GeV energy range.

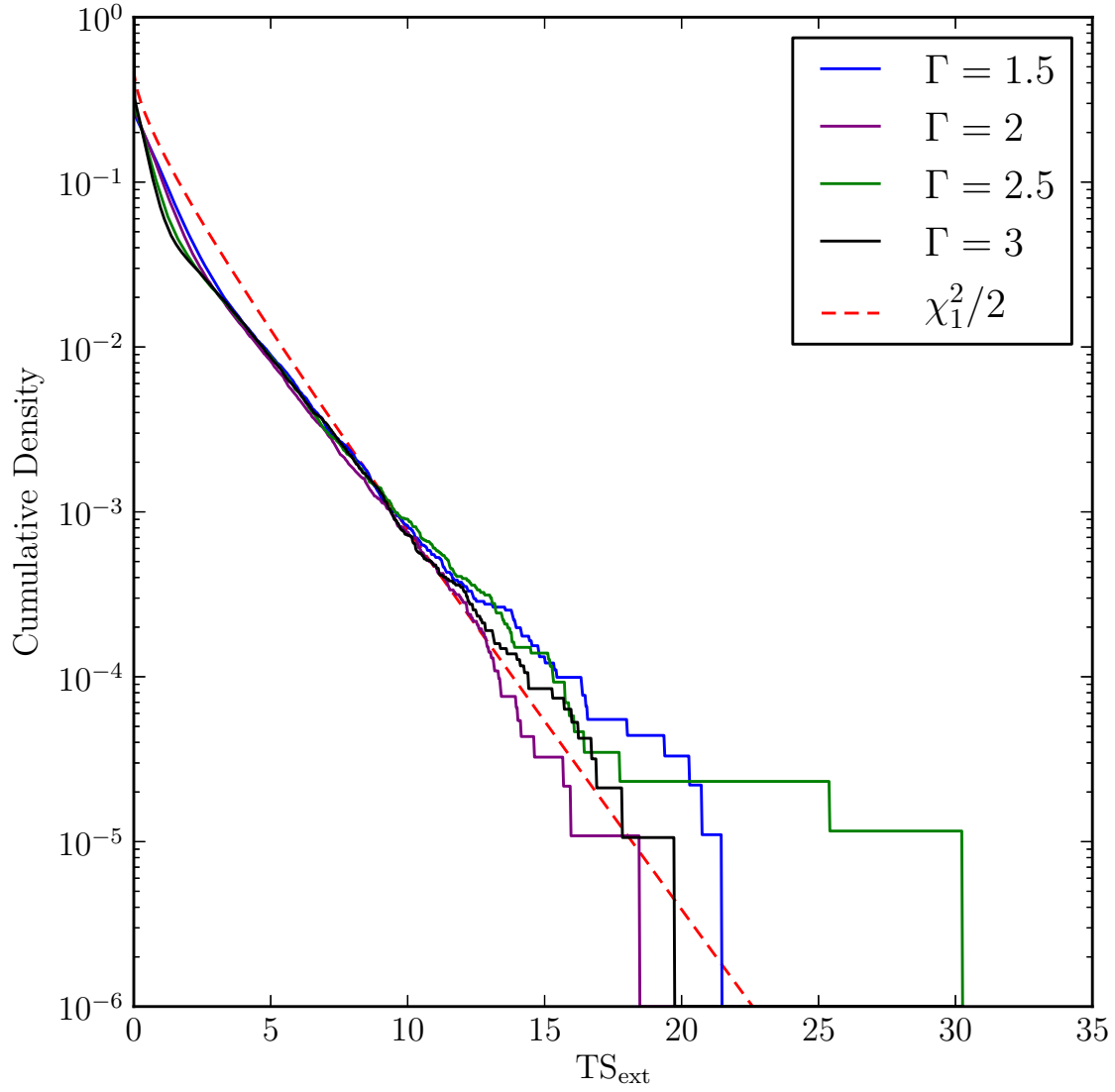


Fig. 5.— Cumulative distribution of  $TS_{\text{ext}}$  for sources simulated on top of the Galactic diffuse and isotropic background.

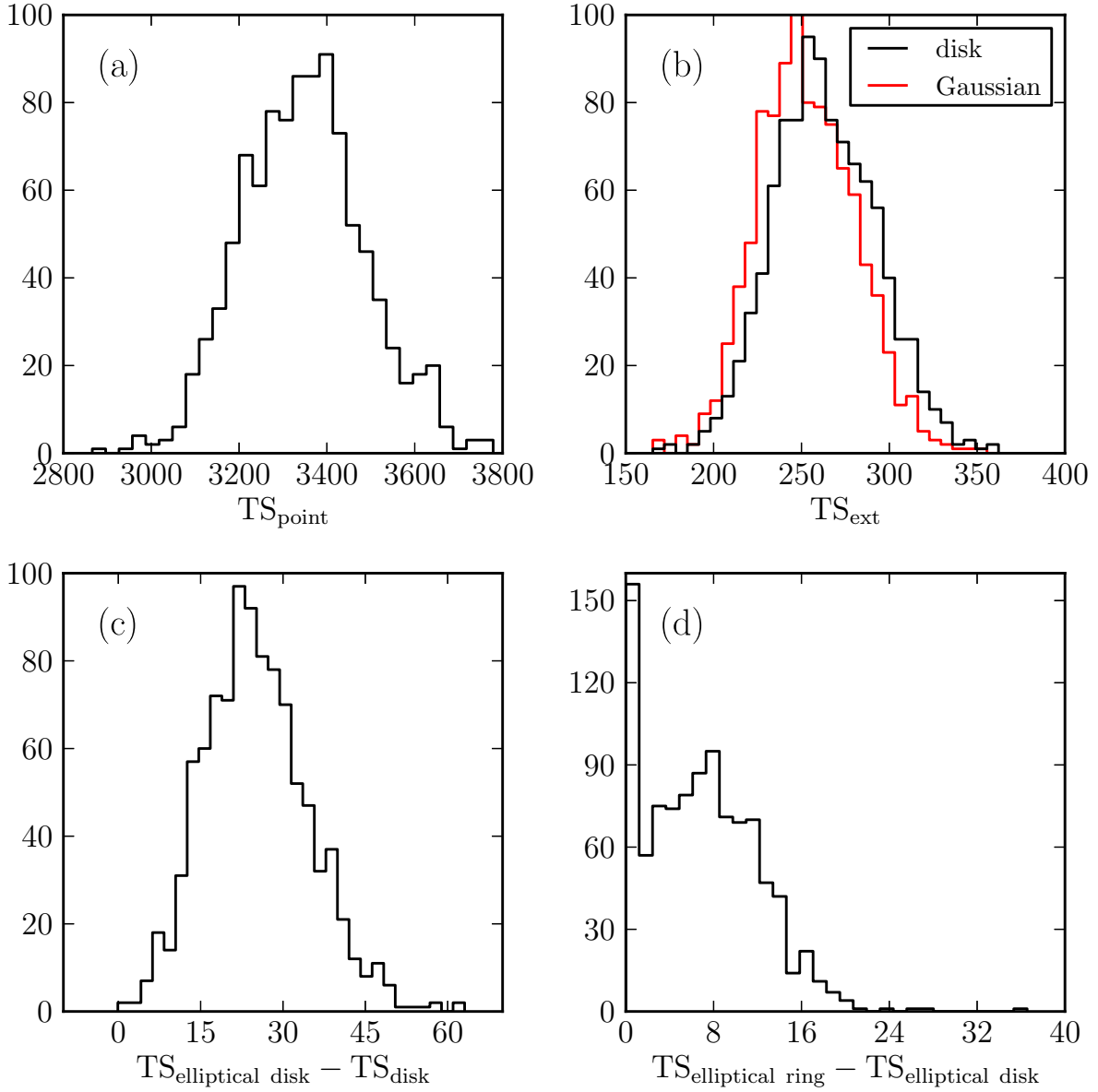


Fig. 6.— The distribution of TS values when fitting 985 statistically independent simulations of W44. (a) is the distribution of TS values when fitting W44 as a point-like source and (b) is the distribution of  $TS_{\text{ext}}$  when fitting the source with a uniform disk or a radially-symmetric Gaussian spatial model. (c) is the distribution of the change in TS when fitting the source with an elliptical disk spatial model compared to fitting it with a radially-symmetric disk spatial model and (d) when fitting the source with an elliptical ring spatial model compared to an elliptical disk spatial model.

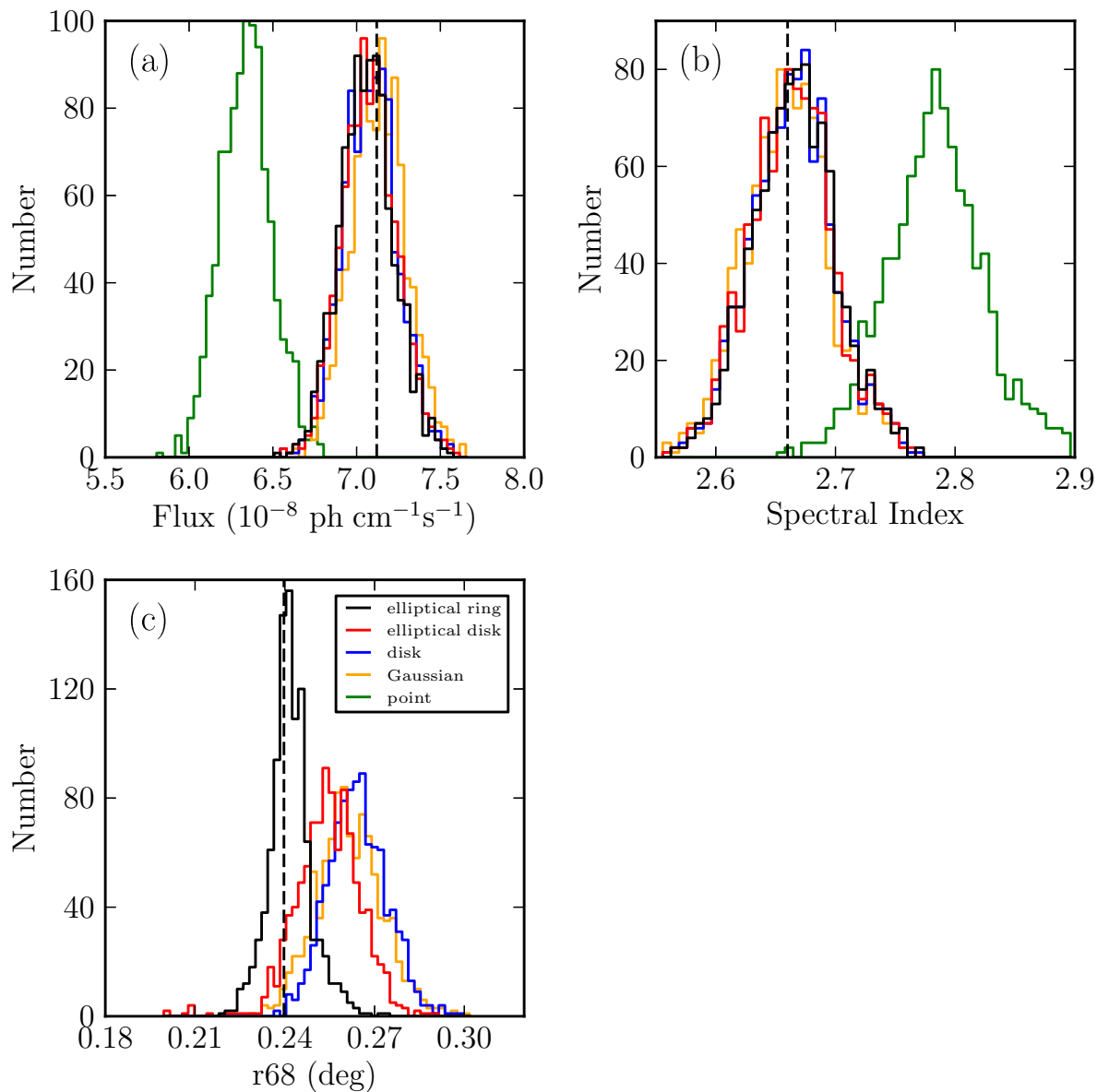


Fig. 7.— The distribution of fit parameters for the Monte Carlo simulations of W44. The plots show the distribution of best fit (a) flux (b) spectral index and (c) 68% containment radius. The dashed vertical lines represent the simulated values of the parameters.

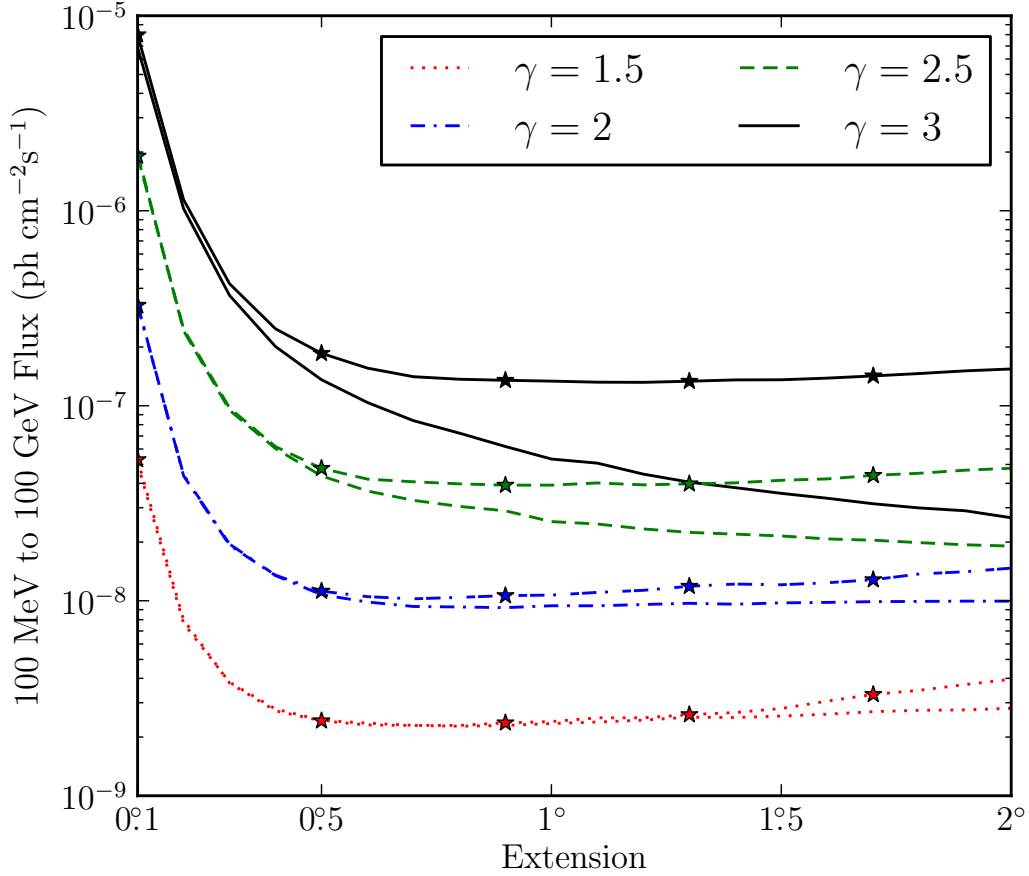


Fig. 8.— The detection threshold to resolve an extended source with a uniform disk model for a two-year exposure. All sources have an assumed power-law spectrum and the different line styles (colors in the electronic version) correspond to different simulated spectral indices. The lines with no markers correspond to the detection threshold using photons with energies between 100 MeV and 100 GeV, while the lines with star-shaped markers correspond to the threshold using photons with energies between 1 GeV and 100 GeV.

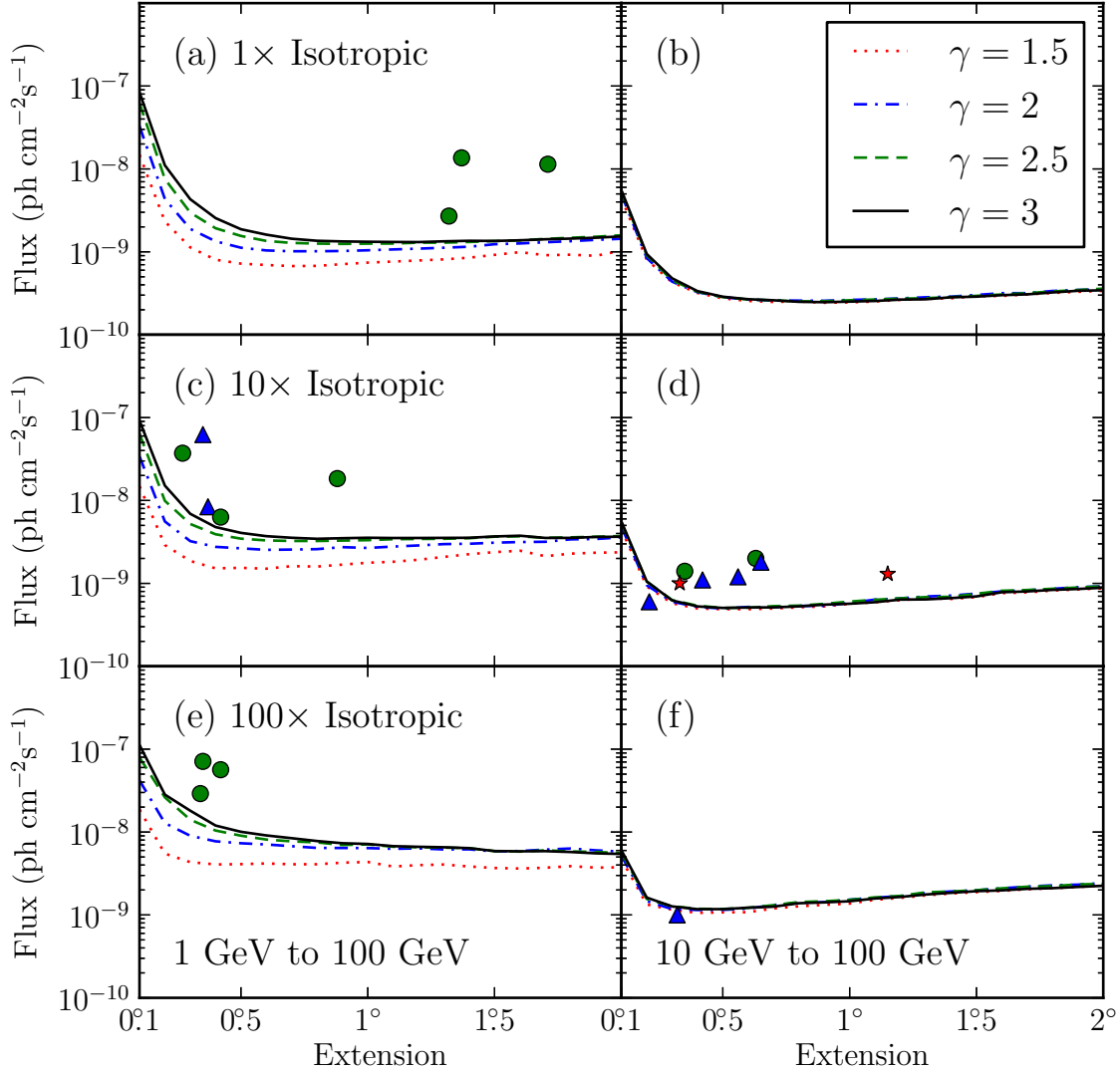


Fig. 9.— The LAT detection threshold for four spectral indices and three backgrounds ( $1\times$ ,  $10\times$ , and  $100\times$  the Sreekumar-like isotropic background) for a two-year exposure. The left-hand plots are the detection threshold when using photons with energies between 1 GeV and 100 GeV and the right-hand plots are the detection threshold when using photons with energies between 10 GeV and 100 GeV. The flux is integrated only in the selected energy range. Overlaid on this plot are the LAT-detected extended sources placed by the magnitude of the nearby Galactic diffuse emission and the energy range they were analyzed with. The star-shaped markers (colored red in the electronic version) are sources with a spectral index closer to 1.5, the triangular markers (colored blue) an index closer to 2, and the circular markers (colored green) an index closer to 2.5. The triangular marker in plot (d) below the sensitivity line is MSH 15–52.

Table 2. Extension Detection Threshold

$\gamma$	BG	0.1	0.2	0.3	0.4	0.5	0.6	0.7	0.8	0.9	1.0	1.1	1.2	1.3	1.4	1.5	1.6	1.7	1.8	1.9	2.0
E>1 GeV																					
1.5	1×	148.1	23.3	11.3	8.0	7.2	6.9	6.7	6.8	7.1	7.4	7.6	7.9	8.1	8.5	9.2	9.9	9.1	9.2	9.0	10.3
	10×	148.4	29.0	18.7	15.2	15.4	15.0	16.1	16.0	16.8	17.7	18.2	19.3	20.9	22.5	23.8	24.8	21.3	22.8	23.4	23.7
	100×	186.8	55.0	43.4	40.7	41.0	41.8	40.9	40.9	42.7	43.6	38.4	39.9	40.6	38.4	36.9	36.3	37.1	38.8	37.2	37.6
2	1×	328.4	43.4	18.9	13.4	11.2	10.4	10.2	10.2	10.2	10.4	10.7	10.9	11.2	11.5	12.4	12.6	13.0	13.4	14.0	14.4
	10×	341.0	55.9	32.3	27.6	26.5	25.4	25.6	25.9	27.4	26.8	27.8	28.7	29.8	30.1	31.0	31.5	31.7	34.0	34.3	35.9
	100×	420.5	128.3	90.2	77.3	73.3	70.8	67.5	64.3	64.2	64.1	62.8	63.6	61.7	61.9	58.4	59.0	61.4	63.3	60.1	58.1
2.5	1×	627.1	75.6	29.8	19.3	15.5	13.5	12.8	12.6	12.5	12.5	12.6	12.9	12.9	13.1	13.5	13.7	14.3	14.8	15.2	15.8
	10×	638.9	99.1	52.1	39.1	34.6	33.0	32.5	32.5	32.8	33.2	34.1	34.3	34.5	35.1	36.6	36.9	35.5	36.0	36.5	37.3
	100×	795.0	262.1	140.9	104.3	90.4	81.2	77.2	75.1	69.7	70.9	66.5	65.6	64.9	64.0	58.9	58.1	60.2	58.4	57.5	55.8
3	1×	841.5	110.6	43.2	25.5	18.7	16.1	14.4	13.6	13.3	13.2	13.1	13.1	13.4	13.6	13.5	13.8	14.2	14.4	14.8	15.4
	10×	921.6	151.3	69.1	47.8	40.7	37.1	35.5	34.5	35.1	35.5	35.3	35.3	35.4	35.5	36.8	37.6	35.3	35.4	36.3	36.6
	100×	1124.1	282.9	181.1	119.8	100.7	91.1	84.3	77.9	73.3	71.8	67.6	66.4	65.5	63.9	59.0	58.6	58.8	57.5	55.4	54.4
E>10 GeV																					
1.5	1×	44.6	8.0	4.3	3.2	2.7	2.6	2.5	2.5	2.4	2.5	2.5	2.6	2.7	2.8	2.9	2.9	3.1	3.2	3.3	3.4
	10×	45.2	9.2	5.8	5.0	4.9	4.9	5.0	5.2	5.3	5.7	5.9	6.3	6.6	6.5	6.8	7.6	7.8	8.2	8.5	8.7
	100×	47.3	13.4	11.6	10.6	10.8	10.8	12.0	12.7	13.2	13.7	15.3	16.1	17.2	18.2	18.9	19.5	20.4	21.0	21.7	22.9
2	1×	49.7	8.4	4.4	3.3	2.8	2.6	2.6	2.6	2.6	2.6	2.7	2.7	2.8	2.9	3.0	3.2	3.2	3.4	3.5	3.5
	10×	48.6	9.5	6.0	5.2	5.0	5.2	5.2	5.3	5.4	5.8	6.4	6.6	7.0	7.1	7.5	8.0	8.3	8.6	9.0	9.2
	100×	51.8	14.7	11.8	11.5	11.5	11.9	13.2	14.0	14.3	15.3	16.2	16.9	18.4	19.2	19.8	21.0	22.0	22.8	23.2	24.3
2.5	1×	53.1	9.1	4.5	3.3	2.8	2.7	2.6	2.5	2.5	2.6	2.7	2.7	2.8	2.8	2.9	3.1	3.2	3.3	3.5	3.6
	10×	53.7	10.5	6.3	5.4	5.1	5.1	5.3	5.4	5.7	6.0	6.3	6.6	6.8	6.9	7.5	8.1	8.3	8.6	8.9	9.2
	100×	57.0	15.6	12.7	11.9	11.8	12.2	13.1	14.3	14.6	15.2	16.3	17.0	18.8	19.2	19.9	21.0	21.9	22.3	23.3	23.7
3	1×	55.5	9.4	4.8	3.4	2.9	2.7	2.6	2.5	2.5	2.5	2.6	2.7	2.7	2.8	2.9	3.0	3.1	3.2	3.4	3.4
	10×	56.0	10.5	6.2	5.3	5.1	5.1	5.1	5.3	5.5	5.7	5.9	6.4	6.4	6.6	7.0	7.8	8.0	8.3	8.6	8.9
	100×	60.3	16.2	12.7	11.7	11.8	12.2	12.6	13.8	14.2	14.6	15.8	16.5	17.6	18.5	19.4	19.8	20.7	21.0	21.8	22.5

Note. — The detection threshold to resolve spatially extended sources with a uniform disk spatial model for a two-year exposure. The threshold is calculated for sources of varying energy ranges, spectral indices, and background levels. The sensitivity was calculated against a Sreekumar-like isotropic background and the second column is the factor that the simulated background was scaled by. The remaining columns are varying sizes of the source. The table quotes integral fluxes in the analyzed energy range (1 GeV to 100 GeV or 10 GeV to 100 GeV) in units of  $10^{-10}$   $\text{ph cm}^{-2} \text{s}^{-1}$ .



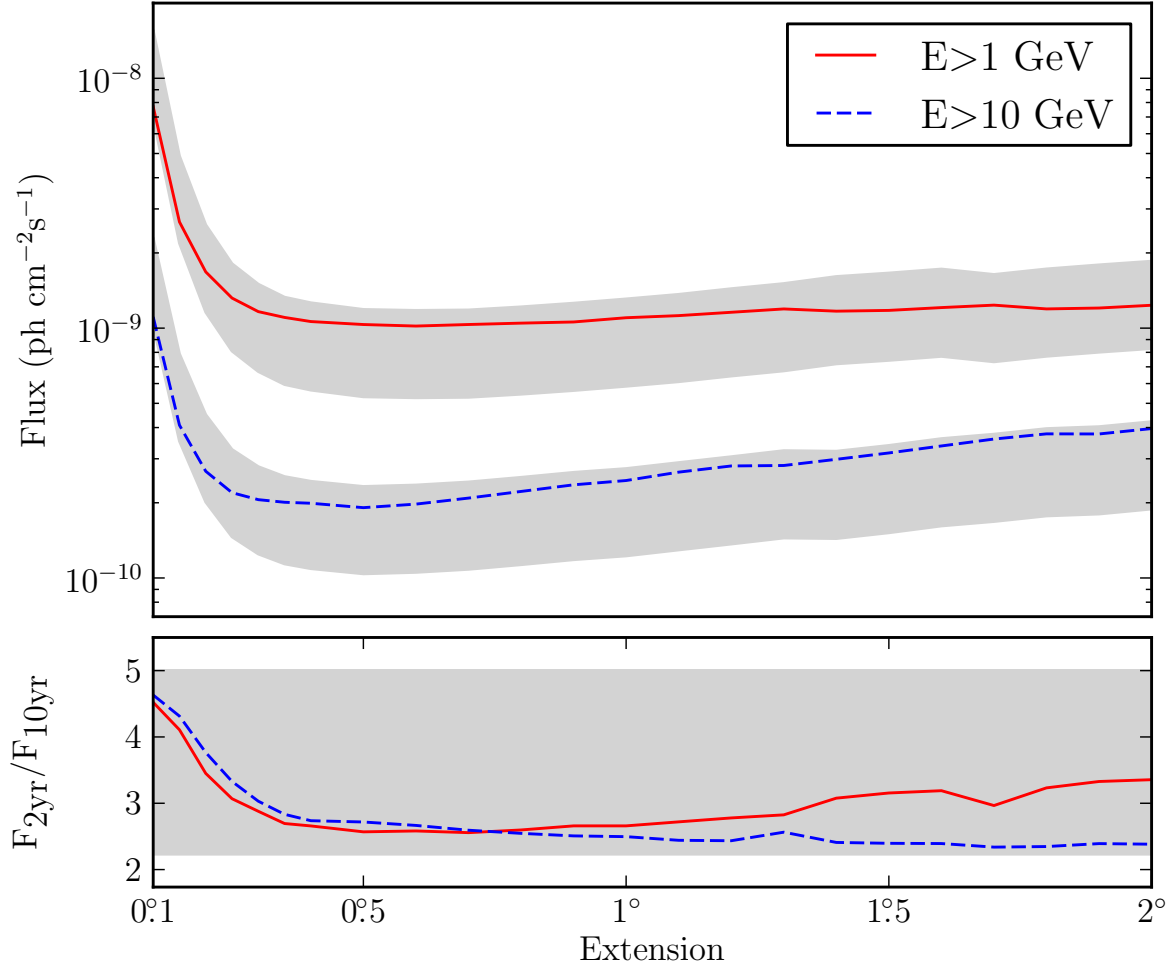


Fig. 10.— The projected detection threshold of the LAT to extension after 10 years for a power-law source of spectral index 2 against 10 times the isotropic background in the energy range from 1 GeV to 100 GeV (solid line colored red in the electronic version) and 10 GeV to 100 GeV (dashed line colored blue). The shaded gray regions represent the detection threshold assuming the sensitivity improves from 2 to 10 years by the square root of the exposure (top edge) and linearly with exposure (bottom edge). The lower plot shows the factor increase in sensitivity. For small extended sources, the detection threshold of the LAT to the extension of a source will improve by a factor larger than the square root of the exposure.

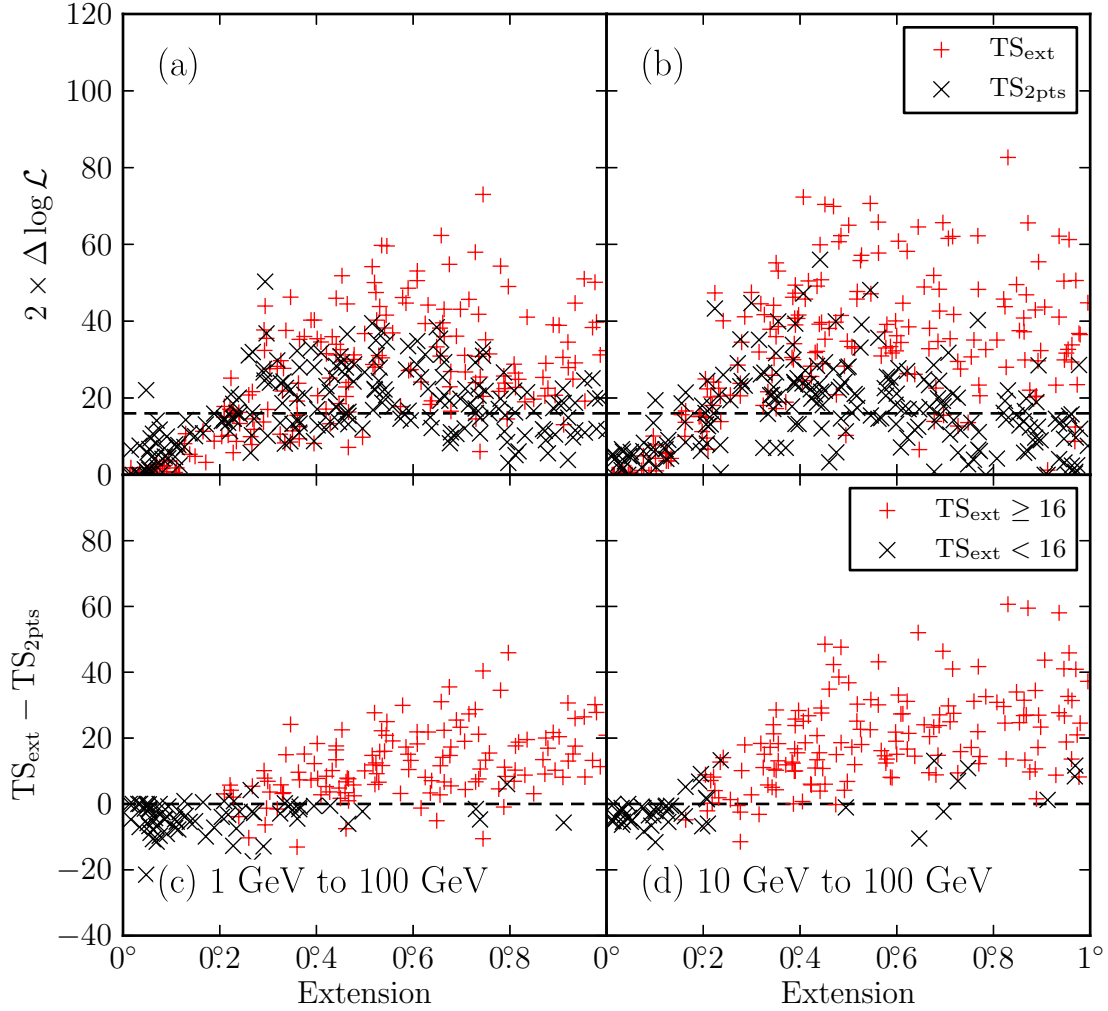


Fig. 11.— (a) and (b) are the distribution of  $TS_{\text{ext}}$  and of  $TS_{2\text{pts}}$  when fitting simulated spatially extended sources of varying sizes as both an extended source and as two point-like sources. (c) and (d) are the distribution of  $TS_{\text{ext}} - TS_{2\text{pts}}$  for the same simulated sources. (a) and (c) represent sources fit in the 1 GeV to 100 GeV energy range and (b) and (d) represent sources fit in the 10 GeV to 100 GeV energy range. In (c) and (d), the plus-shaped markers (colored red in the electronic version) are fits where  $TS_{\text{ext}} \geq 16$ .

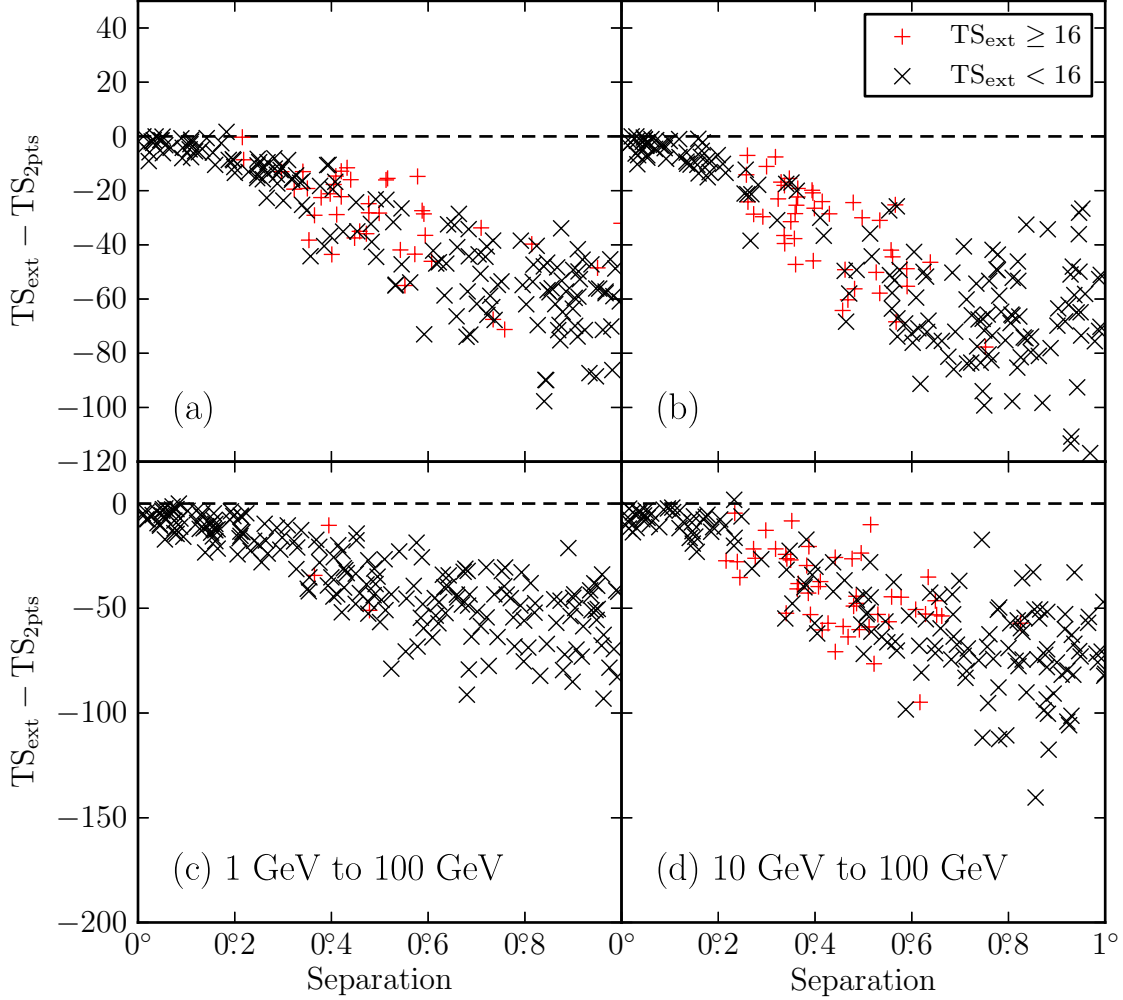


Fig. 12.— The distribution of  $TS_{\text{ext}} - TS_{2\text{pts}}$  when fitting two simulated point-like sources of varying separations as both an extended source and as two point-like sources. (a), and (b) represent simulations of two point-like sources with the same spectral index and (c) and (d) represent simulations of two point-like sources with different spectral indices. (a) and (c) fit the simulated sources in the 1 GeV to 100 GeV energy range and (b) and (d) fit in the 10 GeV to 100 GeV energy range. The plus-shaped markers (colored red in the electronic version) are fits where  $TS_{\text{ext}} \geq 16$ .

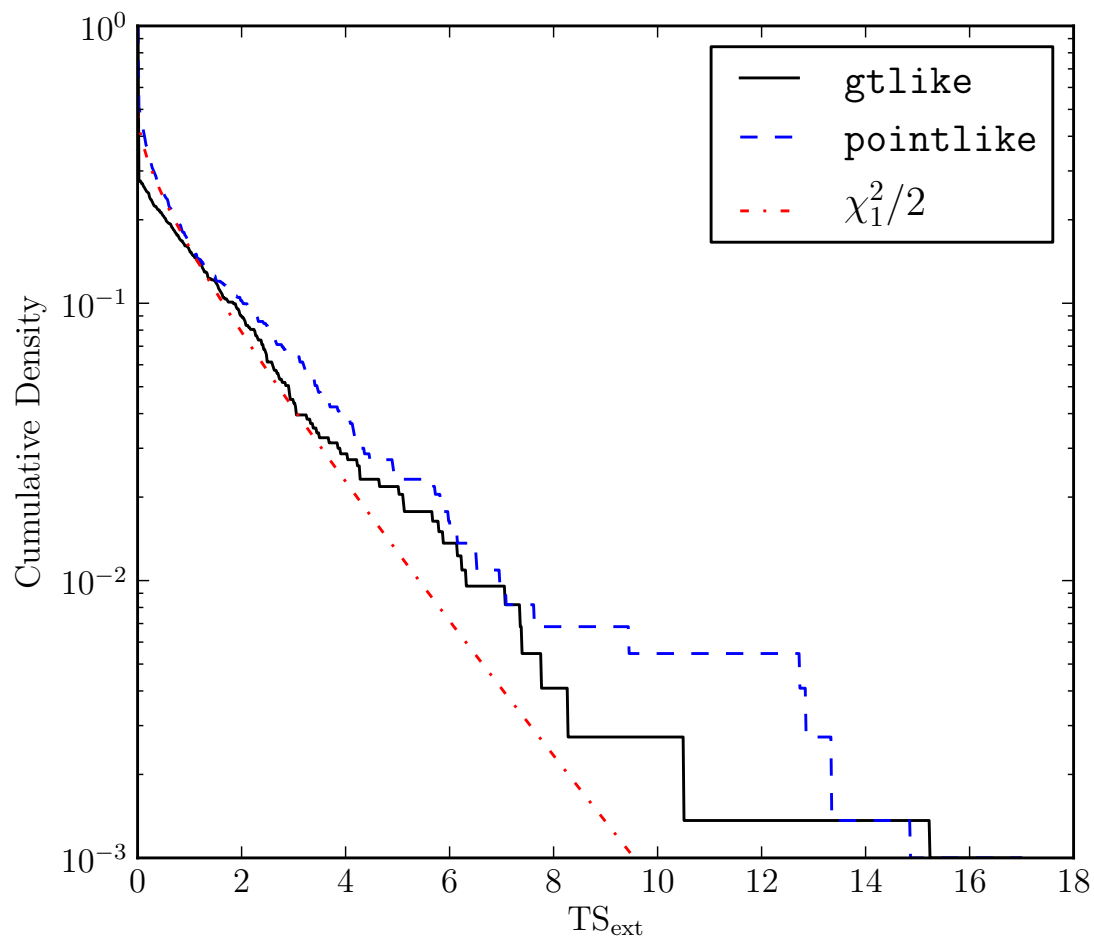


Fig. 13.— The cumulative density of  $TS_{\text{ext}}$  for the 733 clean AGN in 2LAC that were significant above 1 GeV calculated with `pointlike` (dashed line colored blue in the electronic version) and with `gtlike` (solid line colored black). AGN are too far and too small to be resolved by the LAT. Therefore, the cumulative density of  $TS_{\text{ext}}$  is expected to follow a  $\chi_1^2/2$  distribution (Equation 11, the dash-dotted line colored red).

Table 3. Analysis of the twelve extended sources included in the 2FGL catalog

Name	GLON (deg.)	GLAT (deg.)	$\sigma$ (deg.)	TS	TS <sub>ext</sub>	Pos Err (deg.)	Flux <sup>(a)</sup>	Index
E>1 GeV								
SMC	302.59	-44.42	$1.32 \pm 0.15 \pm 0.31$	95.0	52.9	0.14	$2.7 \pm 0.3$	$2.48 \pm 0.19$
LMC	279.26	-32.31	$1.37 \pm 0.04 \pm 0.11$	1127.9	909.9	0.04	$13.6 \pm 0.6$	$2.43 \pm 0.06$
IC 443	189.05	3.04	$0.35 \pm 0.01 \pm 0.04$	10692.9	554.4	0.01	$62.4 \pm 1.1$	$2.22 \pm 0.02$
Vela X	263.34	-3.11	0.88					
Centaurus A	309.52	19.42	$\sim 10$					
W28	6.50	-0.27	$0.42 \pm 0.02 \pm 0.05$	1330.8	163.8	0.01	$56.5 \pm 1.8$	$2.60 \pm 0.03$
W30	8.61	-0.20	$0.34 \pm 0.02 \pm 0.02$	464.8	76.0	0.02	$29.1 \pm 1.5$	$2.56 \pm 0.05$
W44	34.69	-0.39	$0.35 \pm 0.02 \pm 0.02$	1917.0	224.8	0.01	$71.2 \pm 0.5$	$2.66 \pm 0.00$
W51C	49.12	-0.45	$0.27 \pm 0.02 \pm 0.04$	1823.4	118.9	0.01	$37.2 \pm 1.3$	$2.34 \pm 0.03$
Cygnus Loop	74.21	-8.48	$1.71 \pm 0.05 \pm 0.06$	357.9	246.0	0.06	$11.4 \pm 0.7$	$2.50 \pm 0.10$
E>10 GeV								
MSH 15-52 <sup>(b)</sup>	320.39	-1.22	$0.21 \pm 0.04 \pm 0.04$	76.3	6.6	0.03	$0.6 \pm 0.1$	$2.20 \pm 0.22$
HESS J1825-137 <sup>(b)</sup>	17.56	-0.47	$0.65 \pm 0.04 \pm 0.02$	59.7	33.8	0.05	$1.6 \pm 0.2$	$1.63 \pm 0.22$

<sup>(a)</sup>Integral Flux in units of  $10^{-9}$  ph cm<sup>-2</sup> s<sup>-1</sup> and integrated in the fit energy range (either 1 GeV to 100 GeV or 10 GeV to 100 GeV).

<sup>(b)</sup>The discrepancy in the best fit spectra of MSH 15-52 and HESS J1825-137 compared to Abdo et al. (2010a) and Grondin et al. (2011) is due to fitting over a different energy range.

Note. — All sources were fit using a radially-symmetric uniform disk spatial model. GLON and GLAT are Galactic longitude and latitude of the best fit extended source respectively. The first error on  $\sigma$  is statistical and the second is systematic (see Section 8). The errors on the integral fluxes and the spectral indices are statistical

only. Pos Err is the error on the position of the source. Vela X and the Centaurus A Lobes were not fit in our analysis but are included for completeness.

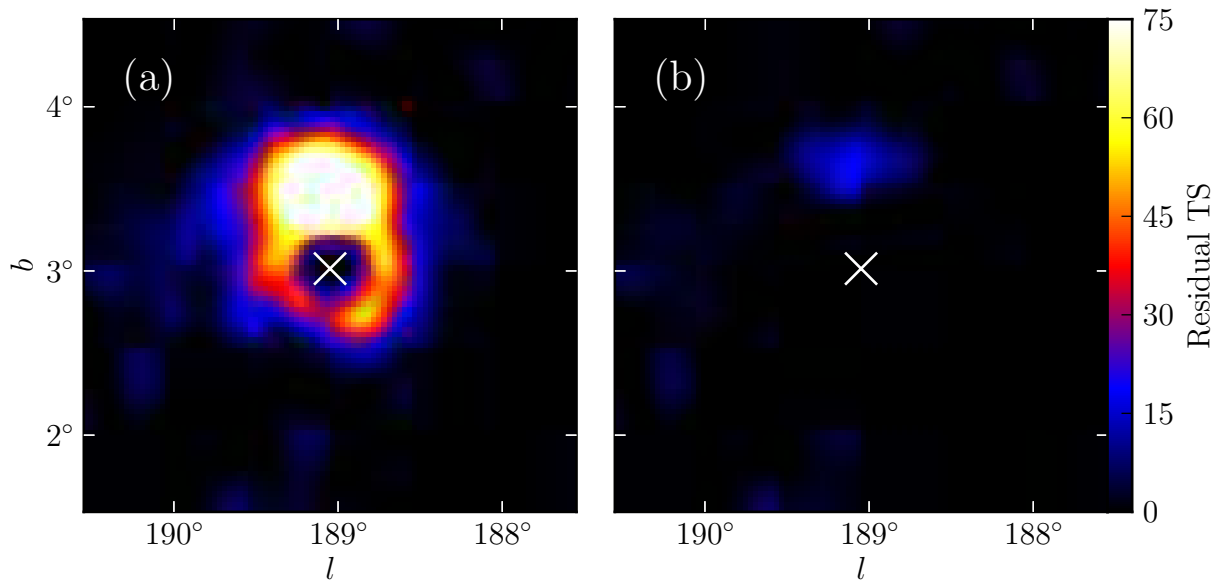


Fig. 14.— A TS map generated for the region around the SNR IC 443 using photons with energies between 1 GeV and 100 GeV. (a) TS map after subtracting IC 443 modeled as a point-like source. (b) same as (a), but IC 443 modeled as an extended source. The cross represents the best fit position of IC 443.

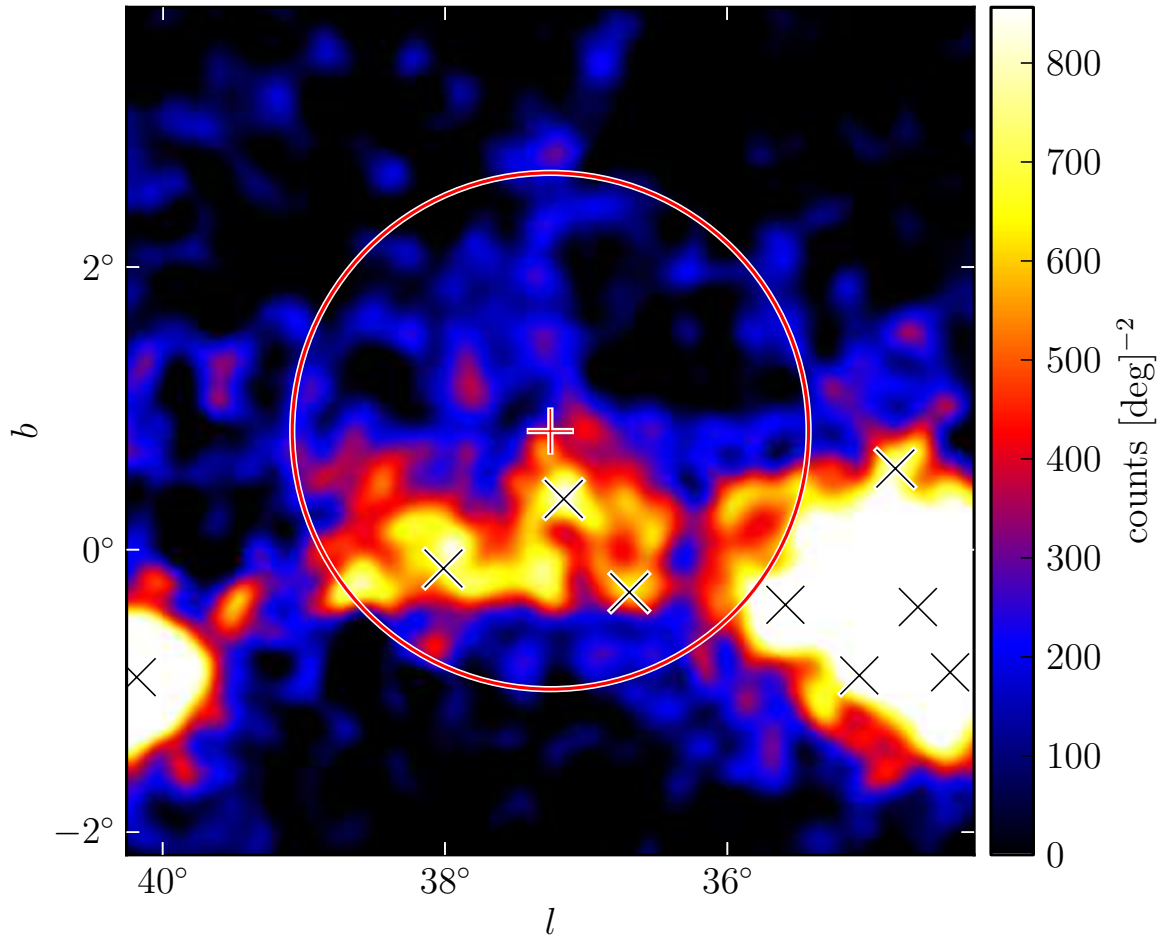


Fig. 15.— A diffuse-emission-subtracted 1 GeV to 100 GeV counts map of the region around 2FGL J1856.2+0450c smoothed by a  $0.1^\circ$  2D Gaussian kernel. The plus-shaped marker and circle (colored red in the online version) represent the center and size of the source fit with a radially-symmetric uniform disk spatial model. The black crosses represent the positions of other 2FGL sources. The extension is statistically significant, but the extension encompasses many 2FGL sources and the emission does not look to be uniform. Although the fit is statistically significant, it likely corresponds to residual features of inaccurately modeled diffuse emission picked up by the fit.



Table 4. Extension fit for the nine additional extended sources

Name	GLON (deg.)	GLAT (deg.)	$\sigma$ (deg.)	TS	TS <sub>ext</sub>	Pos Err (deg.)	Flux <sup>(a)</sup>	Index	Counterpart
E>1 GeV									
2FGL J0823.0–4246	260.32	–3.28	$0.37 \pm 0.03 \pm 0.02$	322.2	48.0	0.02	$8.4 \pm 0.6$	$2.21 \pm 0.09$	Puppis A
2FGL J1627.0–2425c	353.07	16.80	$0.42 \pm 0.05 \pm 0.16$	139.9	32.4	0.04	$6.3 \pm 0.6$	$2.50 \pm 0.14$	Ophiuchus
E>10 GeV									
2FGL J0851.7–4635	266.31	–1.43	$1.15 \pm 0.08 \pm 0.02$	116.6	86.8	0.07	$1.3 \pm 0.2$	$1.74 \pm 0.21$	Vela Jr.
2FGL J1615.0–5051	332.37	–0.13	$0.32 \pm 0.04 \pm 0.01$	50.4	16.7	0.04	$1.0 \pm 0.2$	$2.19 \pm 0.28$	HESS J1616–508
2FGL J1615.2–5138	331.66	–0.66	$0.42 \pm 0.04 \pm 0.02$	76.1	46.5	0.04	$1.1 \pm 0.2$	$1.79 \pm 0.26$	HESS J1614–518
2FGL J1632.4–4753c	336.52	0.12	$0.35 \pm 0.04 \pm 0.02$	64.4	26.9	0.04	$1.4 \pm 0.2$	$2.66 \pm 0.30$	HESS J1632–478
2FGL J1712.4–3941 <sup>(b)</sup>	347.26	–0.53	$0.56 \pm 0.04 \pm 0.02$	59.4	38.5	0.05	$1.2 \pm 0.2$	$1.87 \pm 0.22$	RX J1713.7–3946
2FGL J1837.3–0700c	25.08	0.13	$0.33 \pm 0.07 \pm 0.05$	47.0	18.5	0.07	$1.0 \pm 0.2$	$1.65 \pm 0.29$	HESS J1837–069
2FGL J2021.5+4026	78.24	2.20	$0.63 \pm 0.05 \pm 0.04$	237.2	128.9	0.05	$2.0 \pm 0.2$	$2.42 \pm 0.19$	$\gamma$ -Cygni

<sup>(a)</sup>Integral Flux in units of  $10^{-9}$  ph cm<sup>-2</sup> s<sup>-1</sup> and integrated in the fit energy range (either 1 GeV to 100 GeV or 10 GeV to 100 GeV).

<sup>(b)</sup>The discrepancy in the best fit spectra of 2FGL J1712.4–3941 compared to Abdo et al. (2011) is due to fitting over a different energy range.

Note. — The columns in this table have the same meaning as those in Table 3. RX J1713.7–3946 and Vela Jr. were previously studied in dedicated publications (Abdo et al. 2011; Tanaka et al. 2011).

Table 5. Dual localization, alternative PSF, and alternative approach to modeling the diffuse emission

Name	TS <sub>pointlike</sub>	TS <sub>gtlike</sub>	TS <sub>alt,diff</sub>	TS <sub>extpointlike</sub>	TS <sub>extgtlike</sub>	TS <sub>extalt,diff</sub>	$\sigma$ (deg.)	$\sigma_{alt,diff}$ (deg.)	$\sigma_{alt,psf}$ (deg.)	TS <sub>2pts</sub>
E>1 GeV										
2FGL J0823.0–4246	331.9	322.2	356.0	60.0	48.0	56.0	0.37	0.39	0.39	23.0
2FGL J1627.0–2425c	154.8	139.9	105.7	39.4	32.4	24.8	0.42	0.40	0.58	24.5
E>10 GeV										
2FGL J0851.7–4635	115.2	116.6	123.1	83.9	86.8	89.8	1.15	1.16	1.17	15.5
2FGL J1615.0–5051 <sup>(a)</sup>	48.2	50.4	56.6	15.2	16.7	17.8	0.32	0.33	0.32	13.1
2FGL J1615.2–5138	75.0	76.1	83.8	42.9	46.5	54.1	0.42	0.43	0.43	35.1
2FGL J1632.4–4753c	64.5	64.4	66.8	23.0	26.9	25.5	0.35	0.36	0.37	10.9
2FGL J1712.4–3941	59.8	59.4	39.9	38.4	38.5	30.7	0.56	0.55	0.53	2.7
2FGL J1837.3–0700c	44.5	47.0	39.2	17.6	18.5	16.1	0.33	0.32	0.38	10.8
2FGL J2021.5+4026	239.1	237.2	255.8	139.1	128.9	138.0	0.63	0.65	0.59	37.3

<sup>(a)</sup>Using `pointlike`, TS<sub>ext</sub> for 2FGL J1615.0–5051 was slightly below 16 when the source was fit in the 10 GeV to 100 GeV energy range. To confirm the extension measure, the extension was refit in `pointlike` using a slightly lower energy. In the 5.6 GeV to 100 GeV energy range, we obtained a consistent extension and TS<sub>ext</sub> = 28.0. In the rest of this paper, we quote the  $E > 10\text{GeV}$  results for consistency with the other sources.

Note. — TS<sub>pointlike</sub>, TS<sub>gtlike</sub>, and TS<sub>alt,diff</sub> are the test statistic values from `pointlike`, `gtlike`, and `gtlike` with the alternative approach to modeling the diffuse emission respectively. TS<sub>extpointlike</sub>, TS<sub>extgtlike</sub>, and TS<sub>extalt,diff</sub> are the TS values from `pointlike`,

`gtlike`, and `gtlike` with the alternative approach to modeling the diffuse emission respectively.  $\sigma$ ,  $\sigma_{\text{alt,diff}}$ , and  $\sigma_{\text{alt,psf}}$  are the fit sizes assuming a radially-symmetric uniform disk model with the standard analysis, the alternative approach to modeling the diffuse emission, and the alternative PSF respectively.

Table 6. Nearby Residual-induced Sources

Extended Source	Residual-induced Sources
2FGL J0823.0–4246	2FGL J0821.0–4254, 2FGL J0823.4–4305
2FGL J1627.0–2425c	...
2FGL J0851.7–4635	2FGL J0848.5–4535, 2FGL J0853.5–4711, 2FGL J0855.4–4625
2FGL J1615.0–5051	...
2FGL J1615.2–5138	2FGL J1614.9–5212
2FGL J1632.4–4753c	2FGL J1634.4–4743c
2FGL J1712.4–3941	...
2FGL J1837.3–0700c	2FGL J1835.5–0649
2FGL J2021.5+4026	2FGL J2019.1+4040

Note. — For each new extended source, we list nearby 2FGL sources that we have concluded here correspond to residuals induced by not modeling the extensions of nearby extended sources.

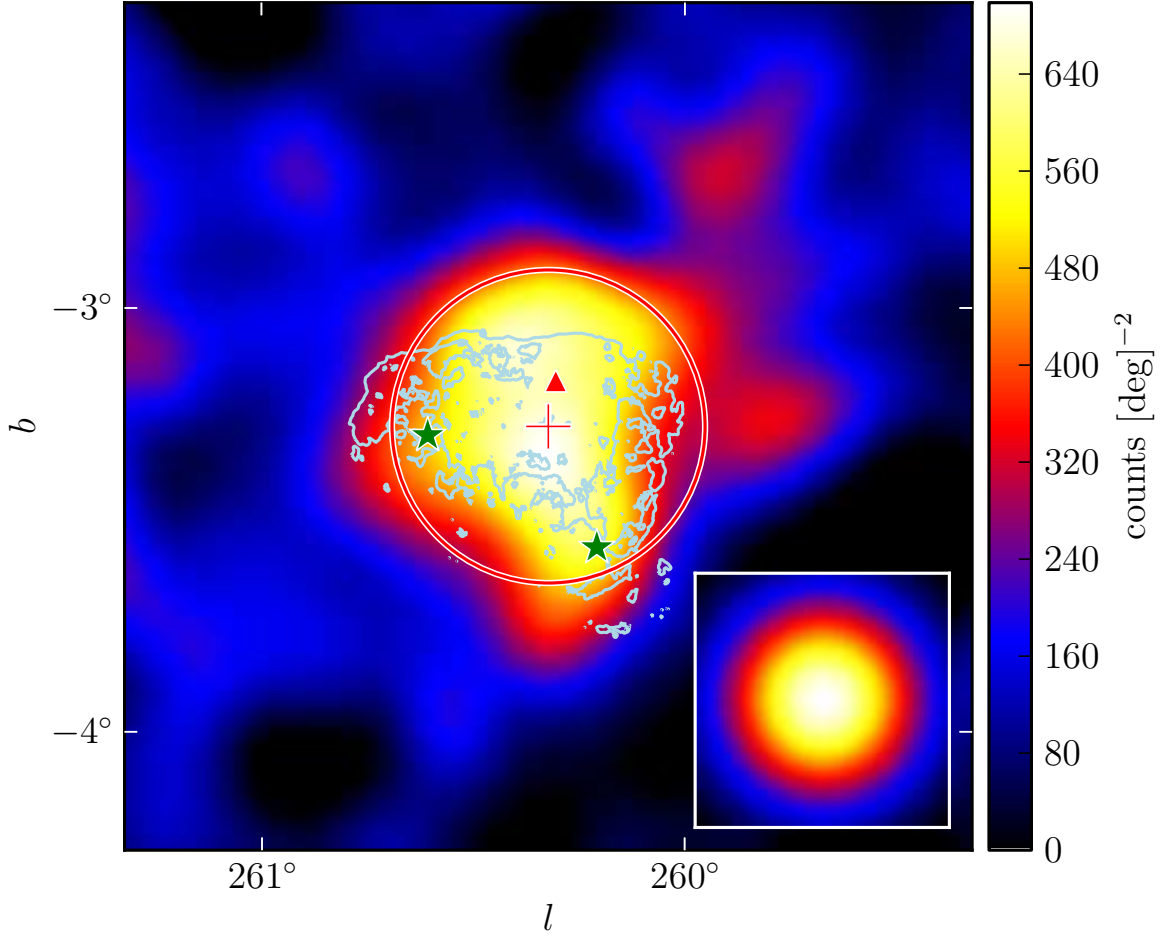


Fig. 16.— A diffuse-emission-subtracted 1 GeV to 100 GeV counts map of 2FGL J0823.0–4246 smoothed by a  $0\text{.}1$  2D Gaussian kernel. The triangular marker (colored red in the online version) represents the 2FGL position of this source. The plus-shaped marker and the circle (colored red) represent the best fit position and extension of this source assuming a radially-symmetric uniform disk model. The two star-shaped markers (colored green) represent 2FGL sources that were removed from the background model. From left to right, these sources are 2FGL J0823.4–4305 and 2FGL J0821.0–4254. The lower right inset is the model predicted emission from a point-like source with the same spectrum as 2FGL J0823.4–4305 smoothed by the same kernel. This source is spatially coincident with the Puppis A SNR. The light blue contours correspond to the X-ray image of Puppis A observed by *ROSAT* (Petre et al. 1996).

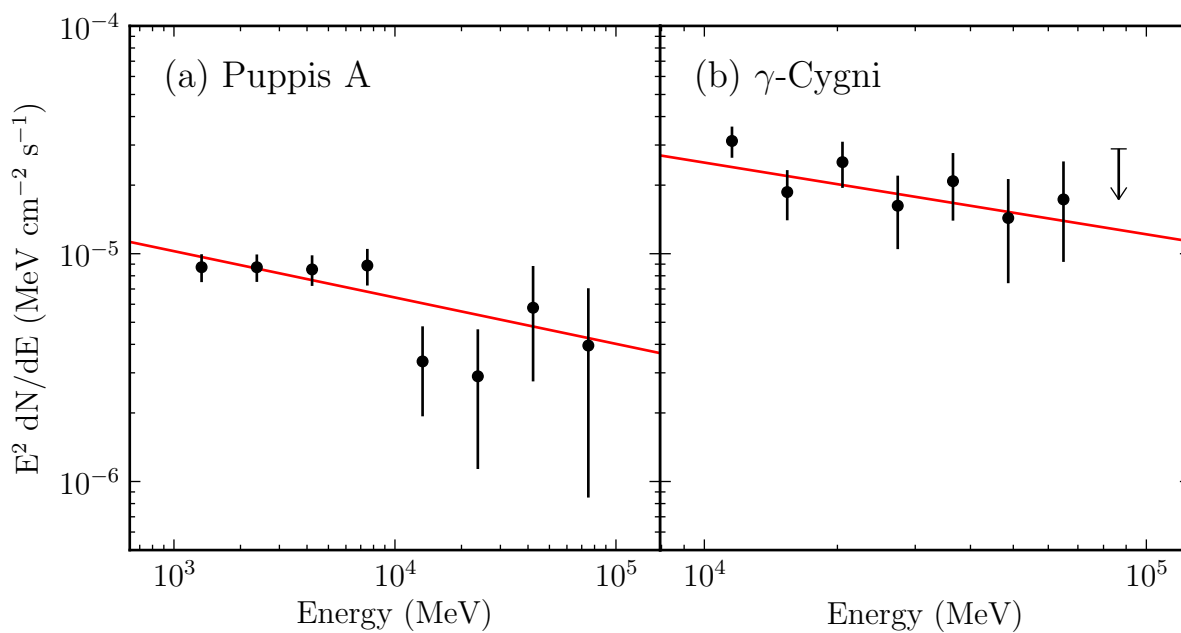


Fig. 17.— The spectral energy distribution of the extended sources Puppis A (2FGL J0823.0–4246) and  $\gamma$ -Cygni (2FGL J2021.5+4026). The lines (colored red in the online version) are the best fit power-law spectral models of these sources. Puppis A has a spectral index of  $2.21 \pm 0.09$  and  $\gamma$ -Cygni has an index of  $2.42 \pm 0.19$ . The spectral errors are statistical only. The upper limit is at the 95% confidence level.

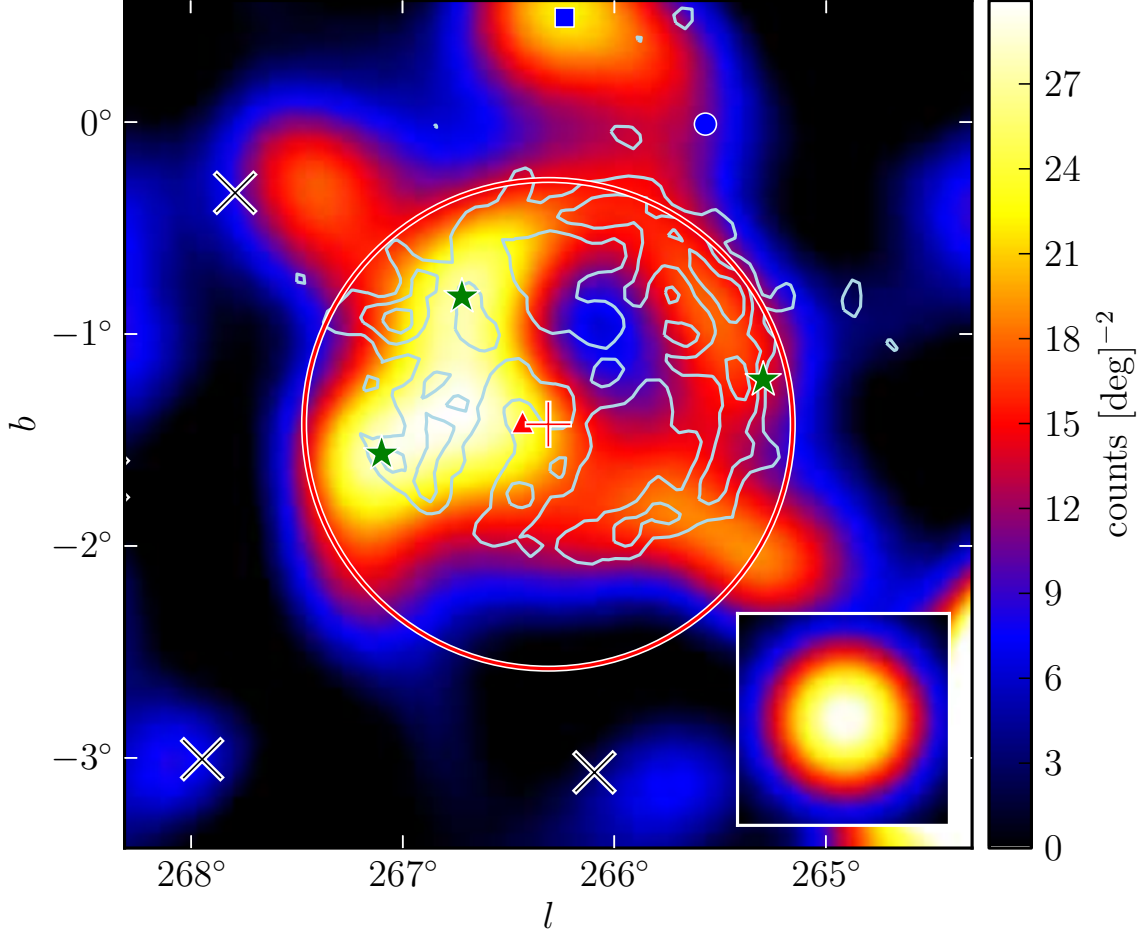


Fig. 18.— A diffuse-emission-subtracted 10 GeV to 100 GeV counts map of 2FGL J0851.7–4635 smoothed by a  $0.25^\circ$  2D Gaussian kernel. The triangular marker (colored red in the electronic version) represents the 2FGL position of this source. The plus-shaped marker and the circle (colored red) are the best fit position and extension of this source assuming a radially-symmetric uniform disk model. The three black crosses represent background 2FGL sources. The three star-shaped markers (colored green) represent other 2FGL sources that were removed from the background model. They are (from left to right) 2FGL J0853.5–4711, 2FGL J0855.4–4625, and 2FGL J0848.5–4535. The circular and square-shaped marker (colored blue) represents the 2FGL and relocalized position of another 2FGL source. This extended source is spatially coincident with the Vela Jr. SNR. The contours (colored light blue) correspond to the TeV image of Vela Jr. (Aharonian et al. 2007a).

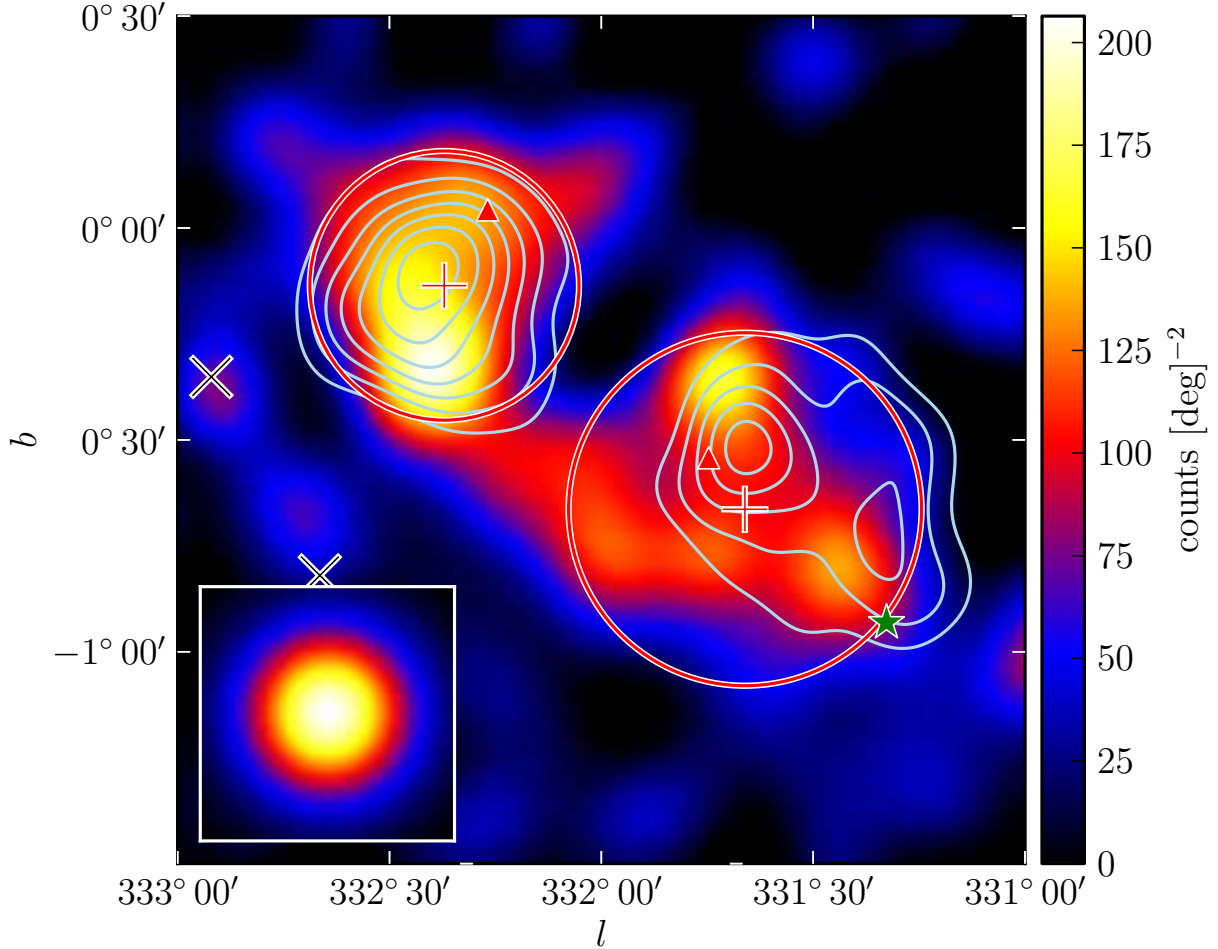


Fig. 19.— A diffuse-emission-subtracted 10 GeV to 100 GeV counts map of 2FGL J1615.0–5051 (upper left) and 2FGL J1615.2–5138 (lower right) smoothed by a  $0^\circ:1$  2D Gaussian kernel. The triangular markers (colored red in the electronic version) represent the 2FGL positions of these sources. The cross-shaped markers and the circles (colored red) represent the best fit positions and extensions of these sources assuming a radially symmetric uniform disk model. The two black crosses represent background 2FGL sources and the star-shaped marker (colored green) represents 2FGL J1614.9-5212, another 2FGL source that was removed from the background model. The contours (colored light blue) correspond to the TeV image of HESS J1616–508 (left) and HESS J1614–518 (right) (Aharonian et al. 2006).



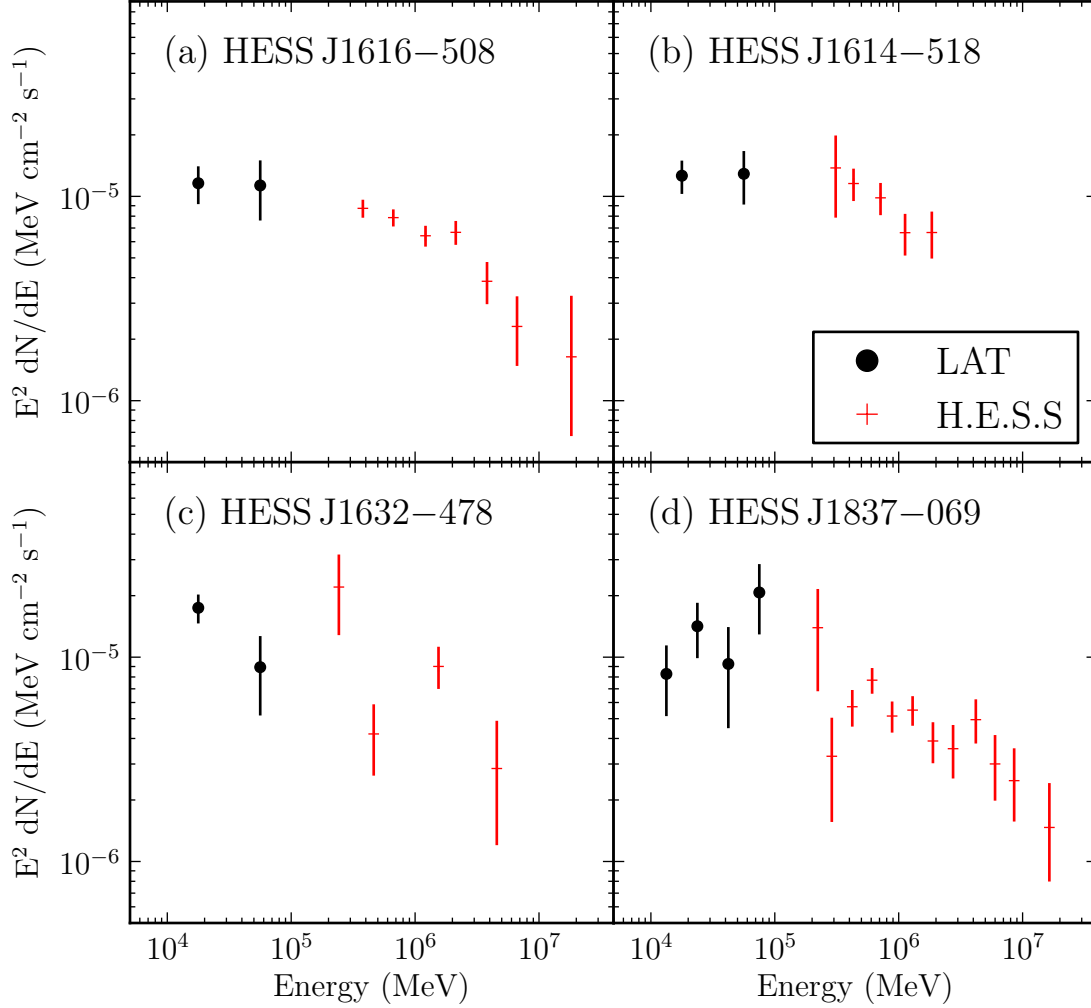


Fig. 20.— The spectral energy distribution of four extended sources associated with unidentified extended TeV sources. The black points with circular markers are obtained by the LAT. The points with plus-shaped markers (colored red in the electronic version) are for the associated H.E.S.S. sources. (a) the LAT SED of 2FGL J1615.0–5051 together with the H.E.S.S. SED of HESS J1616–508. (b) 2FGL J1615.2–5138 and HESS J1614–518. (c) 2FGL J1632.4–4753c and HESS J1632–478. (d) 2FGL J1837.3–0700c and HESS J1837–069. The H.E.S.S. data points are from (Aharonian et al. 2006). Both LAT and H.E.S.S. spectral errors are statistical only.

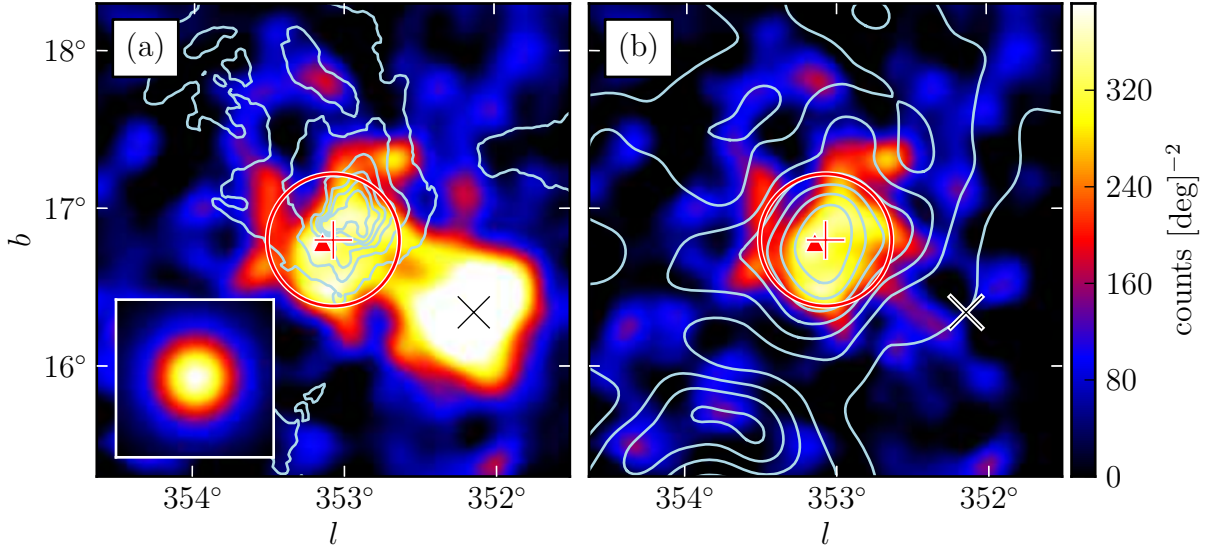


Fig. 21.— A diffuse-emission-subtracted 1 GeV to 100 GeV counts map of (a) the region around 2FGL J1627.0–2425 smoothed by a  $0.1$  2D Gaussian kernel and (b) with the emission from 2FGL J1625.7–2526 subtracted. The triangular marker (colored red in the online version) represents the 2FGL position of this source. The plus-shaped marker and the circle (colored red) represent the best fit position and extension of this source assuming a radially-symmetric uniform disk model and the black cross represents a background 2FGL source. The contours in (a) correspond to the  $100 \mu\text{m}$  image observed by IRAS (Young et al. 1986). The contours in (b) correspond to CO ( $J = 1 \rightarrow 0$ ) emission integrated from  $-8 \text{ km s}^{-1}$  to  $20 \text{ km s}^{-1}$ . They are from de Geus et al. (1990), were cleaned using the moment-masking technique (Dame 2011), and have been smoothed by a  $0.25$  2D Gaussian kernel.

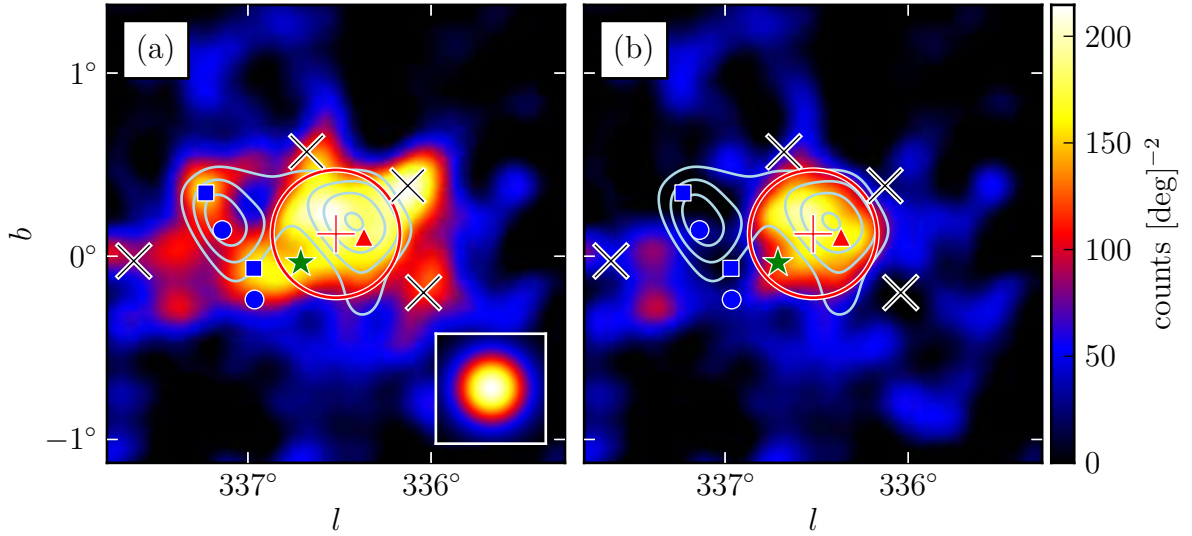


Fig. 22.— A diffuse-emission-subtracted 10 GeV to 100 GeV counts map of 2FGL J1632.4–4753c (a) smoothed by a  $0.1$  2D Gaussian kernel and (b) with the emission from the background sources subtracted. The triangular marker (colored red in the electronic version) represents the 2FGL position of this source. The plus-shaped marker and the circle (colored red) are the best fit position and extension of 2FGL J1632.4–4753c assuming a radially-symmetric uniform disk model. The four black crosses represent background 2FGL sources subtracted in (b). The circular and square-shaped markers (colored blue) represent the 2FGL and relocalized positions respectively of two additional background 2FGL sources subtracted in (b). The star-shaped marker (colored green) represents 2FGL J1634.4–4743c, another 2FGL source that was removed from the background model. The contours (colored light blue) correspond to the TeV image of HESS J1632–478 (Aharonian et al. 2006).

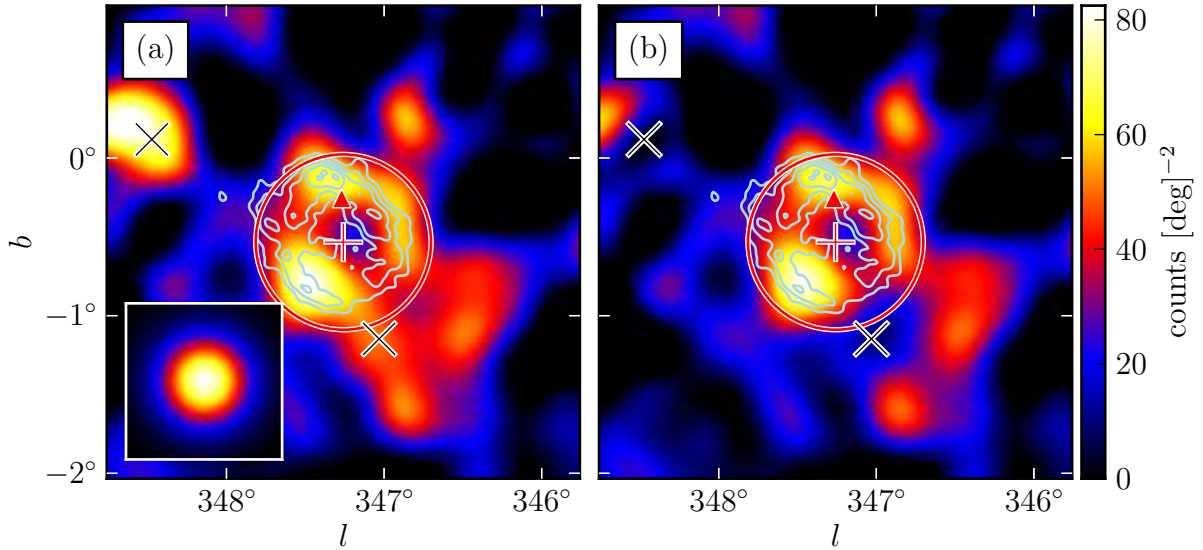


Fig. 23.— A diffuse-emission-subtracted 10 GeV to 100 GeV counts map of 2FGL J1712.4–3941 (a) smoothed by a  $0.15^\circ$  2D Gaussian kernel and (b) with the emission from the background sources subtracted. This source is spatially coincident with RX J1713.7–3946 and was recently studied in Abdo et al. (2011). The triangular marker (colored red in the online version) represents the 2FGL position of this source. The plus-shaped marker and the circle (colored red) are the best fit position and extension of this source assuming a radially symmetric uniform disk model. The two black crosses represent background 2FGL sources subtracted in (b). The contours (colored light blue) correspond to the TeV image (Aharonian et al. 2007b).

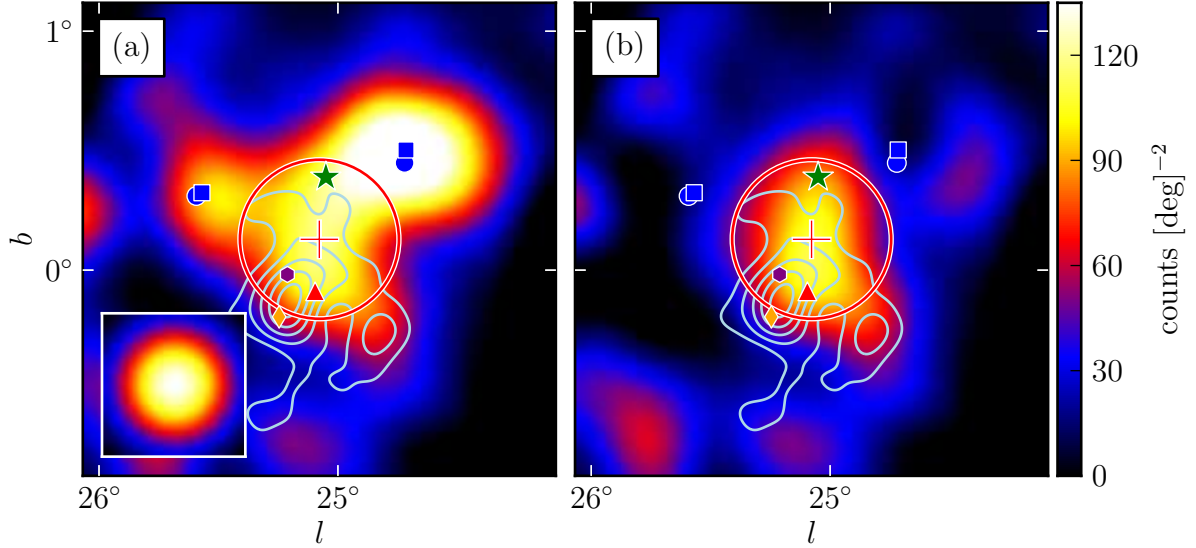


Fig. 24.— A diffuse-emission-subtracted 10 GeV to 100 GeV counts map of the region around 2FGL J1837.3–0700c (a) smoothed by a  $0.15^\circ$  2D Gaussian kernel and (b) with the emission from the background sources subtracted. The triangular marker (colored red in the online version) represents the 2FGL position of this source. The plus-shaped marker and the circle (colored red) represent the best fit position and extension of 2FGL J1837.3–0700c assuming a radially-symmetric uniform disk model. The circular and square-shaped markers (colored blue) represent the 2FGL and the relocalized positions respectively of two background 2FGL sources subtracted in (b). The star-shaped marker (colored green) represents 2FGL J1835.5–0649, another 2FGL source that was removed from the background model. The contours (colored light blue) correspond to the TeV image of HESS J1837–069 (Aharonian et al. 2006). The diamond-shaped marker (colored orange) represents the position of PSR J1838–0655 and the hexagonal-shaped marker (colored purple) represents the position AX J1837.3–0652 (Gotthelf & Halpern 2008).

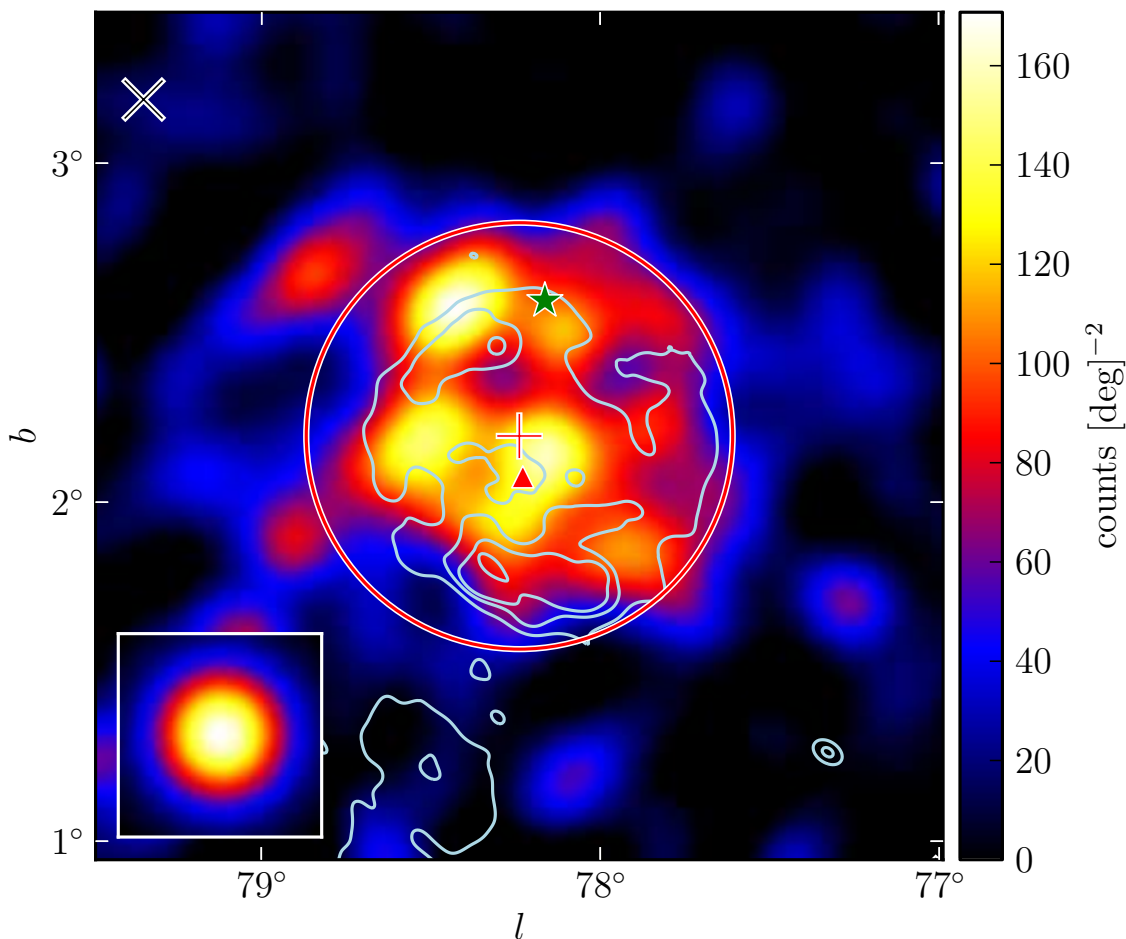


Fig. 25.— A diffuse-emission-subtracted 10 GeV to 100 GeV counts map of the region around 2FGL J2021.5+4026 smoothed by a  $0.1^\circ$  2D Gaussian kernel. The triangular marker (colored red in the online version) represents the 2FGL position of this source. The plus-shaped marker and the circle (colored red) represent the best fit position and extension of 2FGL J2021.5+4026 assuming a radially-symmetric uniform disk model. The star-shaped marker (colored green) represents 2FGL J2019.1+4040, a 2FGL source that was removed from the background model. 2FGL J2021.5+4026 is spatially coincident with the  $\gamma$ -Cygni SNR. The contours (colored light blue) correspond to the 408MHz image of  $\gamma$ -Cygni observed by the Canadian Galactic Plane Survey (Taylor et al. 2003).

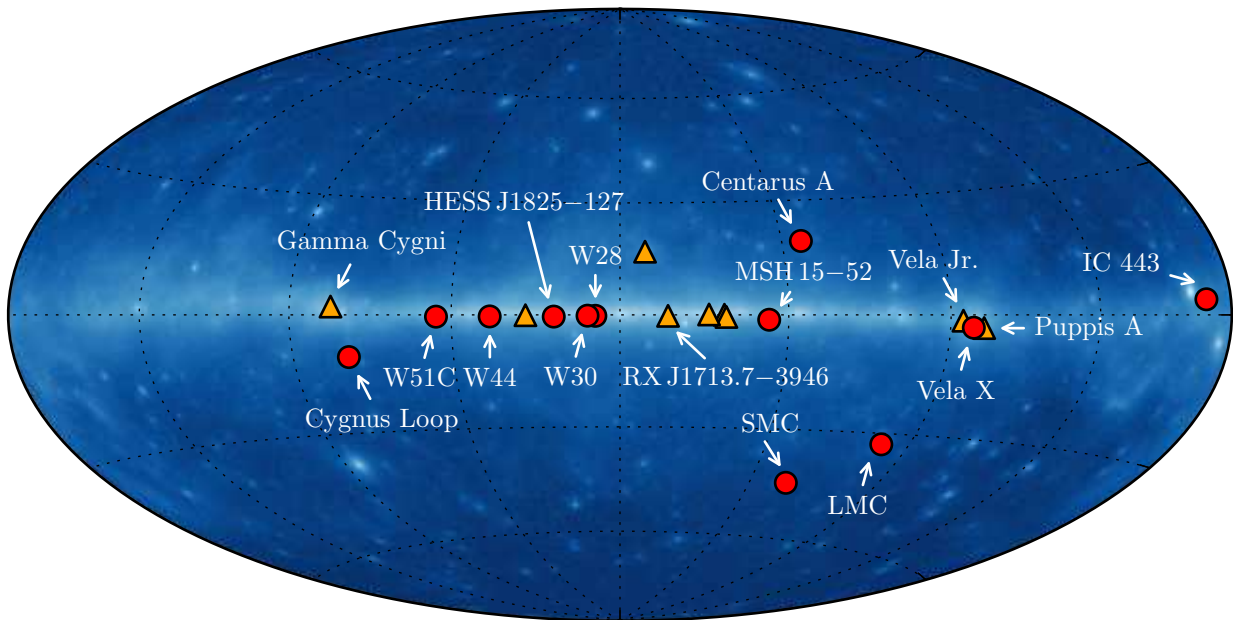


Fig. 26.— The 21 spatially extended sources detected by the LAT at GeV energies with 2 years of data. The twelve extended sources included in 2FGL are represented by the circular markers (colored red in the online version). The nine new extended sources are represented by the triangular markers (colored orange). The source positions are overlaid on a 100 MeV to 100 GeV Aitoff projection sky map of the LAT data in Galactic coordinates.

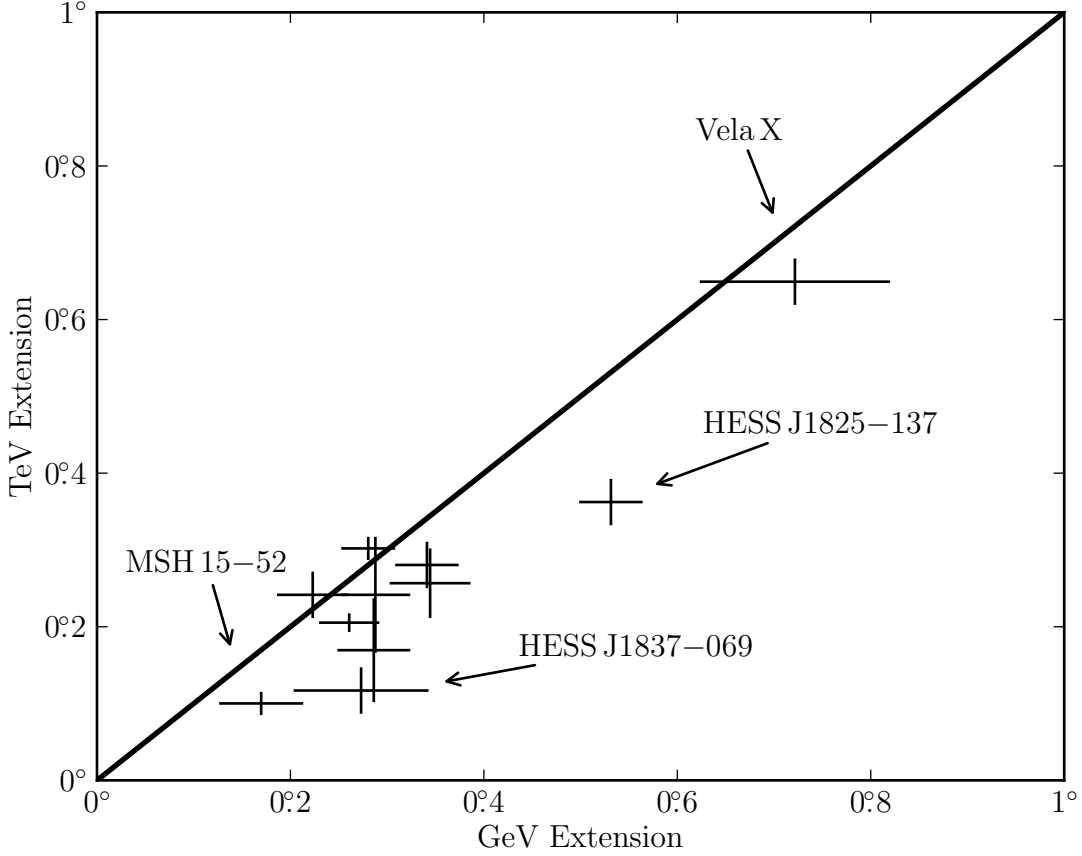


Fig. 27.— A comparison of the sizes of extended sources detected at both GeV and TeV energies. The TeV sizes of W30, 2FGL J1837.3–0700c, 2FGL J1632.4–4753c, 2FGL J1615.0–5051, and 2FGL J1615.2–5138 are from Aharonian et al. (2006). The TeV sizes of MSH 15–52, HESS J1825–137, Vela X, Vela Jr., RX J1713.7–3946 and W28 are from Aharonian et al. (2005, 2006b,c, 2007a,b, 2008). The TeV size of IC 443 is from Acciari et al. (2009) and W51C is from Krause et al. (2011). The TeV sizes of MSH 15–52, HESS J1614–518, HESS J1632–478, and HESS J1837–069 have only been reported with an elliptical 2D Gaussian fit and so the plotted sizes are the geometric mean of the semi-major and semi-minor axis. The LAT extension of Vela X is from Abdo et al. (2010f). The TeV sources were fit assuming a 2D Gaussian surface brightness profile so the plotted GeV and TeV extensions were first converted to  $r_{68}$  (see Section 2.4). Because of their large sizes, the shape of RX J1713.7–3946 and Vela Jr. were not directly fit at TeV energies and so are not included in this comparison. On the other hand, dedicated publications by the LAT collaboration on these sources showed that their morphologies are consistent (Abdo et al. 2011; Tanaka et al. 2011). The LAT extension errors are the statistical and systematic errors added in quadrature.



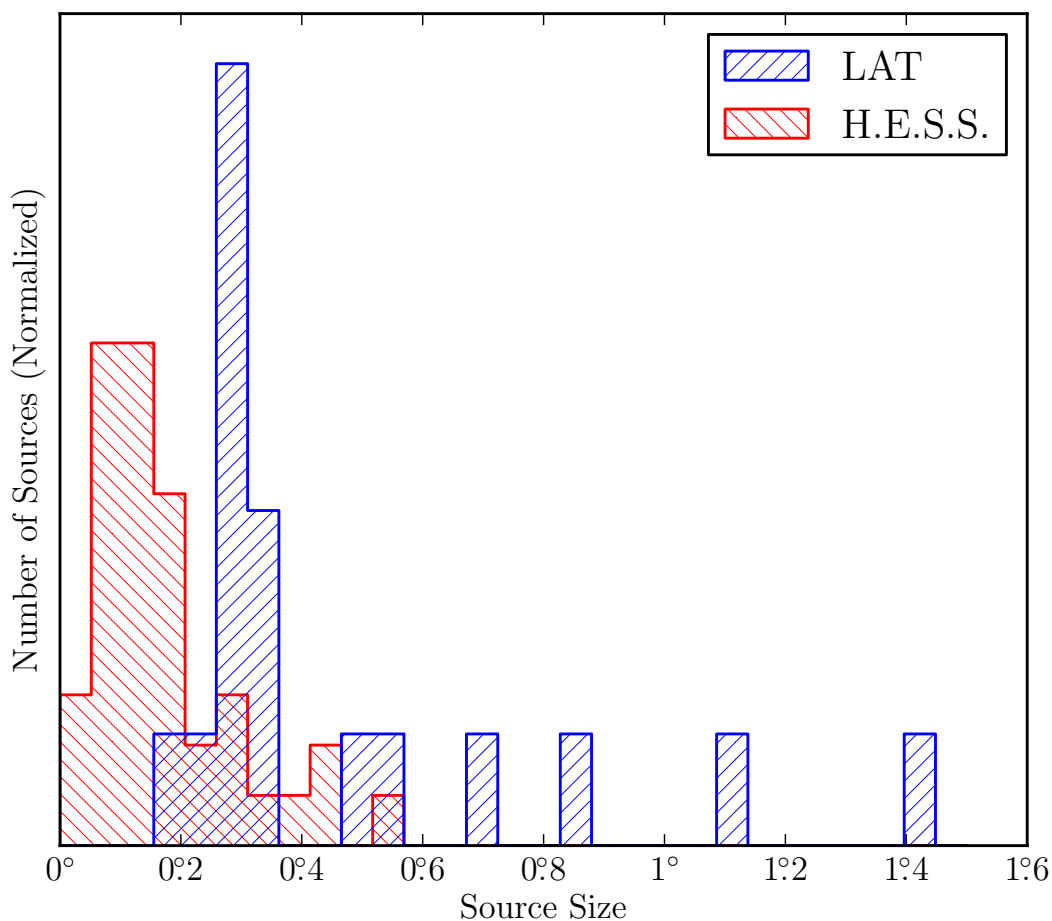


Fig. 28.— The distributions of the sizes of 18 extended LAT sources at GeV energies (colored blue in the electronic version) and the sizes of the 40 extended H.E.S.S. sources at TeV energies (colored red). The H.E.S.S. sources were fit with a 2D Gaussian surface brightness profile so the LAT and H.E.S.S. sizes were first converted to  $r_{68}$ . The GeV size of Vela X is taken from Abdo et al. (2010f). Because of their large sizes, the shape of RX J1713.7–3946 and Vela Jr. were not directly fit at TeV energies and are not included in this comparison. Centaurus A is not included because of its large size.

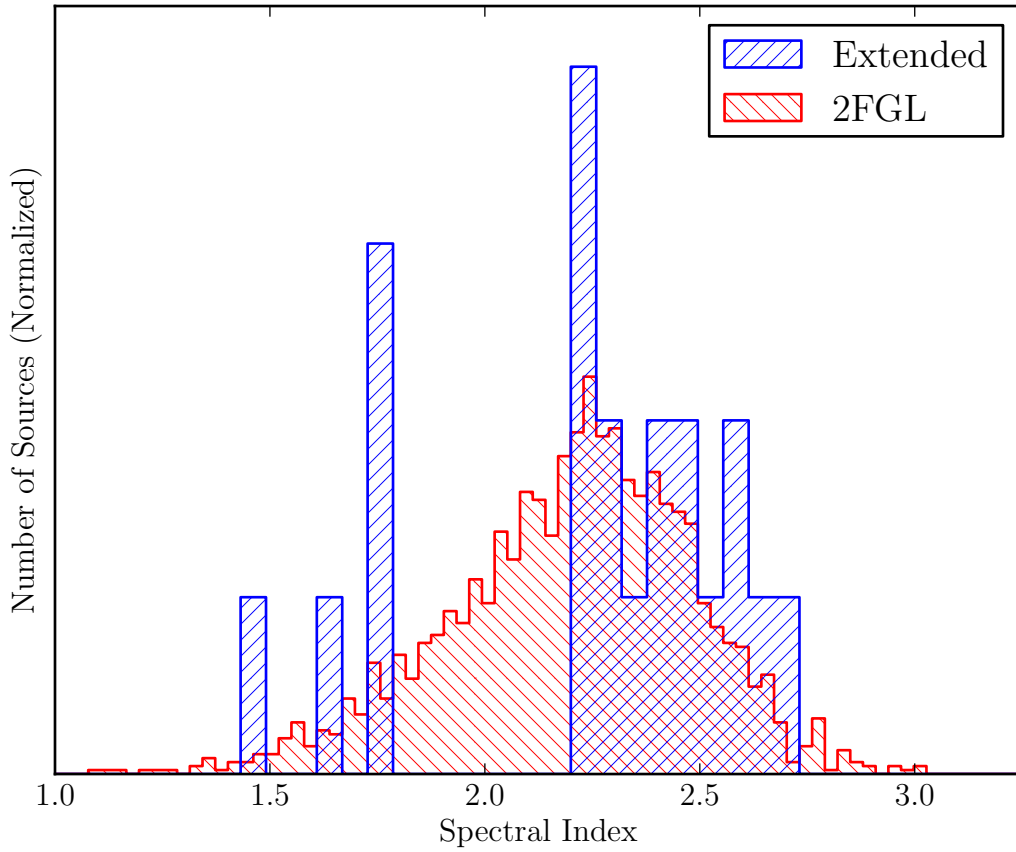


Fig. 29.— The distribution of spectral indices of the 1873 2FGL sources (colored red in the electronic version) and the 21 spatially extended sources (colored blue). The index of Centaurus A is taken from Nolan et al. (2012) and the index of Vela X is taken from Abdo et al. (2010f).